Full Title: Extended hopanoid lipids promote bacterial motility, surface attachment, and root nodule development in the *Bradyrhizobium diazoefficiens-Aeschynomene afraspera* symbiosis

Short Title: Extended hopanoids promote efficient *Bradyrhizobium-Aeschynomene* symbiosis

Belin, B.J.,[1] Tookmanian, E.T.,[1] de Anda, J.,[3] Wong, G. C. L.,[3] Newman, D.K.[1,2]

[1]Division of Biology & Bioengineering, [2]Division of Geological & Planetary Sciences, California Institute of Technology, Pasadena, CA.

[3]Department of Bioengineering, Department of Chemistry and Biochemistry, and California NanoSystems Institute, University of California Los Angeles, Los Angeles, CA 90095-1600, USA University of California Los Angeles, Los Angeles, CA.

Abstract

Hopanoids are steroid-like bacterial lipids that enhance membrane rigidity and promote bacterial growth under diverse stresses. Roughly 10% of bacteria contain genes involved in hopanoid biosynthesis, and these genes are particularly conserved in plant-associated organisms. We previously found that the extended class of hopanoids (C_{35}) in the nitrogen-fixing soil bacterium *Bradyrhizobium diazoefficiens* promotes its root nodule symbiosis with the tropical legume *Aeschynomene afraspera*. By quantitatively modeling root nodule development, we identify independent roles for hopanoids in the initiation of root nodule formation and in determining the rate of root nodule maturation. *In vitro* studies demonstrate that extended hopanoids support *B. diazoefficiens* motility and surface attachment, which may correlate with stable root colonization *in planta*. Confocal microscopy of maturing root nodules reveals that root nodules infected with extended hopanoid-deficient *B. diazoefficiens* contain unusually low densities of bacterial symbionts, indicating that extended hopanoids are necessary for persistent, high levels of host infection. This work identifies extended hopanoids as regulators of the efficiency of *Bradyrhizobia* nitrogen-fixing symbioses, agriculturally and economically significant associations with growing importance in a changing climate.

Introduction

Hopanoids are steroid-like lipids synthesized by metabolically and environmentally diverse bacteria. Studies in multiple organisms have shown that hopanoids support bacterial survival in response to stress, including growth under conditions of high osmolarity, low pH, elevated temperatures, detergents, and antibiotics (reviewed in ref. [1]). It is thought that hopanoids primarily promote survival by rigidifying and decreasing the permeability of membranes,[2],[3] providing a better barrier against external insults. Hopanoids may also directly regulate proteins, chemical signals, and other lipids in the membrane (as do eukaryotic sterols[4]), but such interactions are yet to be characterized.

Hopanoids consist of a 30-carbon pentacyclic core, generated by the squalene-hopene cyclase (*shc*) family of enzymes,[5],[6] that can be modified to generate a medley of distinct molecules. The most common hopanoid modifications are methylation by the enzyme HpnP[7] and addition of a ribose-derived side chain by the enzyme HpnH (Fig. 1a)[8]. Downstream enzymes can further diversify side chains

40 added by HpnH,[9] and the resulting molecules are known collectively as the C_{35} or extended hopanoids.
41 Common extended hopanoid side chains include aminotriol-, polyol-, and adenosyl- moieties, although
42 organism-specific side chains have also been observed. For example, the *Bradyrhizobiaceae* family of
43 soil bacteria encode an extended hopanoid with a lipid A side chain, known as HoLA[10–12]. It is an open
44 question whether HoLA and other specific extended hopanoids perform non-overlapping functions in
45 cells, although evidence that methylated and extended hopanoids affect membrane biophysics and stress
46 tolerance to differing degrees supports this notion (reviewed in ref. [1]).

47 In the environment, hopanoid biosynthesis genes are enriched in plant-associated
48 metagenomes,[13] and they are highly conserved in the plant growth-promoting *Bacilli*, *Nostoc* and
49 *Anabaena* symbionts of various green plants, and *Frankia* and *Bradyrhizobia* nitrogen-fixing symbionts of
50 legumes[14],[15]. We previously found that hopanoids are required for optimal symbiosis of two strains of
51 *Bradyrhizobia*, the photosynthetic *Bradyrhizobium* BTAi1 and the model *Bradyrhizobium diazoefficiens*,
52 with members of the *Aeschynomene* genus of tropical legumes[10,11]. The symbiotic properties of *B.*
53 *diazoefficiens* are of particular agricultural and economic significance because it natively forms symbioses
54 with soybean crops[16]. In a *B. diazoefficiens-Aeschynomene afraspera* symbiosis model, we found that
55 the bacterial extended hopanoids specifically are required for optimal rates of *in planta* nitrogen
56 fixation[11].

57 Numerous processes in bacteria and plant hosts determine the rate of nitrogen fixation in legume-
58 rhizobia symbioses. The most basic requirement is the inherent capacity of bacteria to perform the
59 nitrogen fixation reaction, which demands a high uptake of various trace metals, rapid consumption of
60 protons and ATP, and the absence of freely-diffusing oxygen. In *Frankia* legume symbionts, it has been
61 suggested that hopanoids help to maintain a low-oxygen environment by limiting oxygen diffusion across
62 membranes[17–19], although comparative measurements of free oxygen in wild type and hopanoid-
63 deficient strains have not been performed.

64 Another determinant of root nodule nitrogen fixation levels is the efficiency of root nodule
65 development, beginning with rhizobial colonization of the plant root surface. In *Aeschynomene* hosts root
66 colonization occurs on plant root “cracks”, breaks in the outer epidermal layers formed naturally by lateral
67 root emergence[20]. *B. diazoefficiens* possesses two systems that guide motility towards these cracks, a

68 constitutive subpolar flagellum and inducible lateral flagella[21], which appear to fill complementary roles.
69 The subpolar flagellum primarily drives chemotaxis in open aquatic environments, whereas the lateral
70 flagella promote motility on surfaces or in viscous fluids[22]; presumably these activities correspond to
71 persistent, long-range movement towards hosts and clearing obstacles on the soil and root surface,
72 respectively[23,24]. In *A. afraspera,* root surface colonization also requires bacterial Nod factors,
73 immunosuppressant molecules that activate pro-symbiotic signaling[25].
74 After stable colonies are established at root cracks, rhizobial infections progress to the root
75 interior. The cytological details of this process have been characterized for *A. afraspera* only in
76 association with the *Bradyrhizobium* strain ORS285,[25] and in this context, rhizobia can be observed
77 invading roots via thread-like patterns in the intercellular spaces of the inner epidermal and cortical cell
78 layers. At the cortex, several host cells become intracellularly infected with bacteria. These infected cells
79 appear to internalize the bacteria through narrow membrane invaginations, each enclosing multiple
80 bacterial cells, that pinch off to form intracellular infection pockets[25]. In a few infected cells, these
81 infection pockets presumably break down into symbiosomes, an organelle-like structure consisting of
82 intracellular bacteria (now called “bacteroids”) surrounded by a plant membrane, which is the basic
83 nitrogen-fixing unit and defining feature of the root nodule.
84 Two developmental programs follow symbiosome formation in *A. afraspera*. In the first, infected
85 host cells enter a proliferative state[25], forming the nodule primordium, and grow to form a large,
86 spherical mass of infected cells known as the central infection zone. As the infection zone develops it is
87 enveloped by epidermal tissue, and eventually, a vasculature system. This pathway for infection zone
88 formations is unusual among legumes. More commonly, the nodule primordium arises from a meristem
89 that is regulated independently and spatially separated from the bacterial invasion site; paradoxically,
90 bacterial internalization in meristem-dependent nodules often inhibits, rather than stimulates, further host
91 proliferation[26]. Another notable feature of *A. afraspera* is that two or more discrete infection zones may
92 develop in the same nodule, resulting in a multi-lobed morphology. Each infection zone is thought to arise
93 from a single infected cell, as co-inoculation of *A. afraspera* with a mixture of GFP- and mCherry-
94 expressing *Bradyrhizobia* strains generally results in infection zones expressing only one
95 fluorophore[25,27].

96 The second program initiated by symbiosome formation is the establishment of major genetic and
97 chemical changes for bacteroids, including a sharp reduction in pH[28] and free oxygen levels[29] in the
98 surrounding environment, high levels of bacteroid genome duplication, suppression of non-symbiotic
99 genes, extreme changes in bacterial morphology, and a loss of bacteroid viability. These genetic changes
100 are directed largely by antimicrobial NCR (nodule cysteine-rich) peptides produced by legume hosts
101 (reviewed in [30]). Mutant rhizobia with higher susceptibility to the NCR peptides *in vitro* tend to be
102 ineffective symbionts that trigger plant defense reactions or early senescence of root nodules, a process
103 in which the central nodule tissue is degraded and recycled by the host[31].
104 In this study, we sought to better understand how the extended hopanoids of *B. diazoefficiens*
105 support nitrogen fixation in the *A. afraspera* root nodule symbiosis. We found that the lower nitrogen
106 fixation of extended hopanoid mutants can be explained by a reduction in root nodule size and rhizobial
107 occupancy, indicating that the underlying defect is primarily developmental rather than relating to per-
108 bacteroid nitrogen fixation productivity. By novel application of a quantitative framework for modeling plant
109 tissue growth using single-nodule tracking, we find that extended hopanoids support root nodule
110 development through two independent pathways: by promoting bacterial motility towards and attachment
111 to root surfaces and by maintaining normal host and symbiosome proliferation rates in the infection zone.
112 In addition, our results reveal the dynamics of nodulation in *A. afraspera*, demonstrating that for these
113 plants nodulation occurs in bursts separated by fixed intervals that do not depend on net fixed nitrogen
114 production across the root. We further suggest that nodule growth rates are key determinants of an *A.*
115 *afraspera* nodule's nitrogen fixation output at maturity, in which growth rates may be "tuned" to stimulate
116 proliferation in nodules with more effective symbionts.
117
118 **Results**
119
120 *Loss of extended hopanoids results in reduced nodule size*
121 Previously, we observed a symbiotic defect for a mutant lacking extended hopanoids (Δ*hpnH*) in
122 the *B. diazoefficiens-Aeschynomene afraspera* symbiosis model[11]. To verify and better understand this
123 defect, we inoculated *A. afraspera* plants with Δ*hpnH,* Δ*hpnP* (lacking 2-Me hopanoids), or wild-type *B.*

124 *diazoefficiens*. At 24 days post-inoculation (dpi), plants inoculated with Δ*hpnH* were shorter than wild
125 type-inoculated plants, although both strains produced equivalent numbers of nodules (Fig. 1b). Δ*hpnH*-
126 inoculated plants also exhibited a roughly 50% decrease in the rate of reduction of acetylene gas (a proxy
127 for nitrogen fixation) compared to wild type-inoculated plants at this time point (Fig. 1c). In contrast, the
128 Δ*hpnP* mutant was similar to wild type (Fig. 1b-c). These results are consistent with our previous
129 findings[11].

130 We initially hypothesized that the Δ*hpnH* defect in nitrogen fixation *in planta* occurs because of
131 poor survival of the Δ*hpnH* mutant in hosts, given that *in vitro* the Δ*hpnH* strain is more susceptible to
132 conditions mimicking the nodule environment (*e.g.* low pH, low oxygen, high osmolarity, and NCR
133 peptides)[11]. To assess Δ*hpnH* viability within *A. afraspera* nodules, we performed morphological
134 analyses of nodule semi-thin sections using confocal fluorescent microscopy. Hand-sectioned nodule
135 slices (of roughly 200-500 μm thickness) were stained with a bacterial live:dead kit, consisting of the
136 SYTO9 DNA dye, which is cell-permeable and labels all cells, and propidium iodide (PI), a dye that
137 uniquely labels cells with compromised membranes, which are generally non-viable. Contrary to our
138 expectations, we did not observe an increase in PI staining in nodules containing Δ*hpnH* (Fig. 1d; Fig.
139 S1,S2). Signatures of plant defense reactions, which previously were associated with Δ*hpnH*[11], were
140 also rare, occurring prominently in only ~1.5% (1/67) of nodules (Fig. S2).

141 The most apparent difference in the morphology of Δ*hpnH* nodules compared to wild type was
142 the presence of relatively small nodules (Fig. S1,S2). To determine whether lower nodule size could
143 explain reduced nitrogen fixation in Δ*hpnH*-inoculated plants, we repeated acetylene reduction assays for
144 wild-type- and Δ*hpnH*-inoculated plants, harvested their nodules, and calculated the total nodule dry
145 mass for each plant at 24 dpi. We found a decrease in the nodule dry mass per plant for Δ*hpnH*-
146 inoculated plants that is commensurate with the decrease in acetylene reduction rates (Fig. 1e). After
147 normalization by nodule dry mass, no significant difference could be observed in acetylene reduction
148 between the wild-type- and Δ*hpnH*-inoculated plants (Fig. 1e). This suggests the *in planta* nitrogen
149 fixation defect of Δ*hpnH* at 24 dpi can be explained by smaller average nodule sizes. It also rules out the
150 possibility that nitrogenase functions ineffectively in the absence of extended hopanoids due to

151 inactivation by oxygen, as has been suggested in *Frankia*[17–19], as the per-mg nitrogen fixation rates
152 are unaffected in Δ*hpnH*.
153
154 *Δ*hpnH *nodules are more variable in size than wild-type nodules*
155 Curious about the origin of the smaller Δ*hpnH* nodule sizes, we devised three *a priori* hypotheses
156 for how small nodules could arise: first, that Δ*hpnH* nodule growth is terminated prematurely; second, that
157 Δ*hpnH* nodules grow at a slower rate; and third, that the initiation of Δ*hpnH* nodules is delayed. Of these
158 scenarios, the first possibility is unique in that Δ*hpnH* nodules would be *necessarily* smaller than wild
159 type; in other words, Δ*hpnH* nodules could not "catch up" to wild type given additional time. To test this
160 possibility, we measured acetylene reduction per plant across an extended 40 dpi period, and we
161 observed that the differences in both acetylene reduction rates and nodule dry masses between wild type
162 and Δ*hpnH* steadily decreased with time (Fig. 2a-b). By 40 dpi the overall symbiotic efficiencies of wild
163 type and Δ*hpnH* per plant were indistinguishable, in terms of the plants' qualitative appearance (Fig. 2c,d)
164 as well as their average shoot heights and acetylene reduction rates (Fig. S3). Total nodule counts per
165 plant also did not differ between wild type and Δ*hpnH* at 40 dpi, indicating that the increase in total nodule
166 mass reflects growing nodules rather than more frequent nodulation (Fig. S3).
167 These total dry mass measurements appeared consistent with Δ*hpnH* nodules "catching up" to
168 wild type, so we sought to independently verify this interpretation by measuring the radii of individual
169 nodules on ten plants for each strain at 40 dpi (Fig. 2e,f). From these data we determined that although
170 *average* nodule sizes (and, by extension, the total nodule mass) did become similar between strains by
171 this time point (0.73 vs. 0.88 mm average radii), their underlying distributions were markedly distinct.
172 Wild-type nodule radii appear to form a roughly normal distribution, whereas the Δ*hpnH* nodule radius
173 distribution is bimodal, consisting of a subpopulation of small nodules with small radii (<0.5 mm) that are
174 rarely observed in wild type, as well as a second, larger subpopulation that has a similar median radius as
175 wild type but is skewed towards larger radii (>1.5mm). These data demonstrate that the small-nodule
176 phenotype of Δ*hpnH* persists throughout a 40 dpi time course, but is compensated by greater size
177 heterogeneity, in which a handful of "mega" nodules offset smaller nodules over time.
178

179 *Δ*hpnH *nodule size heterogeneity reflects variable nodule growth rates*

180 The static measurements described above were insufficient to evaluate our hypothesis that
181 Δ*hpnH* nodule growth is aborted, because we could not infer from these assays whether the small
182 nodules observed at 24 (Fig. 1) and 40 (Fig. 2) dpi represent the same population, or whether they simply
183 began growing at different times. To better evaluate the possible mechanisms of the Δ*hpnH* nodule size
184 defect, we studied the kinetics of single nodule development. Beginning one week after inoculation of *A.*
185 *afraspera* plants with either wild type or Δ*hpnH*, we collected images of entire plant roots every 3-5 days
186 up to ~40 days post-inoculation (Fig. S4, S5). From these images, we identified nodules that were clearly
187 visible (*e.g.* not obscured by lateral roots or more recently emerged nodules) in at least five time points
188 (Fig. 3a) and measured their radii. We then calculated nodule volumes by approximating nodules as
189 spheres and plotted the volume of the tracked nodules over time. While we again observed that many
190 Δ*hpnH* nodules were smaller at 40 dpi than any of the wild type nodules, we also found that nodule
191 growth was highly variable both within and between strains (Fig. 3b,c).

192 To describe this heterogeneity, we employed a simple framework for quantifying nodule
193 development. We describe nodule growth by the following variables: the time (t_i) of the initial intracellular
194 infection event and the volume of the nascent nodule (V_i), equivalent to the volume of one infected *A.*
195 *afraspera* cortical cell; the time (t_{min}) and volume (V_{min}) at which a clearly visible, spherical nodule has
196 developed; the rate of growth of a nodule once it has become visible (dV/dt); and the time (t_{max}) and
197 volume (V_{max}) of a nodule when its growth has stopped (Fig. 3d). To calculate these variables, we fit each
198 nodule's growth over time to three different growth models: exponential, quadratic, and a generalized
199 logistic (*e.g.* sigmoidal) equation commonly used for plant growth[32,33] (see Methods for complete
200 details). Sigmoidal models generally provided the best fit to the experimental data, so these models were
201 used for growth parameter calculation (Fig. 3e; Fig. S6, S7).

202 The growth rates of Δ*hpnH* nodules were lower on average than wild-type nodules (Fig. 3f), with
203 roughly a third of tracked nodules exhibiting growth rates lower than observed for wild type by 40 dpi
204 (<0.1 mm^3/dpi). We noted that this was the same fraction of nodules as in the subpopulation of nodules
205 with smaller-than wild type radii at 40 dpi (Fig. 2e; Fig. 3g), and indeed, the subpopulation of nodules with
206 lower-than-wild-type growth rates and small nodule sizes are the same (Fig. 3h). Additionally, we found

207 that the growth rate of a nodule and its maximum size are positively linearly correlated for both strains,
208 with Pearson coefficients of ~0.64 ($p<10^{-9}$) for wild type and ~0.75 ($p<10^{-15}$) for Δ*hpnH*. We interpret these
209 data to suggest that host proliferation is slower in a subset of nodules infected with Δ*hpnH*, and that this
210 at least partially accounts for the low final volume of these nodules.

211 We also noted that the Δ*hpnH* nodule sizes at 40 dpi differed between these single-nodule
212 volume measurements (Fig. 3g) and our previous 40 dpi end-point measurements of nodule radii (Fig.
213 2e), in that we did not observe larger-than-wild-type "mega" nodules in the single-nodule dataset. This
214 discrepancy likely reflects the smaller sample size in our single-nodule tracking experiments (84
215 compared to 268 end-point nodules), and the low frequency of "mega" nodule formation. To verify this, we
216 selected 10,000 random subsets of 84 nodules from the 268 Δ*hpnH* nodules shown in Figure 2e,
217 converted the nodule radii to volumes, and found that there is no statistically significant difference
218 ($p<0.05$) between a random subset of Fig. 2e and the Δ*hpnH* single-nodule tracking data in ~92%
219 (9184/10000) of cases. Thus the differences in nodule size distributions in Figure 3g and Figure 2e are
220 consistent with sampling error.

221 We also used nodule growth fitting to test our hypothesis that the growth period is shorter for
222 Δ*hpnH* nodules compared to wild type – *e.g.* that growth stops prematurely. We estimated the window of
223 maximum growth as the time required for a nodule to increase from 10% to 90% of its final volume.
224 Neither the time at which a nodule reaches 90% of its maximum volume, t_{max}, nor the window of
225 maximum growth differs significantly between Δ*hpnH* and wild type (Fig. S8a,b). The window of maximum
226 growth for each nodule is also uncorrelated with their final volume or growth rate, indicating that small
227 nodules are not prematurely aborted; rather, their growth periods are similar to larger nodules (Fig. S9a-
228 d).

229 To better understand the subpopulation of small, slow-growing Δ*hpnH* nodules, we sectioned
230 nodules from Δ*hpnH*-inoculated plants at 40 dpi and separated the small (<0.5 mm radius) subpopulation
231 of nodules from all others (>0.5 mm radius). We stained sections with SYTO9, PI and Calcofluor and
232 imaged the sections with confocal microscopy. We found that while most small Δ*hpnH* nodules contained
233 a single, continuous infection zone, a large fraction were un- or under-infected with bacteria, often
234 exhibiting disorganized central infection zones (~37%; 28/75) (Fig. 4a; Fig. S10). Of the fully infected

235 small Δ*hpnH* nodules, some contained primarily PI-stained, likely dead bacterial cells (~25%; 12/47) (Fig.
236 4a; Fig. S10). Similarly high proportions of under-infected nodules or nodules primarily occupied with
237 membrane-compromised bacteria did not occur in larger Δ*hpnH* nodules harvested at the same time
238 point; however, we did notice that many of these nodules contained noticeably fragmented infection
239 zones (Fig. 4b; Fig. S11).

240 We also compared the subpopulation of small Δ*hpnH* nodules at 40 dpi to two wild-type nodule
241 populations: similarly small nodules harvested at 10 and 25 dpi (Fig. 4a; Fig S12; Fig. S13), and nodules
242 harvested at the same 40 dpi time point (Fig. 4b; Fig. S14). Again, we found that higher proportions of
243 under-infected nodules and nodules containing primarily membrane-compromised bacteria were unique
244 to the Δ*hpnH* small-nodule subset. It is interesting that these phenotypes were not apparent for Δ*hpnH*
245 nodules in the previously analyzed 24 dpi time point (Fig. S1), in which nodules that are under-infected or
246 primarily occupied by dead bacteroids are rare. It is possible we did not capture these phenotypes
247 because they occur infrequently in the overall nodule population; infection zones with primarily dead
248 bacteroids occur in only 12/75 small Δ*hpnH* nodules in Fig. S10, and small (<0.5 mm radius) nodules
249 themselves make up only a third of all Δ*hpnH* nodules at 40 dpi. An alternate conclusion from these data
250 is that poor Δ*hpnH* survival or infection density is only apparent at later stages in development, indicating
251 inherently poor persistence of Δ*hpnH* within host cells and/or premature nodule senescence.
252

253 *Δ*hpnH *is delayed in early plant-symbiont association*

254 Our final hypothesis for the origin of small nodules, that the onset of nodule growth is delayed,
255 proved more difficult to address. The "true" beginning of nodule formation is the time when the first *A.*
256 *afraspera* cortical cell is infected, t_i (Fig. 3d). However, this initial infection event is not visible at the root
257 surface, and it is difficult to extrapolate from sigmoidal models in which the growth curves approach the
258 initial volume $V_i \sim 0$ mm^3 asymptotically. As a proxy for t_i, we defined three alternate t_{min} as the times at
259 which nodules reached three arbitrarily small volumes: V = 0.05 mm^3, V = 0.1 mm^3, and V = 0.2 mm^3.
260 When t_{min} is defined by V = 0.05 mm^3 or 0.1 mm^3, t_{min} could not be accurately calculated for all nodules, as
261 the sigmoidal models sometimes predicted $t_{min} < 0$ (an impossible value) (Fig. S8c). These nodule
262 volumes are also too small to be seen on the root surface, and we had no experimental means to

263 determine the accuracy of the calculations in this low-volume regime. When t_{min} is defined by V = 0.2 mm^3
264 (the smallest nodule volume that we could identify in our single-nodule tracking assays), there is a small
265 but statistically significant increase for Δ*hpnH* relative to wild type (Fig. S8c). To independently verify this
266 delay in visible nodule appearance, we inspected the roots of 20 wild type- and 20 Δ*hpnH*-inoculated
267 plants over 40 dpi and recorded the number of visible nodules per plant each day. We found a more even
268 distribution of observed t_{min} for Δ*hpnH* relative to wild type, with a 1-3 day shift in the most frequent dpi.
269 Surprisingly, we also found that the formation of new nodules is periodic, with a new "burst" of nodules
270 emerging roughly every 18 days (Fig. 3i). This periodicity of nodule emergence appears to be similar
271 between strains.

272 While the slight t_{min} delay for Δ*hpnH* is consistent with longer times required to initiate the
273 symbiosis (*e.g.* root surface colonization, invasion of the root epidermis and cortex, and intracellular
274 uptake), it is also possible that a delay in t_{min} simply reflects a lower rate of nodule growth immediately
275 after the first host cell is intracellularly infected. To address this, we compared the calculated value of t_{min}
276 (defined by V = 0.2 mm^3) to the maximum growth rates and volumes for each nodule (Fig. S9e,f). We did
277 not find that the subpopulation of nodules with lower growth rates and final volumes than wild type was
278 more likely to have a later t_{min}, supporting the interpretation that the delay in t_{min} of Δ*hpnH* could be due to
279 a separate initiation defect, although it is also possible that the growth rates of emergent nodules and
280 nascent nodule primordia are not strictly related. Interestingly, t_{min} is also not correlated with the period in
281 which maximum nodule growth occurs, such that later-emerging nodules have similar periods of growth
282 as nodules formed within a few dpi (Fig. S9g,h). This indicates that although the appearance of new
283 nodules is restricted to narrow, periodic time frames (Fig. 3i), once a nodule has entered its maximum
284 growth phase, its continued growth is comparatively unconstrained.

285 To further verify the slight delay in the initiation of the symbiosis for Δ*hpnH* relative to wild type,
286 we performed competition assays using a standard fluorescence labeling approach. We first generated
287 Δ*hpnH* and wild-type strains expressing chromosomally-integrated fluorescent proteins, and then we co-
288 inoculated *A. afraspera* with different ratios of these two strains. As control experiments, we also co-
289 inoculated each tagged strain with its untagged counterpart, in order to determine the effect of fluorescent
290 protein overexpression on each strain's competitiveness. After >40 dpi we measured the size of nodules

291 on plants inoculated with each strain combination and ratio, then sectioned and fixed nodules for imaging.
292 Although we expected each nodule to contain a clonal population based on previous work[25,27], the
293 majority of nodules appeared to contain a mixture of both strains (Fig. 5a; Fig. S15-S19). We instead
294 quantified the relative abundance of each strain in each nodule by fluorescence imaging; in our control
295 experiments, in which only one fluorophore-expressing strain was present, a DNA dye (either SYTO9 for
296 mCherry-expressing bacteria or PI, which stains all cells in fixed samples, for GFP-expressing bacteria)
297 was used to label all bacteria.

298 Both WT-YFP and Δ*hpnH*-mCherry were significantly out-competed by their corresponding
299 untagged strains, with higher proportions of tagged strains correlating with lower bacterial DNA
300 abundance and smaller nodule and/or infection zone sizes (Fig. 4b-c; Fig. S21-22). Additionally, plants
301 co-inoculated with untagged-Δ*hpnH* and Δ*hpnH*-mCherry were significantly shorter than plants inoculated
302 with untagged-Δ*hpnH* only, suggesting Δ*hpnH*-mCherry is symbiotically defective (Fig. S20). These
303 effects of fluorophore overexpression made it difficult to interpret our WT-YFP and Δ*hpnH*-mCherry
304 competition data (Fig. S23), so we developed an alternative, antibiotics-based method to study the timing
305 of early symbiotic initiation.

306 First we sought antibiotics that were effective against *B. diazoefficiens* but would minimally affect
307 *A. afraspera* growth. We selected three antibiotics (100 µg/ml streptomycin, 100 µg/ml kanamycin, and 20
308 µg/ml tetracycline) and treated non-inoculated plants with these antibiotics for two weeks, alone and in
309 combination. After this treatment, we found that neither kanamycin nor streptomycin, nor the combination
310 of the two, significantly affected plant appearance, shoot height, or root and shoot dry masses compared
311 to untreated controls (Fig. S24). Plants treated with tetracycline were noticeably more yellow in color,
312 indicating chlorosis, and the roots and plant medium became brown; these plants also had lower shoot
313 and root dry masses than untreated plants (Fig. S24).

314 Next, because the Δ*hpnH* strain is more sensitive to antibiotics than wild type[11], we tested
315 various concentrations of the non-plant-perturbing antibiotics streptomycin and kanamycin to identify
316 concentrations that would result in the same rates of cell death for both strains. We inoculated plant
317 growth media with wild type or Δ*hpnH* to the same concentrations and under the same environmental
318 conditions as in plant inoculation experiments. The wild-type culture was supplemented with 100 µg/ml

319 streptomycin plus 100 µg/ml kanamycin, and Δ*hpnH* cultures were supplemented with decreasing
320 concentrations of these antibiotics: 75, 50 and 25 µg/mL each. Samples of the cultures were then
321 collected, serially diluted and added to PSY plates to estimate colony-forming units (cfus) per mL over
322 time. At 50 µg/mL kanamycin plus 50 µg/mL streptomycin, the rate of decrease in cfus/mL for Δ*hpnH* was
323 equivalent to that of wild type treated with 100 µg/ml kanamycin plus streptomycin (Fig. 5d).
324 Finally, we inoculated 40 plants each with wild type or Δ*hpnH* and added streptomycin or
325 kanamycin to 100 µg/mL each or 50 µg/mL each, respectively, at various points post-inoculation. After 40
326 days we counted the number of nodules per plant, and found that antibiotics were able to block nodule
327 formation over a ~50% longer window in Δ*hpnH* compared to wild type (Fig. 5e). The decrease in nodules
328 formed at different antibiotic treatment time points was also evident in the overall appearance of the
329 plants (Fig. 5f). These results suggest that Δ*hpnH* requires more time on average to reach the
330 intracellular stage of the symbiosis, at which point we presume that the bacteria are protected from
331 antibiotic by the host cells. These data are consistent with Δ*hpnH* requiring more time to colonize the root
332 surface, invade the root epidermis, and/or be internalized by host cells.
333
334 *Extended hopanoids support surface attachment and motility*
335 Because we found that expression of genetic tags in wild type and Δ*hpnH* perturbed their
336 symbiosis with *A. afraspera*, and therefore we could not confidently track these strains *in planta*, we used
337 an *in vitro* approach to study two steps in the initiation of the symbiosis: (1) bacterial motility toward or
338 along the *A. afraspera* root, and (2) stable attachment of bacteria to the root surface[20]. To determine
339 whether Δ*hpnH* is less motile than wild type, we inoculated low-agar, PSY plates with Δ*hpnH* or wild type
340 and measured the rate of zone of swimming over time. We observed that diameter of motility was
341 reduced in Δ*hpnH* compared to wild type (Fig. 6a-b), consistent with a swimming motility defect; however,
342 because we have previously shown that Δ*hpnH* grows more slowly in this medium than wild type[11], we
343 could not rule out the possibility that slower zone expansion simply reflects a longer doubling time.
344 To investigate the nature of the plate motility defect, we studied the motility of single *B.*
345 *diazoefficiens* cells. We inoculated cells that have been incubated in PSY liquid medium into a glass
346 bottom steril flow cell with 100µL of each strain and recorded the trajectories of single cells near the glass

surface at 5 ms time resolution. The cells were tracked using an in-house tracking software in MATLAB,[34] in which actively swimming cells are defined as having super-diffusive motion and a trajectory radius of gyration greater than 2.5 μm, and we calculated mean swimming speeds for each cell using a moving window average over the cell's full trajectory (see Methods for details). In agreement with our low-agar swimming plates, we found a significantly lower ($p < 0.0001$) fraction of motile cells for Δ*hpnH*, $N_{\Delta hpnH} = 65 \pm 29$, compared to wild type, $N_{wt} = 368 \pm 60$, in PSY medium (Fig. 6c), although the average mean-speed among motile cells were similar between strains, $\langle V \rangle_{\Delta hpnH} = 24.83 \pm 7.0$ μm/sec and $\langle V \rangle_{wt} = 22.75 \pm 6.7$ μm/sec (Fig. 6d). Because the composition of PSY differs greatly from that of the plant growth medium (BNM), we repeated these assays in BNM supplemented with arabinose. Under this condition, we again observed a lower fraction of motile Δ*hpnH* cells than wild type, ($N_{\Delta hpnH} = 54 \pm 59$, $N_{wt} = 450 \pm 310$) (Fig. 6e), with similar mean speeds between strains and across media conditions (Fig. 6d,f). These results are consistent with a delay in the initiation of the Δ*hpnH* symbiosis with *A. afraspera* due to a lower occurrence of motile bacterial cells, indicating that the effect of extended hopanoids is likely regulatory and upstream of the workings of the flagellum.

We next tested the surface attachment capabilities of Δ*hpnH* and wild type by incubating dense bacterial cultures on glass coverslips and quantifying the fraction of the surface covered with stably adhered cells after two hours. In PSY medium, both strains adhered poorly, and there was no significant difference in their attachment efficiencies (Fig 6g; Fig. S25). In BNM supplemented with arabinose, both strains adhered to glass better than in PSY, and Δ*hpnH* attachment levels were significantly lower than wild type (Fig. 6g; Fig. S25). The origin of the differences in surface attachment between PSY and BNM is unclear. While this result may indicate that the surface attachment machinery of *B. diazoefficiens* functions better in BNM, we cannot exclude the interpretation that because PSY is more rich than BNM, peptides and other components of PSY are more likely to interact with the glass surface to occlude or disfavor bacterial attachment. Regardless, the lower adherence of Δ*hpnH* in BNM data suggest that Δ*hpnH* may adhere to the *A. afraspera* root surface less efficiently than wild type, and that this also may contribute to the delay in the initiation of the symbiosis.

Discussion

375 Hopanoids are well-established mediators of bacterial survival under stress, and previously we
376 showed that the capacity for hopanoid production is enriched in plant-associated environments[13] and
377 required for optimal *Bradyrhizobia-Aeschynomene* spp. symbioses[10,11]. Here we performed a detailed,
378 quantitative evaluation of the extended hopanoids' roles in the *Bradyrhizobium diazoefficiens-*
379 *Aeschynomene afraspera* symbiosis. Our results provide evidence that extended hopanoids' effects are
380 pleiotropic and span the stages of root nodule biogenesis. We identify specific extended-hopanoid
381 dependent processes that will provide a foundation for more detailed mechanistic work (Fig. 7). Our
382 description of the kinetics of nodule growth in *A. afraspera*, both for single nodules and across the root
383 system, more generally suggests new hypotheses about the cell and developmental biology of nodule
384 formation in this organism.

385 By tracking the development of individual root nodules, we found that the initial emergence of root
386 nodules is delayed in plants inoculated with extended hopanoid mutants. *In vitro*, extended hopanoids
387 appear to support both the efficiency of surface attachment and the proportion of motile cells in plant
388 growth medium, suggesting that delayed root nodule emergence may result from fewer cells swimming
389 and attaching to the root surface in the initial bacteria-host contact (Fig. 7a-b). At later stages in root
390 nodule development, roughly a third of nodules infected with extended hopanoid mutants grow at slower
391 rates than with wild type and consequently exhibit low volumes when fully mature. Many of these small
392 nodules contain reduced densities of symbionts throughout their infection zones; extended hopanoid
393 mutant nodules with wild-type nodule volumes can also have lower symbiont loads, due to infection zone
394 fragmentation. The origin of this under-infection phenotype is unclear from our experiments. One
395 explanation is that host cells in the nodule primordium either internalize fewer cells from the extracellular
396 environment, or that primordial symbiosomes duplicate or are segregated less effectively, and this
397 phenotype is simply propagated as nodules develop (Fig. 7d). Alternatively, low symbiont densities may
398 reflect symbiont degradation in a previously fully-infected nodule (Fig. 7e).

399 What mechanisms might underpin these extended hopanoid mutant phenotypes? Through a
400 biophysical lens, the effects of extended hopanoid loss in the *B. diazoefficiens-A. afraspera* symbiosis
401 could be viewed purely as consequences of less rigid *B. diazoefficiens* membranes. The fraction of motile
402 cells in *E. coli* populations has been suggested to be sensitive to changes to the mechanical properties of

403 the outer membrane[35], and membrane-based mechanotransduction is required by diverse bacteria to
404 stimulate extracellular matrix production and cement their attachment to surfaces[36,37]. Subsequent
405 progression of bacteria into the root interior through small (micron- to submicron-diameter) channels may
406 also be hindered by a less rigid *B. diazoefficiens* membrane, as growth rates under similarly confined
407 spaces *in vitro* have been shown to be positively correlated with membrane rigidity in *E. coli* and *B.*
408 *subtilis* models[38,39]. Though not much is known about the mechanical requirements of formation and
409 propagation of the symbiosome, bacterial membrane rigidity may be relevant in this context as well. For
410 example, the maintenance of single-bacteroid-containing symbiosomes within host cells (presumably
411 requiring coordination of bacteroid division with division of the surrounding host-derived membrane)
412 implies a mechanical linkage between the bacteroid and peribacteroid membranes, which may be
413 sensitive to changes in bacteroid membrane rigidity. NCR peptide-directed reprogramming of bacteroids
414 could also be less effective in *B. diazoefficiens* with less rigid membranes, increasing bacteroid
415 permeability to peptides or peptide-induced bacteroid lysis. While intriguing, these mechanics-based roles
416 for extended hopanoids are difficult to verify given how little information is available on the biophysical
417 aspects of legume-microbe interactions. Future work in this area would enrich our understanding of how
418 intracellular bacterial infections operate in native multicellular hosts.

419 Other potential extended hopanoid-mediated effects on the symbiosis include regulation of
420 membrane-based processes, such as motility, oxidative phosphorylation, the early legume-rhizobia
421 dialogue or transport across the symbiosome membranes. Specifically, the loss of HoLA from the outer
422 membrane in the *B. diazoefficiens* Δ*hpnH* mutant is likely to disrupt processes involving lipid A, which has
423 previously been shown to enhance bacterial fitness in *A. afraspera* hosts[40]. Identifying the enzyme(s)
424 responsible for the attachment of hopanoids to lipid A will be necessary to determine how much HoLA
425 contributes to the Δ*hpnH* phenotypes we observed in this work, as well as the universality of these
426 phenotypes to other host-bacteria interactions. While many hopanoid-producing bacteria are host-
427 associated, so far HoLA has only been found in the *Bradyrhizobiaceae*.

428 Regardless of the underlying mechanisms for extended hopanoids, it is curious that their absence
429 is not a death knell for the *B. diazoefficiens-A. afraspera* symbiosis at any stage. In our *in vitro* studies,
430 although fewer motile cells were present in the extended hopanoid mutants, mean speeds among motile

431 Δ*hpnH* cells were indistinguishable from wild type. While we cannot rule out more subtle defects in the
432 direction of the movement or in chemotaxis, the identical mean speeds suggest that once motility of
433 Δ*hpnH* cells is induced, their motility systems function properly. Similarly *in planta*, Δ*hpnH* nodules
434 developing at wild-type rates and reaching average wild-type volumes did occur – and, in the case of
435 "mega" nodules, some exceeded their wild-type counterparts. Why do Δ*hpnH* populations form two
436 distinct populations (wild-type-like or defective) rather than falling on a continuous distribution of
437 behavior? Bimodality in a population can reflect a switch-like, or threshold-based, regulation, and perhaps
438 in the Δ*hpnH* strain, a fraction of cells cannot support levels of signaling or biochemical events above the
439 appropriate threshold for proper function. Populations within Δ*hpnH* also may differ in the extent to which
440 extended hopanoid loss is compensated. In *Methylobacterium extorquens* and *Rhodopseudomonas*
441 *palustris*[41,42], hopanoid loss results in upregulation of other membrane-rigidifying lipids including
442 carotenoids and cardiolipins, and in other plant-microbe systems, lipid exchange between hosts and
443 microbes has been observed[43], suggesting that Δ*hpnH* mutant success at a given nodulation site may
444 relate to the local availability of exogenous plant steroids or structurally similar metabolites.
445 Beyond hopanoids, our results provide insight into the developmental control of nodule formation
446 by *A. afraspera* hosts. Although the time of emergence, growth rate and window of growth of any specific
447 nodule appears to be stochastic, the extent to which nodulation is permitted across the entire root system
448 is tightly determined. Host control of nodule numbers, known as the autoregulation of nodulation (AON),
449 is a well-established phenomenon[44], and a new, expanded model of AON derived from studies of *Lotus*
450 *japonicum* has recently been published[45]. In this model, the root-specific TOO MUCH LOVE (TML)
451 protein is a key negative regulator of nodule formation. In the absence of rhizobia, a microRNA (miR2111)
452 produced in plant leaves translocates to roots to suppress TML, poising uninfected plants in a nodulation-
453 susceptible ("ON") state. When rhizobia begin to infect the plants, a negative feedback loop is initiated,
454 beginning with the local production of CLE-family peptides. These CLE peptides then translocate to the
455 shoot and activate a receptor protein at the shoot apex known as HAR1. HAR1-mediated signaling blocks
456 the miR2111 shoot-root translocation, de-repressing TML to create a nodulation-resistant ("OFF") state.
457 The general features of this AON pathway are conserved across legumes (reviewed in [44]), and
458 although AON has not been specifically investigated in *A. afraspera*, our results suggest a similar

459 mechanism is at play. Our observation that the wild-type *B. diazoefficiens-A. afraspera* symbiosis is
460 characterized by an initial 2-3 day burst of nodulation followed by a sharp drop-off is consistent with an
461 initial "ON" state that is inhibited by a negative feedback loop with a several-day activation time. What is
462 most striking about nodule formation in *A. afraspera* is that nodulation-susceptible "ON" states appear to
463 be reactivated at fixed 18-day intervals, and that re-activation is unrelated to systemic nitrogen fixation
464 efficiency: at the end of the first 18 dpi cycle, Δ*hpnH* nodules fix considerably less nitrogen than wild type,
465 yet the timing and distribution of nodulation in the second cycle is unchanged. This both suggests that
466 there is a fixed oscillation between nodulation-susceptible and nodulation-resistant states in *A. afraspera*,
467 and that the timing of the oscillation is determined by the dynamics of the underlying regulatory
468 mechanisms (*e.g.* the rates of synthesis, activation/inhibition, and translocation of specific regulatory
469 molecules). Thus, we predict that a systems-level analysis of regulatory factor dynamics will be key to
470 elucidating the nodulation re-activation pathway, as will a more detailed analysis of nodulation timing in
471 other, model legumes. Specifically, it will be interesting to determine whether re-activation occurs simply
472 by dampening of the negative feedback pathway as inhibitory molecules reach the end of their lifetimes,
473 or if it involves an additional positive feedback mechanism that simply requires a longer activation time.
474 Since the systemic control of nodulation is insensitive to nitrogen fixation, it is possible that *A.*
475 *afrapera* plants maximize overall nitrogen fixation through the local regulation of nodule organogenesis. It
476 is already known that nitrogen-based signaling can locally regulate nodule formation in other legume
477 hosts (reviewed in [44]), albeit in the context of nodule growth inhibition by increased soil nitrogen
478 availability. We have found that the key variable that determines the final size of a nodule (and thus it
479 potential for symbiotic productivity) is the rate of nodule growth and, given that rates of growth are lower
480 in the less-productive Δ*hpnH* strain than wild-type, this could be coupled to the nodule's fixed nitrogen
481 output. Alternately, nodule growth rates may relate to the density and survival of symbionts present,
482 perhaps by indirect sensing of bacteroid-produced signals. An intriguing possibility is that bacteroids
483 secrete mitogenic compounds, such as phytohormones, to directly influence host cell division rates. *B.*
484 *diazoefficiens* has been shown to synthesize the majority of known phytohormones in pure culture[46],
485 and in *Frankia* symbionts, extended hopanoid levels may be correlated with amount of the auxin
486 phytohormome phenyl-acetic acid (PAA)[47]. It has also been shown that *B.* ORS285 mutants that cannot

487 produce cytokinin phytohormones exhibit slower nodulation kinetics and smaller nodule sizes in
488 *Aeschynomene indica* hosts[48]. The full extent to which primordia and infection zone growth are
489 dependent on bacteroid-secreted mitogens or nitrogen fixation productivity, and through what
490 mechanisms, will be an active area of future research.

491 On a technical level, our results underscore the importance of identifying the most informative,
492 least perturbing tools for interrogating legume-microbe symbiosis. Employing quantitative single-nodule
493 and single-cell approaches rather than bulk measurements were essential for uncovering the diverse
494 phenotypes of the *B. diazoefficiens* extended hopanoid mutants and yielded unexpected information on
495 regulation of nodule development by *A. afraspera*. We have also shown the limitations of introducing
496 overexpressed genetic tags into bacteria. While use of these tags has undoubtedly enhanced our
497 understanding of legume-microbe symbiosis[49], they may not fully capture the behavior of native
498 organisms, and in this work we provide a model for evaluating the extent of these genetic tags' effects.
499 Additionally, our work is one of many to emphasize the importance of appropriate culture models for
500 mimicking the host environment, as the Δ*hpnH* surface attachment defect was observed in plant growth
501 medium but not in a standard richer medium. Recent work has suggested that culturing rhizobia in the
502 latter is correlated with an increase in mutations of symbiosis-associated genes[50], raising questions
503 about the utility of rich medium cultures in symbiosis work overall. A more detailed analysis of the host
504 environment, including the full milieu of root exudates[51], available carbon sources[52] and trace metals
505 specific to each legume, will improve *in vitro* models of legume-bacteria interactions.

506 Finally, beyond opening up future work on the mechanism of hopanoids in motility and
507 attachment, this work highlights aspects of the development of *A. afraspera* symbioses most in need of
508 more detailed analysis. Key questions raised in this study include how relevant the biophysical
509 environment of the root invasion is for the mode and the efficiency of progressive bacterial invasion; how
510 is a high density of symbiosomes established and maintained within infected nodule cells; what factors
511 regulate the mitotic index of a nodule, and how dynamic are these indices; and how the answers to all of
512 these questions change in the presence of competition between multiple strains with different symbiotic
513 nitrogen-fixation capacities. Addressing these questions in the *Aeschynomene-Bradyrhizobia* symbiosis
514 will expand our knowledge of the diversity of approaches to establishing persistent, intracellular

515 infections, and perhaps provide a better "blueprint" for engineering novel beneficial plant-microbe
516 associations. These future studies may also prove to be ecologically significant, as African
517 *Aeschynomene* spp. are native to regions with the world's poorest food security and nitrogen fertilizer
518 accessibility and thus in greatest need of better symbiotic nitrogen fixation[53], and *Bradyrhizobia* are
519 dominant in harsh, warm soils predicted to be more prevalent in a changing global climate[54].
520
521 **Methods**
522
523 B. diazoefficiens *culture and strain generation*
524 *B. diazoefficiens* hopanoid biosynthesis mutants were generated previously[11]. For construction
525 of YFP- and mCherry-expressing strains, fluorophore expression vectors pRJPaph-YFP and pRJPaph-
526 mCherry[27] were provided as a gift from Prof. Dr. Hans-Martin Fischer (ETH Zurich). These vectors were
527 introduced into *B. diazoefficiens* by conjugation with the β2155 DAP auxotroph strain of *E.coli*, using the
528 following protocol: *B. diazoefficiens* wild type and Δ*hpnH* were grown in 5 mL PSY medium[55] at 30°C
529 and 250 rpm to an OD_{600} of ~1.0 (wild type) or of 0.5-0.8 (Δ*hpnH*). β2155 strains carrying pRJPaph
530 vectors were grown to an OD_{600} of 0.5-0.8 in 5 mL LB supplemented with 10 µg/mL tetracycline and 300
531 µm DAP at 37°C and 250 rpm. Both *B. diazoefficiens* and β2155 donor cultures were pelleted at 3250 x g
532 for 30 minutes, washed three times in 0.9% sterile saline, and resuspended in 0.9% sterile saline to a
533 final OD_{600} of 1.0. *B. diazoefficiens* strains and β2155 donor cells were combined at a 4:1 ratio,
534 respectively, and mixed by repeated pipetting. Aliquots (50 µl) of these 4:1 mixtures were dropped to PSY
535 plates supplemented with 300 µm DAP, dried in a biosafety cabinet, and incubated for 48 hours at 30°C.
536 Conjugation pastes were then removed from plates and resuspended in 5 mL sterile saline, pelleted at
537 3250 x g for 30 minutes and washed twice, in order to remove residual DAP. Washed cells were pelleted
538 a final time and resuspended to 200 µl in 0.9% sterile saline and plated onto PSY plates supplemented
539 with 20 µg/mL (wild type) or 10 µg/mL (Δ*hpnH*) tetracycline. Colonies appeared after 7-10 days (wild type)
540 or 10-14 days (Δ*hpnH*) and were streaked onto fresh PSY/tetracycline plates, then screened for
541 fluorescence using a Lumascope 720 fluorescent microscope (Etaluma). Fluorescent colonies were then
542 sequenced to verify insertion of the pRJPaph vectors into the *scoI* locus.

543

544 A. afraspera *cultivation and inoculation with* B. diazoefficiens

545 *A. afraspera* seeds were obtained as a gift from the laboratory of Dr. Eric Giraud (LSTM/Cirad,
546 Montpelier, France). Seeds were sterilized and scarified by incubation in 95% sulfuric acid at RT for 45
547 minutes, followed by 5 washes in sterile-filtered nanopure water and a second incubation in 95% ethanol
548 for 5 minutes at RT. After ethanol treatment seeds were washed 5X and incubated overnight in sterile-
549 filtered nanopure water. Seeds were then transferred to freshly poured water/agar plates using sterile,
550 single-use forceps in a biosafety cabinet, and germinated for 24-72 hours in the dark at 28-32°C.

551 Seedlings were then placed in clear glass test tubes containing 100 mL of sterile, nitrogen-free
552 Buffered Nodulation Medium (BNM)[56] and grown for 7-10 days in plant growth chambers (Percival)
553 under the following settings: 28°C, 80-90% humidity, and 16 hour photoperiod under photosynthetic light
554 bulbs (General Electric) emitting ~4000 lumens/ft^2. In parallel, *B. diazoefficiens* strains were grown in 5-10
555 mL PSY liquid culture at 30°C and 250 rpm to stationary phase (OD_{600} > 1.4). Stationary phase cultures
556 were diluted into PSY one day prior to plant inoculation to reach an OD_{600} of ~0.8 at the time of
557 inoculation. OD_{600} ~ 0.8 cultures were pelleted at 3250 x g for 30 minutes at RT, washed once in PSY,
558 then resuspended in PSY to a final OD_{600} of 1.0. Resuspended *B. diazoefficiens* cultures were directly
559 inoculated into the plant medium in a sterile biosafety cabinet; 1 mL of OD_{600}=1.0 culture was added per
560 plant. Inoculated plants were then returned to growth chambers and maintained for the times indicated for
561 each experiment. For longer experiments (lasting longer than ~30 days post-inoculation), plant growth
562 tubes were refilled with sterile-filered nanopure water as needed. To minimize cross-contamination,
563 inoculated plants and non-inoculated plants were cultivated in separate growth chambers, and growth
564 chambers were sterilized with 70% ethanol followed by UV irradiation for at least 24 hours between
565 experiments.

566

567 *Acetylene reduction experiments*

568 Individual plants were transferred to clear glass 150 mL Balch-type anaerobic culture bottles containing
569 15 mL BNM medium and sealed under a gas-tight septum. After sealing, 15 mL of headspace gas (10%
570 of the culture bottle volume) was removed and replaced with 15 mL of acetylene gas (Airgas). Plants in

571 culture bottles were incubated in the light at 28°C in growth chambers for 3-6 hours. A 100 µl sample of
572 the headspace gas was removed using a gas-tight syringe (Hamilton), and this sample was injected and
573 analyzed for ethylene signal intensities using a Hewlett Packard 5890 Series II GC with Hewlett Packard
574 5972 Mass Spectrometer with a 30mx0.320mm GasPro Column (Agilent Technologies) and a 2 mm ID
575 splitless liner (Restek Corporation). Following acetylene reduction measurements, plants were removed
576 from jars and plant shoot heights and number of nodules per plant were recorded. When nodule dry mass
577 measurements were performed, nodules were harvested with a razor blade, transferred into pre-weighed
578 Eppendorf tubes, dried at 50°C for a minimum of 48 hours, then weighed again.
579
580 *Live:Dead staining and imaging of nodule cross-sections*
581 Nodules were hand-sectioned with razor blades and immediately transferred into a fresh solution
582 of 5 µM SYTO9 (diluted 1:100 from a 500 uM stock in DMSO at -20°C; Thermo Fisher) and 0.02 mg/mL
583 (30 µM) propidium iodide (diluted 1:50 from a 1 mg/mL stock stored in water at 4°C; Thermo Fisher) in
584 PBS. Nodule sections were incubated in this SYTO9/propidium iodide solution at room temperature for 30
585 minutes in the dark with gentle shaking, washed 5X in PBS, and fixed in 4% paraformaldehyde (Electron
586 Microscopy Sciences) in PBS overnight in the dark at 4°C. Fixed sections were washed 5X in PBS and
587 transferred to a freshly prepared solution of 0.1 mg/mL Calcofluor White (Fluorescence Brightener 28;
588 Sigma) in PBS. The sections were incubated in the Calcofluor solution in the dark for 1 hour at RT with
589 gentle shaking and washed 5X in PBS to remove excess dye.
590 Prior to imaging, sections were transferred to 30 mm imaging dishes with 20 mm, #0 coverglass
591 bottoms (MatTek) and overlaid with sterile 50% glycerol. Nodule images were collected on a Leica TCS
592 SPE laser-scanning confocal (model DMI4000B-CS) using a 10X/0.3 NA APO ACS objective and solid-
593 state laser lines for fluorophore excitation at the following settings for each dye: Calcofluor, 405 nm
594 excitation/410-500 nm emission; SYTO9, 488 nm excitation/510-570 nm emission; PI, 532 nm
595 excitation/600-650 nm emission. These images were then processed to enhance brightness and contrast
596 in FIJI[57,58].
597
598 *Nodule diameter and volume measurements*

599 Inoculated *A. afraspera* root nodules were imaging using a high-definition Keyence VHX-600
600 digital microscope at 20X magnification. For end-point root nodule volume measurements at 40 days
601 post-inoculation, plants were removed from the growth chamber and imaged at RT on paper towels, then
602 discarded. Nodule diameters were measured using the line tool in FIJI and recorded using a custom FIJI
603 macro. For tracking nodule volumes over time, plants were serially removed from their growth chambers
604 and transferred to a plastic dish containing 150 mL of sterile BNM pre-warmed to 28°C. Images of
605 sections of the plant root were collected serially from the hypocotyl to the root tip. Following collection of
606 images, plants were immediately returned to their original growth tubes in the growth chamber. Plastic
607 dishes were sterilized for 10 minutes in 10% bleach, washed three times in sterile-filtered nanopure
608 water, sprayed with 70% ethanol/water, and air-dried before each new plant was imaged. A fresh aliquot
609 of sterile, pre-warmed BNM also was used for each plant. After the time course was completed, images of
610 entire plant root systems were reconstructed by eye for each plant at each time point. For nodules
611 appearing in at least five time points, nodule diameters were measured as described for the end-point
612 measurements and were converted to approximate volumes in R using the equation $V = 4/3\pi r^3$.
613
614 *Nodule growth curve fitting and analysis*
615 All analyses of nodule growth, and corresponding plots, were generated in R. For nodule growth
616 curve fitting, three model equations were used to identify the best fit, as follows:
617
618 (1) exponential function:

$$V = \boldsymbol{a}e^{-\boldsymbol{b}t} + \boldsymbol{c}$$

619
620 (2) quadratic function:

$$V = \boldsymbol{a}t^2 + \boldsymbol{b}t + \boldsymbol{c}$$

621
622 (3) generalized logistic function (expressed as a Richard's function with a time shift):
623

$$V = \frac{\boldsymbol{a}}{(1 + e^{-\boldsymbol{b}(t-\boldsymbol{c})})^{(\frac{1}{\boldsymbol{d}})}}$$

624

625 Calculation of the optimal parameter values for each equation (e.g. the values of **a**, **b**, **c**, and **d**) and the
626 standard error for each curve compared to the raw data were performed using the built-in function *nlm*() in
627 R. In some cases, *nlm()* could not produce a best-fit model without specifying initial values for the function
628 parameters. For exponential models, an equation of best fit could be successfully determined without
629 specification of initial values for parameters **a**, **b** and **c**. For quadratic models, initial parameter values
630 were required and were set to **a**=0, **b**=10 and **c**=0 for each nodule plot, after identifying these initial
631 parameter values as broadly optimal based on an initial parameter sweep of -50 to 50 for each plot. For
632 sigmoidal models, no broadly optimal initial values could be identified, so a parameter sweep was
633 performed for each plot with the initial value of **a** set to the maximum observed nodule volume (as **a**
634 describes the upper asymptote of the sigmoidal curve), **b** ranging from 0.1 to 1, **c** ranging from 0 to 10,
635 and **d** ranging from 0.01 to 1.0. In the sigmoidal plots, an initial point of (0,0) was added to the nodule
636 volume time series to improve fitting.

637 Because the sigmoidal model provided the best fits, extrapolation of nodule growth characteristics
638 was performed on sigmoidal models only. The maximum nodule volume, $\mathbf{V_{max}}$, is defined as the upper
639 asymptote of the sigmoidal growth curve, *e.g.* **a**. The nodule initiation time, $\mathbf{t_{min}}$, was defined in three
640 separate ways: the times at which the nodule volume is equal to 0.05, 0.1, or 0.2 mm^3 (*e.g.* through
641 solving 0.05, 0.1, or 0.2 = $\mathbf{a}/((1+e^{(-\mathbf{b}(t-\mathbf{c}))})^{(1/\mathbf{d})})$ for *t*). The maximum nodule growth rate, **dV/d*t***, was defined
642 as the average rate of growth (*e.g.* slope) between the time at which the volume is 10% of $\mathbf{V_{max}}$ and the
643 time at which the volume is 90% of $\mathbf{V_{max}}$. The time at which each nodule reaches its maximum size, $\mathbf{t_{max}}$,
644 was approximated as the time at which the volume is 90% of $\mathbf{V_{max}}$, since the "true" maximum volume is
645 asymptotic to the growth curve and is therefore never fully reached in the model.

646

647 *Competition assays*

648 mCherry-tagged Δ*hpnH* and YFP-tagged wild type *B. diazoefficiens* were grown to stationary
649 phase (OD_{600} > 1.4) in 10 mL PSY cultures supplemented with 20 µg/mL (wild type) or 10 µg/mL (Δ*hpnH*)

650 tetracycline; untagged strains were grown in PSY. On the day prior to inoculation, all strains were diluted
651 into 50-150 mL tetracycline-free PSY to reach an OD_{600} of ~0.8 at the time of inoculation. *A. afraspera*
652 plants were cultivated pre-inoculation in test tubes as described above, with the addition of covering the
653 growth tubes in foil to minimize the production of chlorophyll in the plant roots, which spectrally overlaps
654 with mCherry. At the time of inoculation, all cultures were pelleted at 3250 x g for 30 minutes at RT,
655 washed three times, then resuspended in PSY to a final OD_{600} of 1.0. A 10 mL culture of each strain ratio
656 for inoculation was generated a sterile 15mL Falcon tube; for example, for a 50:50 mixture of mCherry-
657 tagged Δ*hpnH* and YFP-tagged wild type, 5 mL of each strain was combined. These cultures were mixed
658 thoroughly by gentle pipetting, and 1 mL of the mixtures was added to directly to the plant medium for 7-8
659 plants per strain mixture.

660 After 45-60 days, plants were harvested. First, plant heights and the number of nodules per plant
661 were recorded. Then, the roots were cut from the stem and images of all nodules for each plant were
662 collected on a high-definition Keyence VHX-600 digital microscope at 20X magnification. These nodules
663 were then cross-sectioned and immediately transferred to Eppendorfs containing 4% paraformaldehyde
664 (Electron Microscopy Sciences) in PBS. Fresh sections were fixed overnight in the dark at 4°C, washed
665 5X in PBS, and stored in PBS supplemented with 0.1% azide in the dark at 4°C until imaging.

666 Fixed sections were stained in Calcofluor (all strain combinations), SYTO9 (WT-YFP and WT co-
667 inoculation only) or propidium iodide (mCherry-Δ*hpnH* and Δ*hpnH* co-inoculation only) as described for
668 Live:Dead staining. Imaging was performed as described for Live:Dead staining using a 5X objective.
669 Given the high autofluorescence of these nodules and low mCherry and YFP signal intensities, the
670 following excitation/emission settings were used: Calcofluor, 405 nm excitation/410-460 nm emission;
671 YFP/SYTO9, 488 nm excitation/500-550 nm emisasion; mCherry, 532 nm excitation/600-650 nm
672 emission.

673 Quantification of nodule statistics (including nodule and infection zone areas, signal intensity of
674 YFP, mCherry, SYTO9 and propidium iodide) was performed on raw images using a custom FIJI macro.
675 Briefly, nodule images were opened at random, infection zones (IZs) and whole nodules were circled by
676 hand and saved as discrete regions of interest (ROIs), and the area and intensity in each channel were
677 measured automatically for all ROIs. These measurements were exported as a text table and various

678 parameters from these measurements were calculated using custom Python scripts, as indicated in the
679 Results. Plots of all parameters and statistical comparisons were generated using custom R scripts.
680
681 *Antibiotic treatment of inoculated plants*
682 *A. afraspera* plants were cultivated as described above and the following antibiotics were added
683 to non-inoculated plants 7 days after rooting in 100 mL BNM growth tubes: kanamycin to 100 µg/mL,
684 streptomycin to 100 µg/mL, tetracycline to 20 µg/mL, kanamycin plus tetracycline, kanamycin plus
685 streptomycin, streptomycin plus tetracycline. Plants were grown in antibiotics under normal plant growth
686 conditions for 14 days, after which plants were visually inspected. Plant heights were also recorded, and
687 the root and shoot systems were separated with a razor blade, transferred into pre-weighed 15 mL Falcon
688 tubes, dried at 50°C for a minimum of 48 hours, then weighed again.
689 Antibiotic treatments of Δ*hpnH* and wild-type *B. diazoefficiens* were performed by growing
690 antibiotic 5 mL PSY cultures of each strain to stationary phase (OD_{600} >1.4) and diluting strains in fresh
691 PSY to reach an OD_{600} of ~0.8 at the time of antibiotic treatment – *e.g.* as they would be grown prior to
692 plant inoculation. Cultures were pelleted at 3250 x g for 30 minutes at RT, washed three times, then
693 resuspended in PSY to a final OD_{600} of 1.0. Four 100 µl aliquots of these culture were diluted 1:00 into
694 separate 10 mL BNM cultures in clear glass tubes in plant growth chambers. Kanamycin (at 25, 50, 75,
695 and 100 µg/mL) and streptomycin (at 25, 50, 75, and 100 µg/mL) were added directly to the BNM
696 cultures, and 100 µl samples were taken immediately prior to antibiotic treatment and at 2, 4, 6, 8, and 10
697 hours post-antibiotic addition. These 100 µl samples were immediately diluted 1:10 in 900 µl and mixed
698 vigorously by repeated pipetting. Vortexing was avoided as we found that this method reduces Δ*hpnH*
699 viability. Ten serial 1:10 dilutions were performed, and three 10 µl samples of each dilution for each strain
700 were spotted and dripped across PSY plates. After 7 days (wild type) or 10 days (Δ*hpnH*), colonies were
701 counted manually and recorded for each dilution exhibiting discrete colonies. Log plots of colony counts
702 over time were generated in R.
703 Plants were then inoculated with Δ*hpnH* and wild-type *B. diazoefficiens* as described above, and
704 kanamycin and streptomycin were added to Δ*hpnH*-inoculated plants to 50 µg/mL each, and to wild type-
705 inoculated plants to 100 µg/mL at 12 hours and 36 hours and at 2, 2.5, 3, 3.5, 4, 4.5, 5, 6.5, 8.5, 9.5, 10.5,

706 and 12.5 days post-inoculation. Four plants were treated per time point per strain, with an additional four
707 plants each as an untreated control. At 40 dpi, the number of nodules per plant was recorded.
708
709 *Bulk motility assays*
710 Swimming motility assays were performed as previously described, with some modifications
711 (Althabegoiti et al. 2008). WT and Δ*hpnH* were grown to turbidity in 5 mL of PSY at 30°C and 250 rpm,
712 diluted to an OD_{600} of 0.02 in 5 mL of fresh PSY, and grown to exponential phase (OD_{600} = 0.3-0.5).
713 Exponential cultures then were diluted to an OD_{600} of 0.06 in fresh PSY and 2 µL of the adjusted cultures
714 into the center of swimming plate containing 0.3% agar/PSY. After inoculation, the plates were wrapped
715 with parafilm to prevent dehydration and incubated in a humidity-controlled environmental chamber
716 (Percival) at 30°C for 10 days total, with daily scans after 5 days. The resulting images were analyzed in
717 FIJI to measure the area of the swimming colony.
718
719 *Surface attachment assays*
720 Δ*hpnH* and wild-type *B. diazoefficiens* were grown in 5 mL PSY cultures to stationary phase
721 (OD_{600} >1.4) then diluted in fresh PSY to reach an OD_{600} of ~0.8 at the time of surface attachment
722 assays. Cultures were pelleted at 3250 x g for 30 minutes at RT, washed twice in the indicated
723 attachment medium, then resuspended in attachment medium to an OD_{600} of 1.0. These cultures were
724 mixed thoroughly by repeated pipetting, and 2 mL samples were added to sterile imaging dishes (30 mm
725 dishes with 20 mm, #1.5 coverglass bottoms; MatTek). Cultures were incubated on imaging dishes
726 *without shaking* at 30°C for two hours. To remove non-adhered cells, imaging dishes were immersed in
727 50 mL of attachment media in a 100 mL glass beaker on an orbital shaker and shaken gently at RT for 5
728 minutes; direct application of washing medium to the coverglass surface was avoided, as we found that
729 this creates a shear force sufficient to wash away adhered cells. Imaging dishes were then gently lifted
730 out of the washing medium and imaged with a 100X objective on a Lumascope 720 fluorescence
731 microscope (Etaluma). Forty fields of view were recorded for each strain and media combination. These
732 images were processed in FIJI using the Enhanced Local Contrast (CLAHE) plugin[59] and converted
733 into a binary image to determine the area of the imaging window covered with adhered cells. Calculation

734 of the fraction of the surface was performed in Excel and statistical analyses were conducted in R. Areas
735 of the surface containing groups of cells larger than 10 μm^2 in area were ignored in the calculations, as
736 these likely do not represent true attachment events rather than sedimentation of larger cell clumps. BNM
737 used for attachment assays was prepared as described above, with the addition of 1.0 g/mL arabinose.
738 Because BNM contains salt crystals that can sediment onto coverglass and occlude or obscure adhered
739 cells, this medium was passed through a 2 µm filter (Millipore) prior to the attachment experiments.
740
741 *Single-cell motility assays and analysis*
742
743 B. diazoefficiens wild-type and ΔhpnH were grown in 12.5 ml PSY medium at 30°C and 200 rpm
744 to an OD_{600} = 0.6-0.8 from an AG medium plate culture. Then, a 1:10 dilution of cell culture was
745 subcultured in PSY medium to a final volume of 12.5 ml and regrown to an OD_{600} of ~0.6. Two aliquots of
746 750 µL were sampled from the regrowth culture and pelleted at 3500 x g for 20 min (wild-type) or for 30
747 min (ΔhpnH) at RT. The supernatant was removed, and one pellet was resuspended in 500 µL PSY and
748 the other in 500 µL BNM medium. Because BNM contains salt crystals that can sediment onto coverglass
749 and occlude or obscure adhered cells, this medium was passed through a 2 µm filter (Millipore) prior to
750 usage for these experiments. The two medium conditions were then incubated for 2.5 hrs (wild-type) or
751 for 3.5 hrs (ΔhpnH) at 30°C; given the difference in growth time ΔhpnH incubated for longer. Right before
752 imaging, each culture was diluted at a 1:10 ratio with its respective medium. The bacteria were then
753 injected into a sterile flow cell (ibidi sticky-Slide VI0.4 with a glass coverslip). The flow cell was attached to
754 a heating stage set to 30°C.
755 The imaging protocol involved high-speed bright-field imaging for 5 min at a single XYZ location
756 per experimental repeat. High speed bright-field recordings used a Phantom V12.1 high speed camera
757 (Vision Research); images were taken with a 5 ms exposure at 200 fps and a resolution of 512×512
758 pixels (0.1 µm/pixel). This protocol was performed on an Olympus IX83 microscope equipped with a 100×
759 oil objective, a 2× multiplier lens, and a Zero Drift Correction autofocus system. The recorded movies
760 were extracted into single frames from the .cine files using PCC 2.8 (Phantom Software). Image

processing and cell tracking algorithms are adapted from previous work[34] and written in MATLAB R2015a (Mathworks).

We identified cells swimming near the surface as cells with a trajectory radius of gyration greater than 2.5 μm and a mean-squared displacement (MSD) slope greater than 1.5. Setting a minimum radius of gyration selects for cells with a minimum net translation on the across the surface, while a minimum MSD slope threshold ensured the cells are moving super-diffusively (MSD slope ≅ 1, diffusive motion; MSD slope ≅ 2, super-diffusive motion). For each tracked cell, the mean-speed, $\mathbf{v}$, was calculated by averaging a moving window, $\mathbf{w}$, of the displacement over the cell's full trajectory, using the following equation:

$$< v > = \ Avg\left(\sum_{t=1}^{N-w} \frac{\sqrt{(x_{t+w} - x_t)^2 + (y_{t+w} - y_t)^2}}{w} * f * p\right)$$

where $\mathbf{N}$ is the total number of points in the trajectory, $\mathbf{f}$ is the acquisition frame rate, and $\mathbf{p}$ is the pixel resolution. Here we set a window size, w= 40 frames. All analysis and visualizations from these experiments where done using MATLAB R2015a (Mathworks).

Acknowledgements

This work was supported by grants from the HHMI (D.K.N.), NASA (NNX12AD93G, D.K.N.), Jane Coffin Childs Memorial Fund (B.J.B.), NIH (K99GM126141, B.J.B.), and Ford Foundation Predoctoral Fellowship (J.d.A.), and Army Research Office (W911NF-18-1-0254, GW). We thank Dr. Eric Giraud for his generous gift of *A. afraspera* seeds and training on *Aeschynomene* symbioses and Drs. Hans-Martin Fischer and Raphael Ledermann for plasmids and technical advice for the genetic transformation of *B. diazoefficiens*. Dr. Nathan Dalleska of the Environmental Analysis Center at Caltech was instrumental in providing training and support for GC-MS analysis of acetylene reduction. We are grateful to Dr. Gargi Kulkarni and other members of the Newman lab, as well as Drs. Elliot Meyerowitz and Rob Phillips, for their collegiality and thoughtful discussions

about this work. We are indebted to Ms. Shannon Park and Ms. Kristy Nguyen for providing the administrative assistance that allows us to focus on our research.

References

1. Belin BJ, Busset N, Giraud E, Molinaro A, Silipo A, Newman DK. Hopanoid lipids: from membranes to plant-bacteria interactions. Nat Rev Microbiol. England; 2018;16: 304–315. doi:10.1038/nrmicro.2017.173
2. Saenz JP, Grosser D, Bradley AS, Lagny TJ, Lavrynenko O, Broda M, et al. Hopanoids as functional analogues of cholesterol in bacterial membranes. Proc Natl Acad Sci U S A. United States; 2015;112: 11971–11976. doi:10.1073/pnas.1515607112
3. Wu C-H, Bialecka-Fornal M, Newman DK. Methylation at the C-2 position of hopanoids increases rigidity in native bacterial membranes. Elife. England; 2015;4. doi:10.7554/eLife.05663
4. Fantini J, Barrantes FJ. How cholesterol interacts with membrane proteins: an exploration of cholesterol-binding sites including CRAC, CARC, and tilted domains. Front Physiol. Frontiers; 2013;4: 31. doi:10.3389/fphys.2013.00031
5. Ochs D, Kaletta C, Entian K, Beck-sickinger A, Porallal K, Chemie O, et al. Cloning, Expression, and Sequencing of Squalene-Hopene Cyclase,. 1992;174: 298–302.
6. Syren P-O, Henche S, Eichler A, Nestl BM, Hauer B. Squalene-hopene cyclases-evolution, dynamics and catalytic scope. Curr Opin Struct Biol. England; 2016;41: 73–82. doi:10.1016/j.sbi.2016.05.019
7. Welander P V, Coleman ML, Sessions AL, Summons RE, Newman DK. Identification of a methylase required for 2-methylhopanoid production and implications for the interpretation of sedimentary hopanes. Proc Natl Acad Sci U S A. United States; 2010;107: 8537–8542. doi:10.1073/pnas.0912949107
8. Welander P V, Doughty DM, Wu C, Mehay S, Roger E. Identification and characterization of Rhodopseudomonas palustris TIE-1 hopanoid biosynthesis mutants. 2012;10: 163–177.
9. Schmerk CL, Welander P V, Hamad MA, Bain KL, Bernards MA, Summons RE, et al. Elucidation

814 of the Burkholderia cenocepacia hopanoid biosynthesis pathway uncovers functions for conserved
815 proteins in hopanoid-producing bacteria. Environ Microbiol. England; 2015;17: 735–750.
816 doi:10.1111/1462-2920.12509
817 10. Silipo A, Vitiello G, Gully D, Sturiale L, Chaintreuil C, Fardoux J, et al. Covalently linked hopanoid-
818 lipid A improves outer-membrane resistance of a Bradyrhizobium symbiont of legumes. Nat
819 Commun. England; 2014;5: 5106. doi:10.1038/ncomms6106
820 11. Kulkarni G, Busset N, Molinaro A, Gargani D, Chaintreuil C, Silipo A, et al. Specific hopanoid
821 classes differentially affect free-living and symbiotic states of Bradyrhizobium diazoefficiens.
822 MBio. United States; 2015;6: e01251-15. doi:10.1128/mBio.01251-15
823 12. Komaniecka I, Choma A, Mazur A, Duda KA, Lindner B, Schwudke D, et al. Occurrence of an
824 unusual hopanoid-containing lipid A among lipopolysaccharides from Bradyrhizobium species. J
825 Biol Chem. United States; 2014;289: 35644–35655. doi:10.1074/jbc.M114.614529
826 13. Ricci JN, Coleman ML, Welander P V., Sessions AL, Summons RE, Spear JR, et al. Diverse
827 capacity for 2-methylhopanoid production correlates with a specific ecological niche. ISME J.
828 Nature Publishing Group; 2014;8: 675–684. doi:10.1038/ismej.2013.191
829 14. Ourisson G, Albrecht P, Rohmer M. The Hopanoids: palaeochemistry and biochemistry of a group
830 of natural products. Pure Appl Chem. 1979;51: 709–729. doi:10.1351/pac197951040709
831 15. Racolta S, Juhl PB, Sirim D, Pleiss J. The triterpene cyclase protein family: a systematic analysis.
832 Proteins. United States; 2012;80: 2009–2019. doi:10.1002/prot.24089
833 16. Rodríguez-Navarro DN, Oliver IM, Contreras MA, Ruiz-Sainz JE. Soybean interactions with soil
834 microbes, agronomical and molecular aspects. doi:10.1051/agro/2010023
835 17. Vilcheze C, Llopiz P, Neunlist S, Poralla K, Rohmer M. Prokaryotic triterpenoids: New hopanoids
836 from the nitrogen-fixing bacteria Azotobacter vinelandii, Beijerinckia indica and Beijerinckia
837 mobilis. Microbiology. 1994;140: 2749–2753. doi:10.1099/00221287-140-10-2749
838 18. Parsons R, Silvester WB, Harris S, Gruijters WT, Bullivant S. Frankia vesicles provide inducible
839 and absolute oxygen protection for nitrogenase. Plant Physiol. United States; 1987;83: 728–731.
840 19. Abeysekera RM, Newcomb W, Silvester WB, Torrey JG. A freeze-fracture electron microscopic
841 study of *Frankia* in root nodules of *Alnus incana* grown at three oxygen tensions. Can J Microbiol.

842 NRC Research Press Ottawa, Canada ; 1990;36: 97–108. doi:10.1139/m90-019
843 20. Wheatley RM, Poole PS. Mechanisms of bacterial attachment to roots. FEMS Microbiol Rev.
844 England; 2018;42: 448–461. doi:10.1093/femsre/fuy014
845 21. Kanbe M, Yagasaki J, Zehner S, Göttfert M, Aizawa S-I. Characterization of two sets of subpolar
846 flagella in Bradyrhizobium japonicum. J Bacteriol. American Society for Microbiology Journals;
847 2007;189: 1083–9. doi:10.1128/JB.01405-06
848 22. Quelas JI, Althabegoiti MJ, Jimenez-Sanchez C, Melgarejo AA, Marconi VI, Mongiardini EJ, et al.
849 Swimming performance of Bradyrhizobium diazoefficiens is an emergent property of its two
850 flagellar systems OPEN. 2016; doi:10.1038/srep23841
851 23. Althabegoiti MJ, Covelli JM, Pérez-Giménez J, Quelas JI, Mongiardini EJ, López MF, et al.
852 Analysis of the role of the two flagella of Bradyrhizobium japonicum in competition for nodulation of
853 soybean. FEMS Microbiol Lett. 2011;319: 133–139. doi:10.1111/j.1574-6968.2011.02280.x
854 24. López-García SL, Perticari A, Piccinetti C, Ventimiglia L, Arias N, De Battista JJ, et al. In-Furrow
855 Inoculation and Selection for Higher Motility Enhances the Efficacy of Nodulation. Agron J.
856 American Society of Agronomy; 2009;101: 357. doi:10.2134/agronj2008.0155x
857 25. Bonaldi K, Gargani D, Prin Y, Fardoux J, Gully D, Nouwen N, et al. Nodulation of Aeschynomene
858 afraspera and A. indica by photosynthetic Bradyrhizobium Sp. strain ORS285: the nod-dependent
859 versus the nod-independent symbiotic interaction. Mol Plant Microbe Interact. United States;
860 2011;24: 1359–1371. doi:10.1094/MPMI-04-11-0093
861 26. Patriarca EJ, Tatè R, Ferraioli S, Iaccarino M. Organogenesis of Legume Root Nodules. Int Rev
862 Cytol. Academic Press; 2004;234: 201–262. doi:10.1016/S0074-7696(04)34005-2
863 27. Ledermann R, Bartsch I, Remus-Emsermann MN, Vorholt JA, Fischer H-M. Stable Fluorescent
864 and Enzymatic Tagging of Bradyrhizobium diazoefficiens to Analyze Host-Plant Infection and
865 Colonization. Mol Plant Microbe Interact. United States; 2015;28: 959–967. doi:10.1094/MPMI-03-
866 15-0054-TA
867 28. Pierre O, Engler G, Hopkins J, Brau F, Boncompagni E, Hérouart D. Peribacteroid space
868 acidification: A marker of mature bacteroid functioning in Medicago truncatula nodules. Plant, Cell
869 Environ. 2013;36: 2059–2070. doi:10.1111/pce.12116

870 29. Denison RF, Okano Y. Leghaemoglobin oxygenation gradients in alfalfa and yellow sweetclover
871 nodules. J Exp Bot. 2003;54: 1085–1091. doi:10.1093/jxb/erg097
872 30. Kereszt A, Mergaert P, Montiel J, Endre G, Kondorosi E. Impact of Plant Peptides on Symbiotic
873 Nodule Development and Functioning. Front Plant Sci. Switzerland; 2018;9: 1026.
874 doi:10.3389/fpls.2018.01026
875 31. Glazebrook J, Ichige A, Walker GC. A Rhizobium meliloti homolog of the Escherichia coli peptide-
876 antibiotic transport protein SbmA is essential for bacteroid development. Genes Dev. Cold Spring
877 Harbor Laboratory Press; 1993;7: 1485–97. doi:10.1101/GAD.7.8.1485
878 32. Szparaga A, Kocira S. Generalized logistic functions in modelling emergence of Brassica napus L.
879 PLoS One. 2018;13: 1–14. doi:10.1371/journal.pone.0201980
880 33. Richards FJ. NA Flexible Growth Function for Empirical Useo Title. J Exp Bot. 1959;10: 290–301.
881 doi:10.1093/jxb/10.2.290
882 34. Lee CK, de Anda J, Baker AE, Bennett RR, Luo Y, Lee EY, et al. Multigenerational memory and
883 adaptive adhesion in early bacterial biofilm communities. Proc Natl Acad Sci U S A. National
884 Academy of Sciences; 2018;115: 4471–4476. doi:10.1073/pnas.1720071115
885 35. Gupta R, Sharma M, Mittal A. Effects of membrane tension on nanopropeller driven bacterial
886 motion. J Nanosci Nanotechnol. 2006;6: 3854–3862. doi:10.1166/jnn.2006.630
887 36. Petrova OE, Sauer K. Sticky situations: Key components that control bacterial surface attachment.
888 J Bacteriol. 2012;194: 2413–2425. doi:10.1128/JB.00003-12
889 37. Persat A. Bacterial mechanotransduction. Curr Opin Microbiol. Elsevier Ltd; 2017;36: 1–6.
890 doi:10.1016/j.mib.2016.12.002
891 38. Mä J, Driessen R, Galajda P, Keymer JE, Dekker C. Bacterial growth and motility in sub-micron
892 constrictions [Internet]. 2009. Available: www.pnas.org/cgi/content/full/
893 39. Tuson HH, Auer GK, Renner LD, Hasebe M, Tropini C, Salick M, et al. Measuring the stiffness of
894 bacterial cells from growth rates in hydrogels of tunable elasticity. Mol Microbiol. Wiley/Blackwell
895 (10.1111); 2012;84: 874–891. doi:10.1111/j.1365-2958.2012.08063.x
896 40. Busset N, Di Lorenzo F, Palmigiano A, Sturiale L, Gressent F, Fardoux J, et al. The Very Long
897 Chain Fatty Acid (C26:25OH) Linked to the Lipid A Is Important for the Fitness of the

898 Photosynthetic Bradyrhizobium Strain ORS278 and the Establishment of a Successful Symbiosis
899 with Aeschynomene Legumes. Front Microbiol. Switzerland; 2017;8: 1821.
900 doi:10.3389/fmicb.2017.01821
901 41. Bradley AS, Swanson PK, Muller EEL, Bringel F, Caroll SM, Pearson A, et al. Hopanoid-free
902 Methylobacterium extorquens DM4 overproduces carotenoids and has widespread growth
903 impairment. PLoS One. United States; 2017;12: e0173323. doi:10.1371/journal.pone.0173323
904 42. Neubauer C, Dalleska NF, Cowley ES, Shikuma NJ, Wu C-H, Sessions AL, et al. Lipid remodeling
905 in Rhodopseudomonas palustris TIE-1 upon loss of hopanoids and hopanoid methylation.
906 Geobiology. England; 2015;13: 443–453. doi:10.1111/gbi.12143
907 43. Keymer A. Cross-kingdom lipid transfer in arbuscular mycorrhiza symbiosis and beyond. Curr
908 Opin Plant Biol. Elsevier Current Trends; 2018;44: 137–144. doi:10.1016/J.PBI.2018.04.005
909 44. Ferguson BJ, Mens C, Hastwell AH, Zhang M, Su H, Jones CH, et al. Legume nodulation: The
910 host controls the party. Plant Cell Environ. Wiley/Blackwell (10.1111); 2018;
911 doi:10.1111/pce.13348
912 45. Tsikou D, Yan Z, Holt DB, Abel NB, Reid DE, Madsen LH, et al. Systemic control of legume
913 susceptibility to rhizobial infection by a mobile microRNA. Science (80-). 2018;6907: eaat6907.
914 doi:10.1126/SCIENCE.AAT6907
915 46. Boiero L, Perrig D, Masciarelli O, Penna C, Cassán F, Luna V. Phytohormone production by three
916 strains of Bradyrhizobium japonicum and possible physiological and technological implications.
917 Appl Microbiol Biotechnol. 2007;74: 874–880. doi:10.1007/s00253-006-0731-9
918 47. Hammad Y, Nalin R, Marechal J, Fiasson K, Pepin R, Berry AM, et al. A possible role for phenyl
919 acetic acid (PAA) on Alnus glutinosa nodulation by Frankia. Plant Soil. Kluwer Academic
920 Publishers; 2003;254: 193–205. doi:10.1023/A:1024971417777
921 48. Podlešáková K, Fardoux J, Patrel D, Bonaldi K, Novák O, Strnad M, et al. Rhizobial Synthesized
922 Cytokinins Contribute to But Are Not Essential for the Symbiotic Interaction Between
923 Photosynthetic Bradyrhizobia and *Aeschynomene* Legumes. Mol Plant-Microbe Interact. The
924 American Phytopathological Society ; 2013;26: 1232–1238. doi:10.1094/MPMI-03-13-0076-R
925 49. Ledermann R, Bartsch I, Muller B, Wulser J, Fischer H-M. A Functional General Stress Response

of Bradyrhizobium diazoefficiens Is Required for Early Stages of Host Plant Infection. Mol Plant Microbe Interact. United States; 2018;31: 537–547. doi:10.1094/MPMI-11-17-0284-R

50. Burghardt LT, Epstein B, Guhlin J, Nelson MS, Taylor MR, Young ND, et al. Select and resequence reveals relative fitness of bacteria in symbiotic and free-living environments. Proc Natl Acad Sci U S A. National Academy of Sciences; 2018;115: 2425–2430. doi:10.1073/pnas.1714246115

51. Sugiyama A, Yazaki K. Root Exudates of Legume Plants and Their Involvement in Interactions with Soil Microbes. doi:10.1007/978-3-642-23047-9_2

52. Pini F, East AK, Appia-Ayme C, Tomek J, Karunakaran R, Mendoza-Suarez M, et al. Bacterial Biosensors for in Vivo Spatiotemporal Mapping of Root Secretion. Plant Physiol. United States; 2017;174: 1289–1306. doi:10.1104/pp.16.01302

53. FAO. Regional Overview of Food Security and Nutrition in Africa 2017. The food security and nutrition–conflict nexus: building resilience for food security, nutrition and peace [Internet]. 2017. Available: www.fao.org/publications

54. Delgado-Baquerizo M, Oliverio AM, Brewer TE, Benavent-Gonzalez A, Eldridge DJ, Bardgett RD, et al. A global atlas of the dominant bacteria found in soil. Science. United States; 2018;359: 320–325. doi:10.1126/science.aap9516

55. Regensburger B, Hennecke H. RNA polymerase from Rhizobium japonicum. Arch Microbiol. Springer-Verlag; 1983;135: 103–109. doi:10.1007/BF00408017

56. Ehrhardt DW, Atkinson EM, Long SR. Depolarization of alfalfa root hair membrane potential by Rhizobium meliloti Nod factors. Science. American Association for the Advancement of Science; 1992;256: 998–1000. doi:10.1126/SCIENCE.10744524

57. Schindelin J, Arganda-Carreras I, Frise E, Kaynig V, Longair M, Pietzsch T, et al. Fiji: An open-source platform for biological-image analysis [Internet]. Nature Methods. 2012. pp. 676–682. doi:10.1038/nmeth.2019

58. Schneider CA, Rasband WS, Eliceiri KW. NIH Image to ImageJ: 25 years of Image Analysis HHS Public Access [Internet]. Nat Methods. 2012. Available: https://www.ncbi.nlm.nih.gov/pmc/articles/PMC5554542/pdf/nihms876304.pdf

954 59. Heckbert PS, Karel. Graphics gems IV [Internet]. Graphics gems IV. AP Professional; 1994.
955 Available: https://dl.acm.org/citation.cfm?id=180940
956
957 **Figure Legends**
958
959 **Figure 1.** (**a**) Chemical structure of the extended hopanoid 2-Methyl Bacteriohopanetetrol (2Me-BHT),
960 consisting of a central pentacyclic core synthesized by the *shc* gene product, a C2 methylation site added
961 by the product of *hpnP* (grey shading, left), and a tetrol group added by the *hpnH* product (grey shading,
962 right). (**b**) Average shoot heights and nodules per plant at 24 dpi for *A. afraspera* plants inoculated with
963 wild-type, Δ*hpnH* or Δ*hpnP B. diazoefficiens.* (**c**) Average acetylene reduction per plant and per nodule at
964 24 dpi for *A. asfrapera* plants inoculated with wild-type, Δ*hpnH* or Δ*hpnP*. (**d**) Representative confocal
965 images of cross-sections of wild type- and Δ*hpnH*-infected nodules at 24 dpi illustrating plant cell walls
966 (Calcofluor, cyan), live bacteria (SYTO9, yellow) and membrane-compromised bacteria and plant nuclei
967 (propidium iodide, magenta). (**e**) Average nodule dry mass and acetylene reduction per nodule dry mass
968 at 24 dpi for plants inoculated with wild-type, Δ*hpnH* or Δ*hpnP*. Data shown in (**b**), (**c**) and (**e**) was
969 collected from n = 8 plants, with error bars representing one standard deviation. Results of two-tailed t-
970 tests between wild type and Δ*hpnH* or Δ*hpnP* are denoted as follows: n.s., $p>0.01$; *****, $p<0.01$; ******, $p<0.001$;
971 *******, $p<0.0001$.
972
973 **Figure 2.** (**a**) Average acetylene reduction per plant (n=4 plants per bar) and (**b**) average nodule dry
974 mass per plant (n=8 plants per bar) for *A. asfrapera* inoculated with wild-type or Δ*hpnH* over time. Error
975 bars representing one standard deviation. Results of two-tailed t-tests between wild type and Δ*hpnH* are
976 denoted as follows: n.s., $p>0.05$; *****, $p<0.05$; *******, $p<0.0001$. (**c-d**) *A. afraspera* inoculated with wild type or
977 Δ*hpnH* at (**c**) 20 dpi (left) and at (**d**) 40 dpi (right). (**e-f**) Distributions of nodule diameters at 40 dpi for *A.*
978 *afraspera* inoculated with (**e**) Δ*hpnH* (right; n=268 nodules pooled from 10 plants) or (**f**) wild type (left;
979 n=227 nodules pooled from 10 plants).
980

981 **Figure 3.** (**a**) Comparison of the development of selected wild type- and Δ*hpnH*-infected nodules over
982 time. (**b**) Nodule growth plots for 74 wild type-infected nodules tracked from 10 plants. (**c**) Nodule growth
983 plots for 84 Δ*hpnH*-infected nodules tracked from 16 plants. (**d**) Schematic of nodule development in *A.*
984 *afraspera*. From the left, bacteria (in blue) colonize and invade plant roots (green) and intracellularly infect
985 a root cell (pink); the time of this initial intracellular infection is considered $\mathbf{t_i}$ and the nodule volume can be
986 described as the volume of the single infected root cell, $\mathbf{V_i}$. This infected cell proliferates to form a
987 spherical nodule that is visible to the naked eye, at time $\mathbf{t_{min}}$ and volume $\mathbf{V_{min}}$. The infected plant cells
988 continue to proliferate at rate **dV/dt** until the nodule has fully matured at time $\mathbf{t_{max}}$ and volume $\mathbf{V_{max}}$. (**e**)
989 Fitted growth curve for a sample wild-type nodule illustrating the positions of $\mathbf{t_{min}}$, $\mathbf{V_{min}}$, **dV/dt**, $\mathbf{t_{max}}$, and
990 $\mathbf{V_{max}}$. (**f-g**) Jitter and box plots of (**f**) **dV/dt** and (**g**) $\mathbf{V_{max}}$ values for all wild type- and Δ*hpnH*-infected
991 nodules. Results of KS-tests between wild-type and Δ*hpnH* nodules are denoted as follows: ***, $p<10^{-6}$.
992 (**h**) Scatter plots of **dV/dt** vs. $\mathbf{V_{max}}$ values for wild-type and Δ*hpnH* nodules. Values of **dV/dt** and $\mathbf{V_{max}}$
993 below what is observed in the wild-type dataset are highlighted in green. (**i**) Distributions of $\mathbf{t_{min}}$ values (as
994 observed by eye) for nodules from wild type- (white bars) or Δ*hpnH*- (grey bars) infected plants. N=457
995 wild-type nodules across 20 plants and 479 Δ*hpnH* nodules across 20 plants.
996
997 **Figure 4.** (**a**) Confocal sections of small (<0.5 mm radius) Δ*hpnH*-infected nodules harvested at 40 dpi
998 and small (<0.5 mm radius) wild type-infected nodules harvested at 10 and 25 dpi. (**b**) Confocal sections
999 of larger (>0.5 mm radius) Δ*hpnH*- or wild type-infected nodules harvested at 40 dpi.
1000
1001 **Figure 5.** (**a**) Confocal sections of nodules from plants co-inoculated with wild type-YFP and Δ*hpnH*-
1002 mCherry harvested at 45-55 dpi. Sections were stained with Calcofluor (cyan) and are expressing YFP
1003 (yellow) and mCherry (magenta). (**b**) Scatter plot of median YFP intensity per pixel normalized by
1004 propidium iodide intensity per pixel (*e.g.* bacteroid density) within infection zones of nodules from plants
1005 co-inoculated with wild type-YFP and wild type, as a function of the percentage of wild type-YFP in the
1006 inoculum. (**c**) Scatter plot of median propidium iodide intensity per pixel (*e.g.* bacteroid density) within
1007 infection zones of nodules from plants co-inoculated with YFP-tagged wild type and untagged wild type,
1008 as a function of the percentage of WT-YFP in the inoculum. (**d**) Colony forming units/mL in wild type and

1009 Δ*hpnH* cultures grown in BNM supplemented with varying concentrations of kanamycin and
1010 spectinomycin at various times post-inoculation. (**e**) Average nodules per plant at 40 dpi for plants
1011 inoculated with either wild type or Δ*hpnH* and treated with 50 µg/mL (Δ*hpnH*) or 100 µg/mL (wild type)
1012 kanamycin and streptomycin at various time points post-inoculation. Nodule counts are normalized to
1013 those observed in non-antibiotic treated plants. (**f**) Images of inoculated plants at 40 dpi after antibiotic
1014 treatment at various time points. Untreated plants are shown on the left, with increasing time of antibiotic
1015 addition. Error bars represent one standard deviation.
1016
1017 **Figure 6.** (**a**) Sample time course of wild type and Δ*hpnH* colony expansion on low-agar PSY plates (dpi
1018 = days post-inoculation). Scale bars represent 2 cm. (**b**) Average colony sizes of wild type and Δ*hpnH*
1019 over time. N=4 plates per strain; error bars indicate one standard deviation. (**c**) Trajectories of individual
1020 wild type (top) and Δ*hpnH* (bottom) cells over a 5 minute time course in PSY. (**d**) Distributions of mean-
1021 speed s for motile wild type (N=359) and Δ*hpnH* (N=91) cells for trajectories in **d**. Dotted lines indicate the
1022 means of the distributions. (**e**) Trajectories of individual wild type (top) and Δ*hpnH* (bottom) cells over a 5
1023 minute time course in BNM. (**f**) Distributions of mean-speeds for motile WT (N=421) and Δ*hpnH* (N=141)
1024 cells in BNM for trajectories in **e**. Dotted lines indicate the means of the distributions. (g) Jitter and box
1025 plots of surface attachment (*e.g.* the percent of the field of view covered with cells) of WT and Δ*hpnH*
1026 after 2 hours of incubation on glass in PSY or BNM. N=40 fields of view per condition. Results of two-
1027 tailed t-tests between wild type and Δ*hpnH* are denoted as follows: n.s., $p>0.05$; ***, $p<0.00001$.
1028
1029 **Figure 7.** Schematic representation of *A. afraspera* wild-type root nodule development (top row; white
1030 background) and defects in development associated with extended hopanoid loss (bottom row; grey
1031 background). Early in development, fewer Δ*hpnH* cells are motile (**a**) and competent to attach to root
1032 surfaces (**b**), leading to a delay in establishment of stable root colonies. At later stages, slow growth of
1033 Δ*hpnH* into the root interior, or poor uptake by and division within host cells (**c**) may generate “patchy”, or
1034 under-populated infection zone that is propagated as the nodule grows (**d**). Alternately, fully-infected
1035 Δ*hpnH* nodules may lose symbionts to symbiont cell death (**e**) via poor bacteroid survival or plant-directed
1036 symbiosome degradation.

1037

1038 **Supplemental Figures**

1039

1040 **Figure S1.** Confocal images of cross-sections of wild type-infected *A. afraspera* nodules at 24 dpi
1041 illustrating plant cell walls (Calcofluor, cyan), live bacteria (SYTO9, yellow) and membrane-compromised
1042 bacteria and plant nuclei (propidium iodide, magenta). Nodules were collected from 3 plants.

1043

1044 **Figure S2**. Confocal images of cross-sections of Δ*hpnH*-infected *A. afraspera* nodules at 24 dpi
1045 illustrating plant cell walls (Calcofluor, cyan), live bacteria (SYTO9, yellow) and dead bacteria and plant
1046 nuclei (propidium iodide, magenta). Nodules were collected from 3 plants. White boxes highlight small
1047 nodules. White arrow indicates a likely plant defense reaction.

1048

1049 **Figure S3**. Average (**a**) shoot height, (**b**) nodules per plant, (**c**) nodule dry weight per plant, (**d**) acetylene
1050 reduction per plant, (**e**) acetylene reduction per nodule, and (**f**) acetylene reduction per nodule dry weight
1051 for *A. asfrapera* inoculated with wild-type or Δ*hpnH* at 40 dpi. N=4 plants per bar; error bars represent one
1052 standard deviation. Results of two-tailed t-tests between wild type and Δ*hpnH* are denoted as follows:
1053 n.s., $p>0.05$.

1054

1055 **Figure S4.** Reconstructed images of the root system of a wild type-infected *A. afraspera* plant. Nodules
1056 fully visible in at least five time points are indicated with black arrowheads.

1057

1058 **Figure S5.** Reconstructed images of the root system of a Δ*hpnH*-infected *A. afraspera* plant. Nodules
1059 fully visible in at least five time points are indicated with black arrowheads.

1060

1061 **Figure S6.** Nodule growth plots for all 74 wild type-infected nodules fit with quadratic (orange; long
1062 dashed lines), exponential (yellow; short dashed lines), or sigmoidal (blue; solid lines) models. Standard
1063 errors (SE) for each model are shown.

1064

1065 **Figure S7.** Nodule growth plots for all 84 Δ*hpnH*-infected nodules fit with quadratic (orange; long dashed
1066 lines), exponential (yellow; short dashed lines), or sigmoidal (blue; solid lines) models. Standard errors
1067 (SE) for each model are shown.
1068
1069 **Figure S8.** (**a**) Jitter and box plots of $\mathbf{t_{max}}$ values for all wild type- and Δ*hpnH*-infected nodules. (**b**) Jitter
1070 and box plots of maximum growth windows for all wild type- and Δ*hpnH*-infected nodules. (**c**) Jitter and
1071 box plots of $\mathbf{t_{min}}$ values (as determined by extrapolation using sigmoidal fits of nodule growth curves) for
1072 all wild type- and Δ*hpnH*-infected nodules, in which $\mathbf{V_{min}}$ is defined as 0.05 mm^3, 0.1 mm^3, 0.2 mm^3.
1073 Green shading highlights negative $\mathbf{t_{min}}$ values. Results of KS-tests between wild-type and Δ*hpnH* nodules
1074 are denoted as follows: *, $p<0.05$; n.s., $p>0.05$.
1075
1076 **Figure S9.** (**a-b**) Scatter plots of $\mathbf{t_{max}}$ vs. (**a**) **dV/dt** and (**b**) $\mathbf{V_{max}}$ for all wild type- (open circles) and
1077 Δ*hpnH*- (grey circles) infected nodules. Green regions highlight values below what is observed for wild
1078 type. (**c-d**) Scatter plots of maximum growth windows vs. (**c**) **dV/dt** and (**d**) $\mathbf{V_{max}}$. (**e-f**) Scatter plots of $\mathbf{t_{min}}$
1079 vs. (**c**) **dV/dt** and (**d**) $\mathbf{V_{max}}$. (**g-h**) Scatter plots of $\mathbf{t_{min}}$ vs. (**a**) $\mathbf{t_{max}}$ and (**b**) maximum growth windows.
1080
1081 **Figure S10**. Confocal sections of small (<0.5 mm radius) Δ*hpnH*-infected nodules harvested at 40 dpi.
1082 Sections were stained with Calcofluor (cyan), SYTO9 (yellow), and propidium iodide (magenta). N=74
1083 nodules harvested from 5 plants. White boxes highlight under-infected nodules. Magenta boxes indicate
1084 nodules primarily containing membrane-compromised cells.
1085
1086 **Figure S11**. Confocal sections of large (>0.5 mm radius) Δ*hpnH*-infected nodules harvested at 40 dpi.
1087 Sections were stained with Calcofluor (cyan), SYTO9 (yellow), and propidium iodide (magenta). N=87
1088 nodules harvested from 5 plants. White boxes highlight under-infected nodules.
1089
1090 **Figure S12**. Confocal sections of small (<0.5 mm radius) wild type-infected nodules harvested at 10 dpi.
1091 Sections were stained with Calcofluor (cyan), SYTO9 (yellow), and propidium iodide (magenta). N=80
1092 nodules harvested from 5 plants. White boxes highlight under-infected nodules.

1093

1094 **Figure S13**. Confocal sections of small (<0.5 mm radius) wild type-infected nodules harvested at 25 dpi.
1095 Sections were stained with Calcofluor (cyan), SYTO9 (yellow), and propidium iodide (magenta). N=82
1096 nodules harvested from 5 plants. Magenta boxes indicate nodules primarily containing membrane-
1097 compromised cells.

1098

1099 **Figure S14**. Confocal sections of wild type-infected nodules harvested at 40 dpi. Sections were stained
1100 with Calcofluor (cyan), SYTO9 (yellow), and propidium iodide (magenta). N=117 nodules harvested from
1101 5 plants. Magenta boxes indicate nodules primarily containing membrane-compromised cells.

1102

1103 **Figure S15**. Confocal sections of nodules from plants co-inoculated with 10% WT-YFP:90% Δ*hpnH*-
1104 mCherry. Nodules were harvested between 45 and 50 dpi. Sections were stained with Calcofluor (cyan)
1105 and express YFP (yellow) mCherry (magenta). N=132 nodules harvested from 8 plants.

1106

1107 **Figure S16**. Confocal sections of nodules from plants co-inoculated with 25% WT-YFP:75% Δ*hpnH*-
1108 mCherry. Nodules were harvested between 45 and 50 dpi. Sections were stained with Calcofluor (cyan)
1109 and express YFP (yellow) mCherry (magenta). N=125 nodules harvested from 7 plants.

1110

1111 **Figure S17**. Confocal sections of nodules from plants co-inoculated with 50% WT-YFP:50% Δ*hpnH*-
1112 mCherry. Nodules were harvested between 45 and 50 dpi. Sections were stained with Calcofluor (cyan)
1113 and express YFP (yellow) mCherry (magenta). N=143 nodules harvested from 7 plants.

1114

1115 **Figure S18**. Confocal sections of nodules from plants co-inoculated with 75% WT-YFP:25% Δ*hpnH*-
1116 mCherry. Nodules were harvested between 45 and 50 dpi. Sections were stained with Calcofluor (cyan)
1117 and express YFP (yellow) mCherry (magenta). N=143 nodules harvested from 8 plants.

1118

1119 **Figure S19**. Confocal sections of nodules from plants co-inoculated with 90% WT-YFP:10% Δ*hpnH*-
1120 mCherry. Nodules were harvested between 45 and 50 dpi. Sections were stained with Calcofluor (cyan)
1121 and express YFP (yellow) mCherry (magenta). N=110 nodules harvested from 7 plants.
1122
1123 **Figure S20**. Average shoot height (**a**) and number of nodules (**b**) for plants co-inoculated with Δ*hpnH*-
1124 mCherry and WT-YFP strains, recorded at 45 dpi. Average shoot height (**c**) and number of nodules (**d**) for
1125 plants co-inoculated with WT and WT-YFP strains, recorded at 40 dpi. Average shoot height (**e**) and
1126 number of nodules (**f**) for plants co-inoculated with Δ*hpnH* and Δ*hpnH*-mCherry strains, recorded at 50
1127 dpi. N=7-8 plants per bar for all panels. Error bars represent one standard deviation. Results of two-tailed
1128 t-tests are denoted as follows: n.s., $p>0.05$; ***, $p<0.0001$.
1129
1130 **Figure S21**. (**a**-**d**) Intensity ratio of YFP to mCherry (**a**), mCherry intensity (**b**), and YFP intensity (**c**) per
1131 pixel within infection zones of nodules co-inoculated with Δ*hpnH*-mCherry and WT-YFP strains. (**d**)
1132 Cross-sectional area of infection zones of nodules co-inoculated with Δ*hpnH*-mCherry and WT-YFP
1133 strains. For (**a**-**d**), N=132, 125, 143, 143 and 110 nodules for 10%, 25%, 50%, 75% and 90% WT-YFP
1134 strain mixtures, respectively, which were sectioned and fixed between 45-50 dpi. (**e**) Nodule volume
1135 distributions from plants co-inoculated with Δ*hpnH*-mCherry and WT-YFP strains at 45 dpi. Sample sizes
1136 are N = 251, 200, 227, 204, and 149 nodules pooled from N = 8, 7, 7, 8, and 7 plants for the 10%, 25%,
1137 50%, 75% and 90% WT-YFP strain mixtures, respectively. (**f**) Scatter plots of mCherry vs. YFP intensities
1138 per pixel within infection zones of nodules co-inoculated with Δ*hpnH*-mCherry and WT-YFP strains. (**g**-**h**)
1139 Scatter plots of YFP/mCherry intensity ratios per pixel in infection zones vs. infection zone (**g**) and nodule
1140 (**h**) cross-section areas for nodules co-inoculated with Δ*hpnH*-mCherry and WT-YFP strains. Scatter plots
1141 contain data pooled from all ratios.
1142
1143 **Figure S22**. (**a**-**d**) Intensity ratio of YFP to propidium iodide (PI) (**a**), PI intensity (**b**), and YFP intensity (**c**)
1144 per pixel within infection zones of nodules co-inoculated with WT and WT-YFP strains. (**d**) Cross-
1145 sectional area of infection zones of nodules co-inoculated with WT and WT-YFP strains. For (**a**-**d**), N =
1146 141, 95, 134, 147, 133, and 167 nodules for 10%, 25%, 50%, 75%, 90% and 100% WT-YFP strain

1147 mixtures, respectively, which were sectioned and fixed between 40-45 dpi. (**e**) Nodule volume
1148 distributions from plants co-inoculated with WT and WT-YFP strains at 40 dpi. Sample sizes are N = 183,
1149 116, 161, 172, 232, and 248 nodules pooled from N = 8, 7, 8, 8, 8, and 8 plants for the 10%, 25%, 50%,
1150 75% and 90% WT-YFP strain mixtures, respectively. (**f**) Scatter plots of PI vs. YFP intensities per pixel
1151 within infection zones of nodules co-inoculated with WT and WT-YFP strains. (**g**-**h**) Scatter plots of
1152 YFP/PI intensity ratios per pixel in infection zones vs. infection zone (**g**) and nodule (**h**) cross-section
1153 areas for nodules co-inoculated with WT and WT-YFP strains. Scatter plots contain data pooled from all
1154 ratios.
1155
1156 **Figure S23**. (**a**-**d**) Intensity ratio of mCherry to SYTO9 (**a**), SYTO9 intensity (**b**), and mCherry intensity (**c**)
1157 per pixel within infection zones of nodules co-inoculated with Δ*hpnH*-mCherry and Δ*hpnH* strains. (**d**)
1158 Cross-sectional area of infection zones of nodules co-inoculated with Δ*hpnH*-mCherry and Δ*hpnH* strains.
1159 For (**a**-**d**), N = 117, 107, 128, 137, 103 and 50 nodules for 10%, 25%, 50%, 75%, 90% and 100% Δ*hpnH*-
1160 mCherry strain mixtures, respectively, which were sectioned and fixed between 50-55 dpi. (**e**) Nodule
1161 volume distributions from plants co-inoculated with Δ*hpnH*-mCherry and Δ*hpnH* strains at 45 dpi. Sample
1162 sizes are N = 150, 222, 191, 254, 297, and 236 nodules pooled from N = 7, 7, 7, 8, 8, and 8 plants for the
1163 10%, 25%, 50%, 75% and 90% WT-YFP strain mixtures, respectively. (**f**) Scatter plots of mCherry vs.
1164 SYTO9 intensities per pixel within infection zones of nodules co-inoculated with Δ*hpnH*-mCherry and
1165 Δ*hpnH* strains. (**g**-**h**) Scatter plots of mCherry/SYTO9 intensity ratios per pixel in infection zones vs.
1166 infection zone (**g**) and nodule (**h**) cross-section areas for nodules co-inoculated with Δ*hpnH*-mCherry and
1167 Δ*hpnH* strains. Scatter plots contain data pooled from all strain ratios.
1168
1169 **Figure S24**. Average (**a**) shoot height, (**b**) shoot dry mass and (**c**) root dry mass for non-inoculated *A.*
1170 *afraspera* plants grown in BNM supplemented with kanamycin, streptomycin or tetracycline for 2 weeks
1171 under normal growth conditions. N=4 plants per condition; error bars represent one standard deviation.
1172 (**d-e**) Images of *A. afraspera* plants after 2 weeks of antibiotic treatment. Asterisks indicate plants grown
1173 in tetracycline-supplemented medium.
1174

1175 **Figure S25**. Surface attachment of wild type (**a,c**) and Δ*hpnH* (**b,d**) incubated on glass coverslips in

1176 various media. For each panel, raw phase images (top row), background-subtracted images (middle row),

1177 and binary images with cells shown in black (bottom row) are shown. Scale bars represent 20 μm.

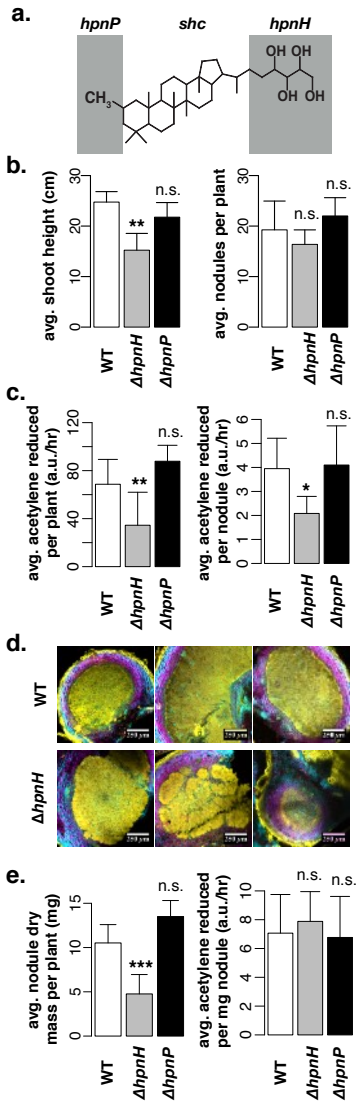
a.
hpnP
shc
hpnH
CH3
OH OH
OH OH
b.
avg. shoot height (cm)
avg. nodules per plant
n.s.
**
n.s.
WT
ΔhpnH
ΔhpnP
c.
avg. acetylene reduced per plant (a.u./hr)
avg. acetylene reduced per nodule (a.u./hr)
**
*
n.s.
d.
WT
ΔhpnH
e.
avg. nodule dry mass per plant (mg)
avg. acetylene reduced per mg nodule (a.u./hr)
***
n.s.

Figure 1.

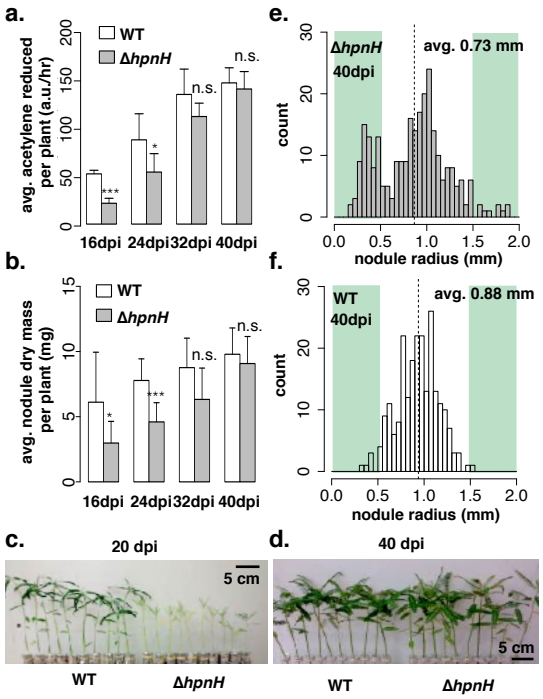
a.
WT
ΔhpnH
avg. acetylene reduced per plant (a.u./hr)
0
50
100
150
200
***
*
n.s.
n.s.
16dpi
24dpi
32dpi
40dpi
b.
WT
ΔhpnH
avg. nodule dry mass per plant (mg)
0
5
10
15
*
***
n.s.
n.s.
16dpi
24dpi
32dpi
40dpi
c.
20 dpi
5 cm
WT
ΔhpnH
d.
40 dpi
5 cm
WT
ΔhpnH
e.
ΔhpnH
40dpi
avg. 0.73 mm
count
0
10
20
30
0.0
0.5
1.0
1.5
2.0
nodule radius (mm)
f.
WT
40dpi
avg. 0.88 mm
count
0
10
20
30
0.0
0.5
1.0
1.5
2.0
nodule radius (mm)

Figure 2.

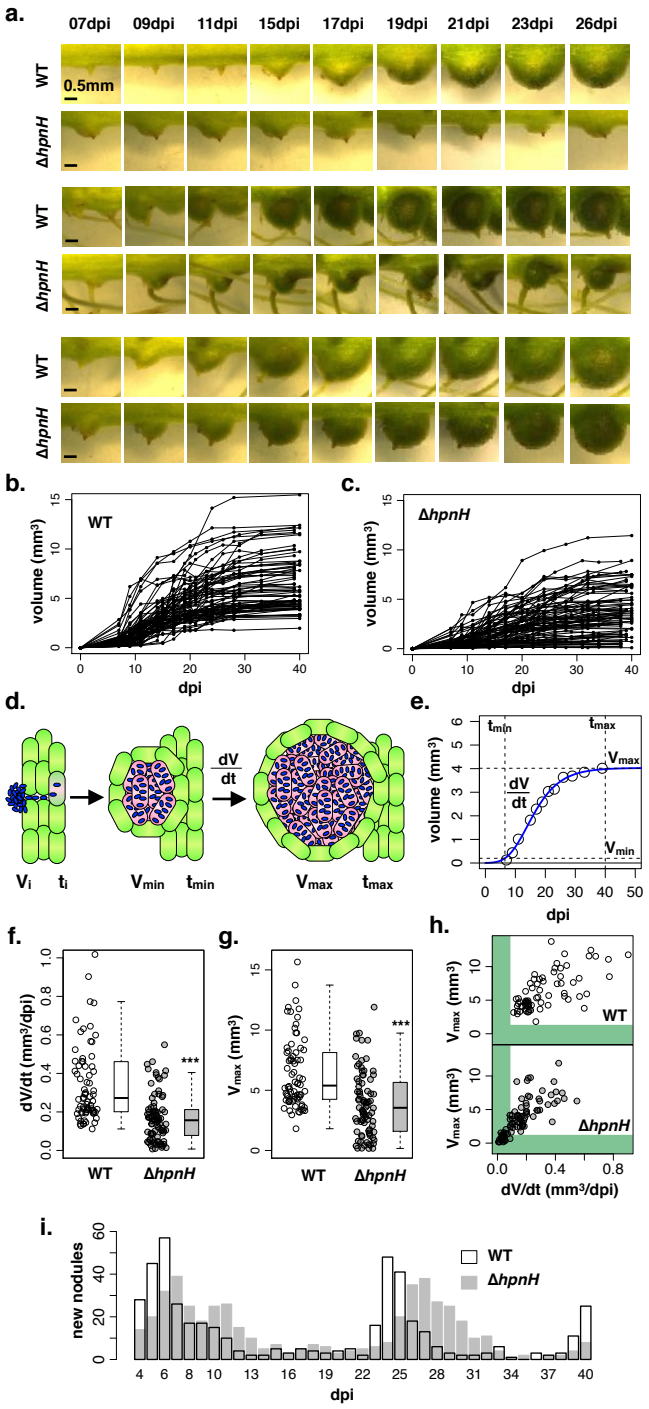
a.
07dpi
09dpi
11dpi
15dpi
17dpi
19dpi
21dpi
23dpi
26dpi
WT
ΔhpnH
0.5mm
b.
WT
volume (mm³)
dpi
c.
ΔhpnH
volume (mm³)
dpi
d.
dV
dt
Vi
ti
Vmin
tmin
Vmax
tmax
e.
tmin
tmax
Vmax
Vmin
dV
dt
volume (mm³)
dpi
f.
dV/dt (mm³/dpi)
***
WT
ΔhpnH
g.
Vmax (mm³)
***
WT
ΔhpnH
h.
Vmax (mm³)
WT
ΔhpnH
dV/dt (mm³/dpi)
i.
new nodules
WT
ΔhpnH
dpi

Figure 3.

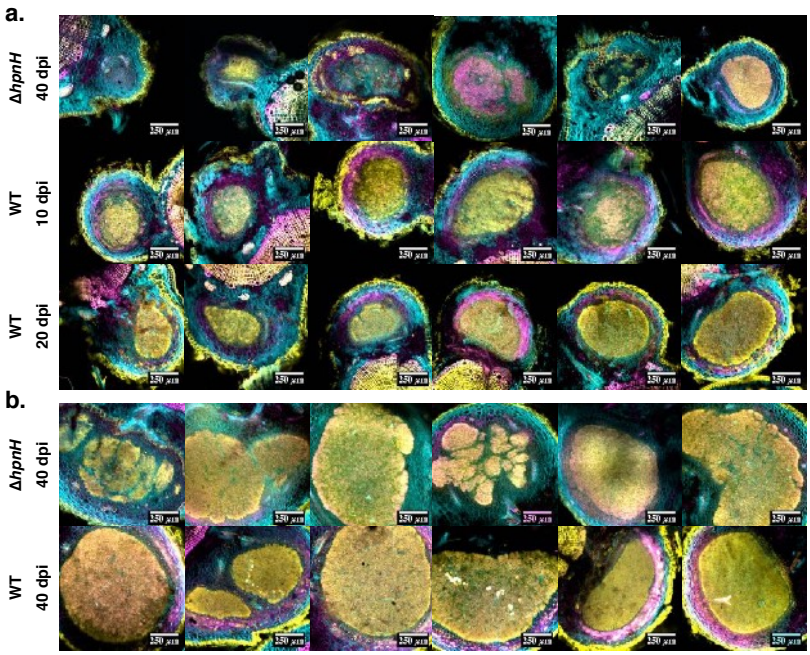

Figure 4.

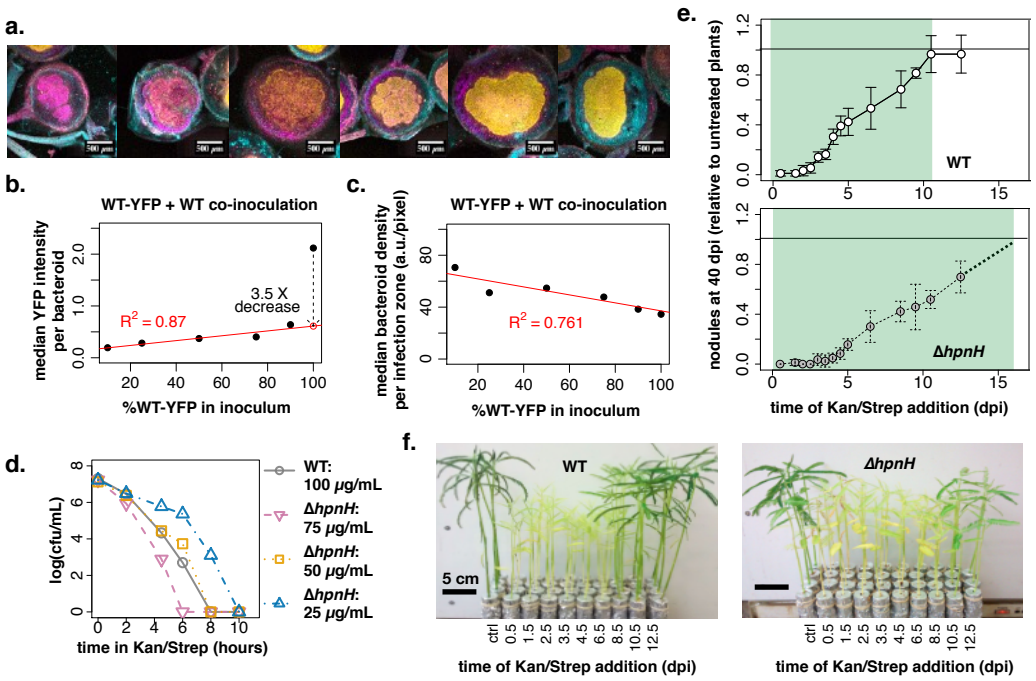
a.
b.
WT-YFP + WT co-inoculation
median YFP intensity per bacteroid
3.5 X decrease
R^2 = 0.87
%WT-YFP in inoculum
c.
WT-YFP + WT co-inoculation
median bacteroid density per infection zone (a.u./pixel)
R^2 = 0.761
%WT-YFP in inoculum
e.
nodules at 40 dpi (relative to untreated plants)
WT
ΔhpnH
time of Kan/Strep addition (dpi)

d.
log(cfu/mL)
time in Kan/Strep (hours)
WT: 100 μg/mL
ΔhpnH: 75 μg/mL
ΔhpnH: 50 μg/mL
ΔhpnH: 25 μg/mL
f.
WT
ΔhpnH
5 cm
ctrl 0.5 1.5 2.5 3.5 4.5 6.5 8.5 10.5 12.5
time of Kan/Strep addition (dpi)

Figure 5.

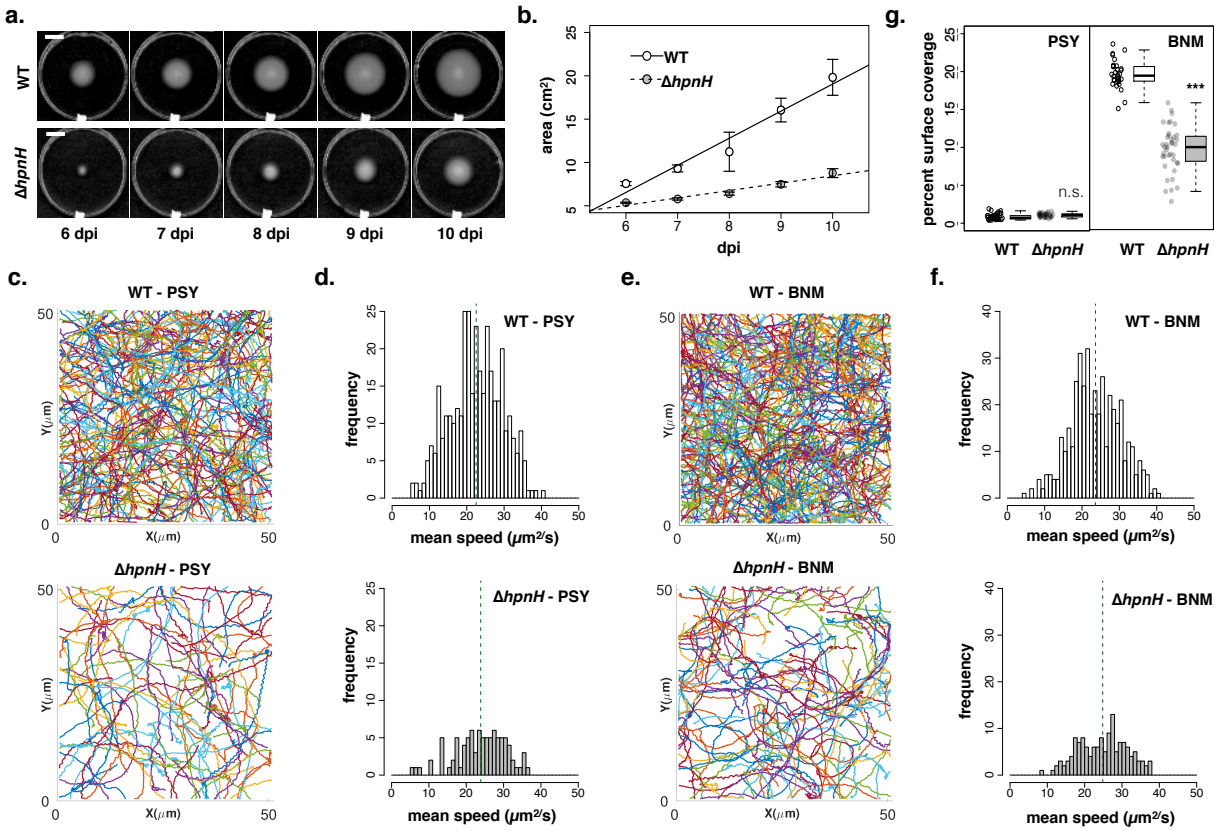
a.
WT
ΔhpnH
6 dpi
7 dpi
8 dpi
9 dpi
10 dpi
b.
WT
ΔhpnH
area (cm²)
dpi
g.
PSY
BNM
percent surface coverage
n.s.
***
WT
ΔhpnH
WT
ΔhpnH
c.
WT - PSY
ΔhpnH - PSY
Y(μm)
X(μm)
d.
WT - PSY
ΔhpnH - PSY
frequency
mean speed (μm²/s)
e.
WT - BNM
ΔhpnH - BNM
Y(μm)
X(μm)
f.
WT - BNM
ΔhpnH - BNM
frequency
mean speed (μm²/s)

Figure 6.

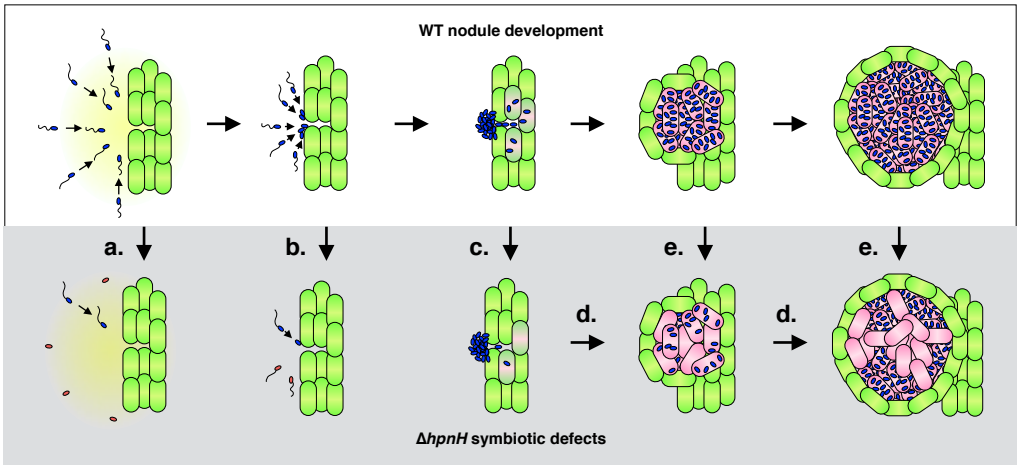

Figure 7.

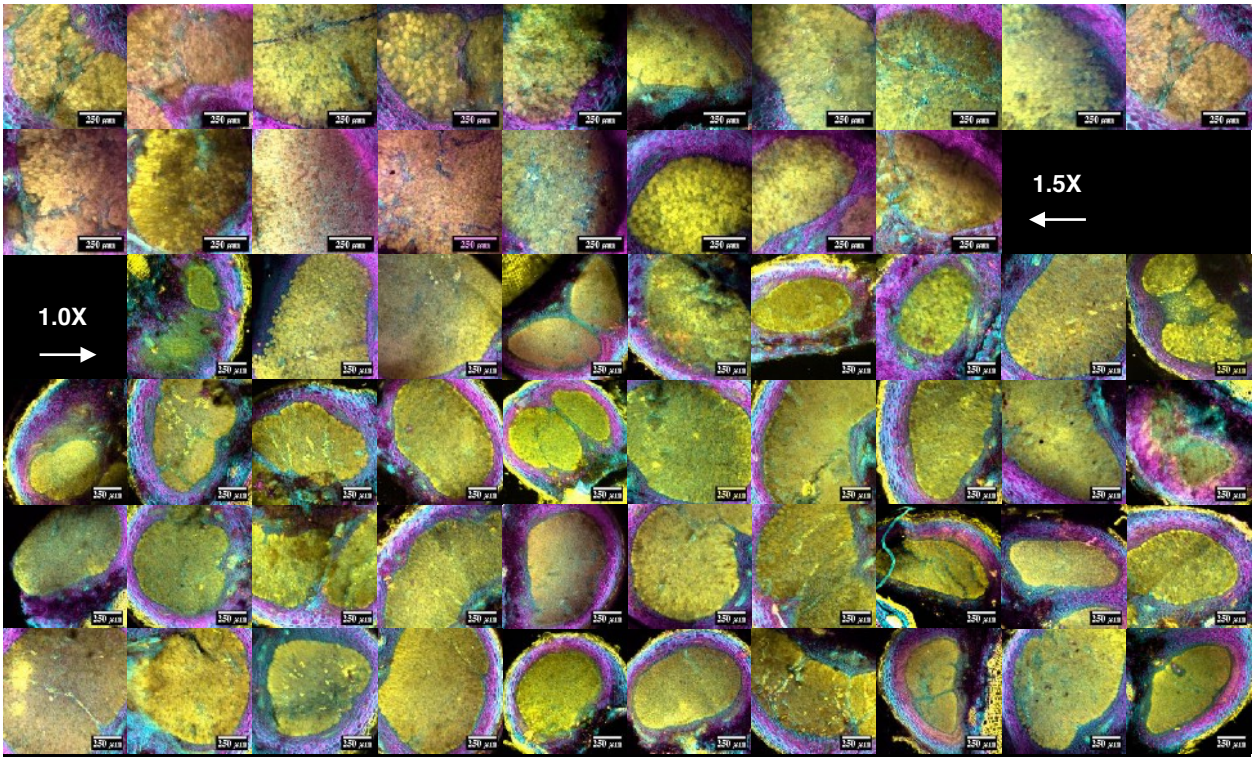

Figure S1.

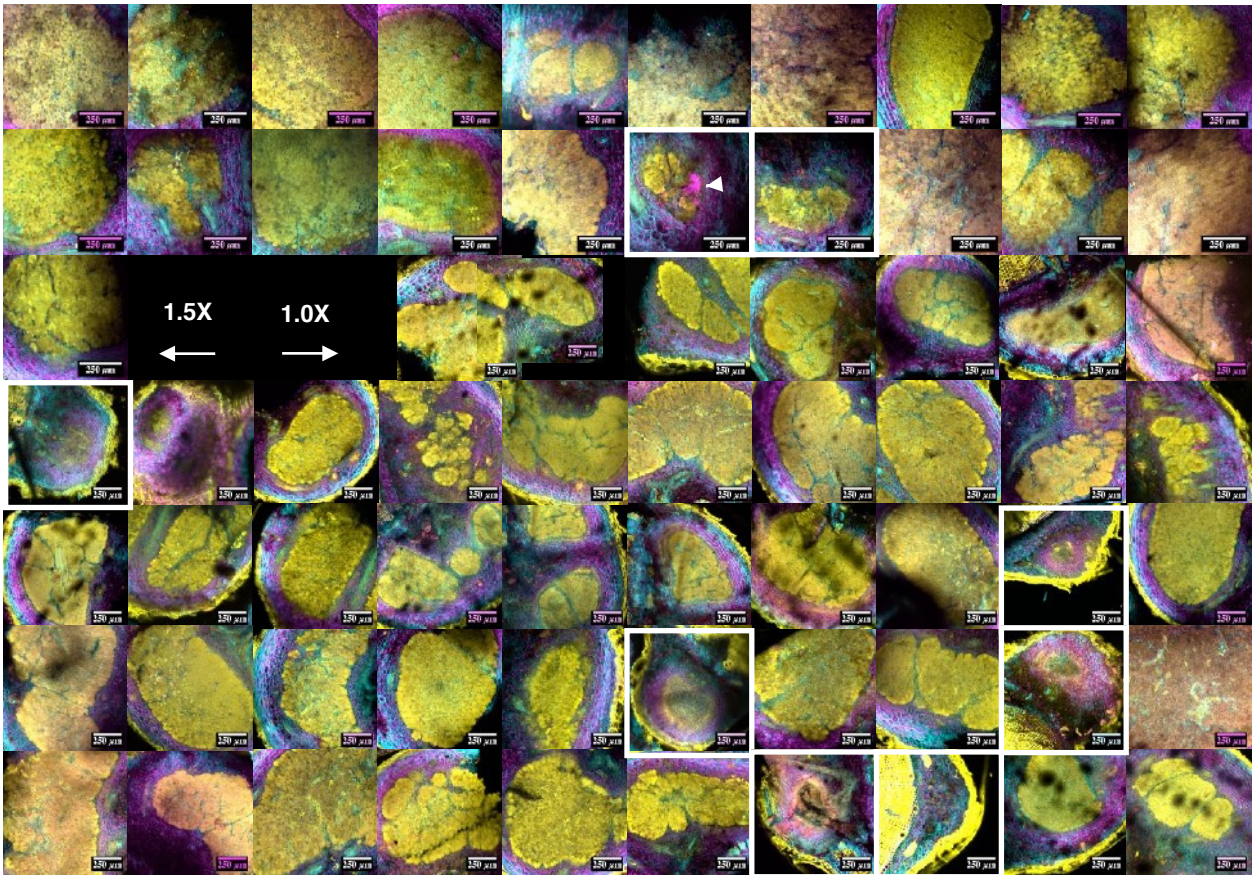

Figure S2.

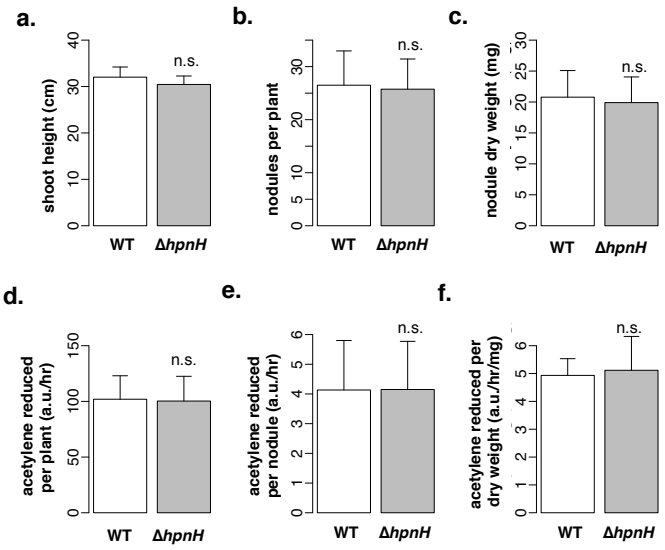
a.
shoot height (cm)
0
10
20
30
40
n.s.
WT
ΔhpnH
b.
nodules per plant
0
5
10
20
30
n.s.
WT
ΔhpnH
c.
nodule dry weight (mg)
0
5
10
15
20
25
30
n.s.
WT
ΔhpnH
d.
acetylene reduced per plant (a.u./hr)
0
50
100
150
n.s.
WT
ΔhpnH
e.
acetylene reduced per nodule (a.u./hr)
0
1
2
3
4
5
6
n.s.
WT
ΔhpnH
f.
acetylene reduced per dry weight (a.u./hr/mg)
0
1
2
3
4
5
6
n.s.
WT
ΔhpnH

Figure S3.

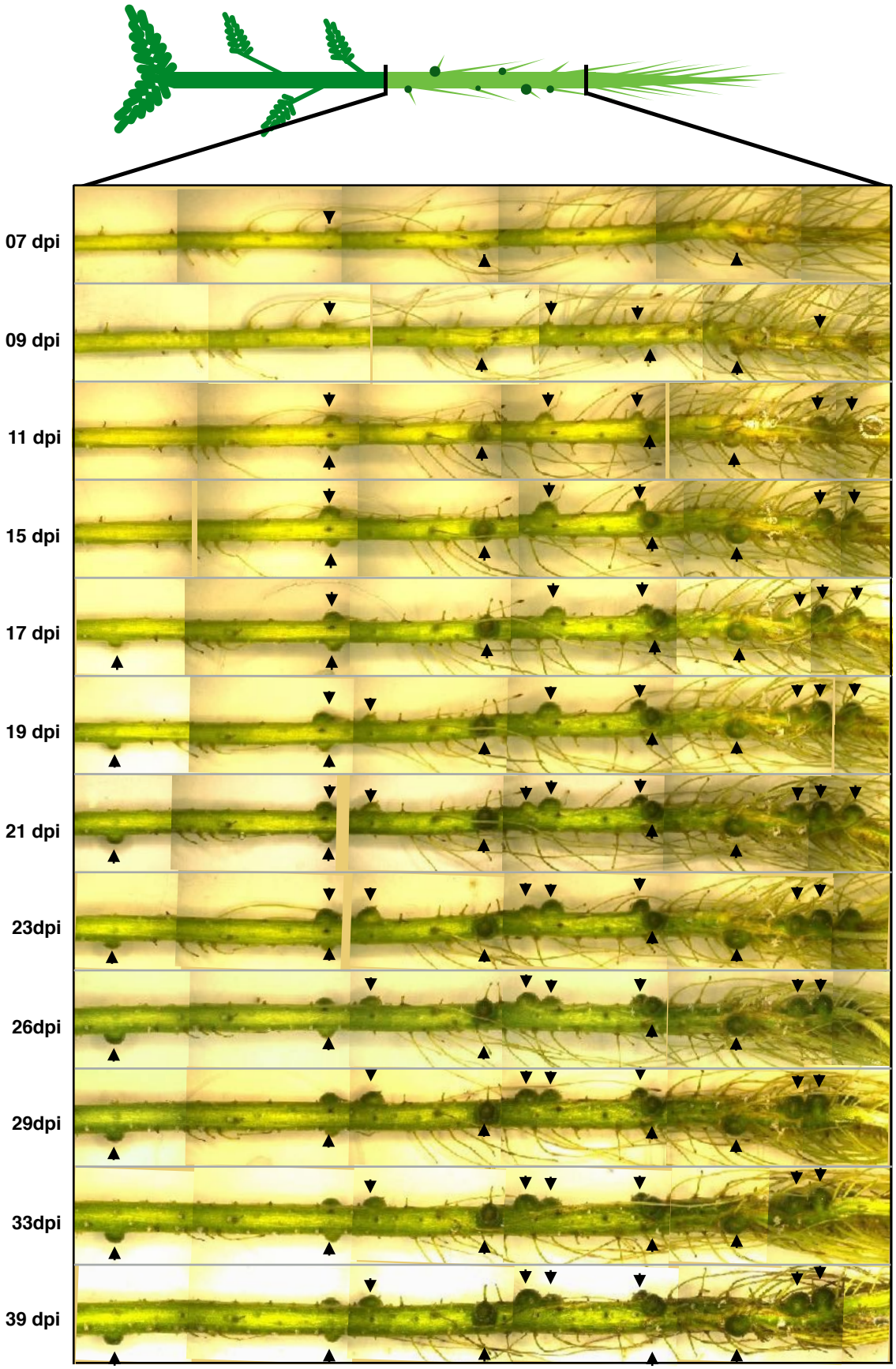
07 dpi
09 dpi
11 dpi
15 dpi
17 dpi
19 dpi
21 dpi
23dpi
26dpi
29dpi
33dpi
39 dpi

Figure S4.

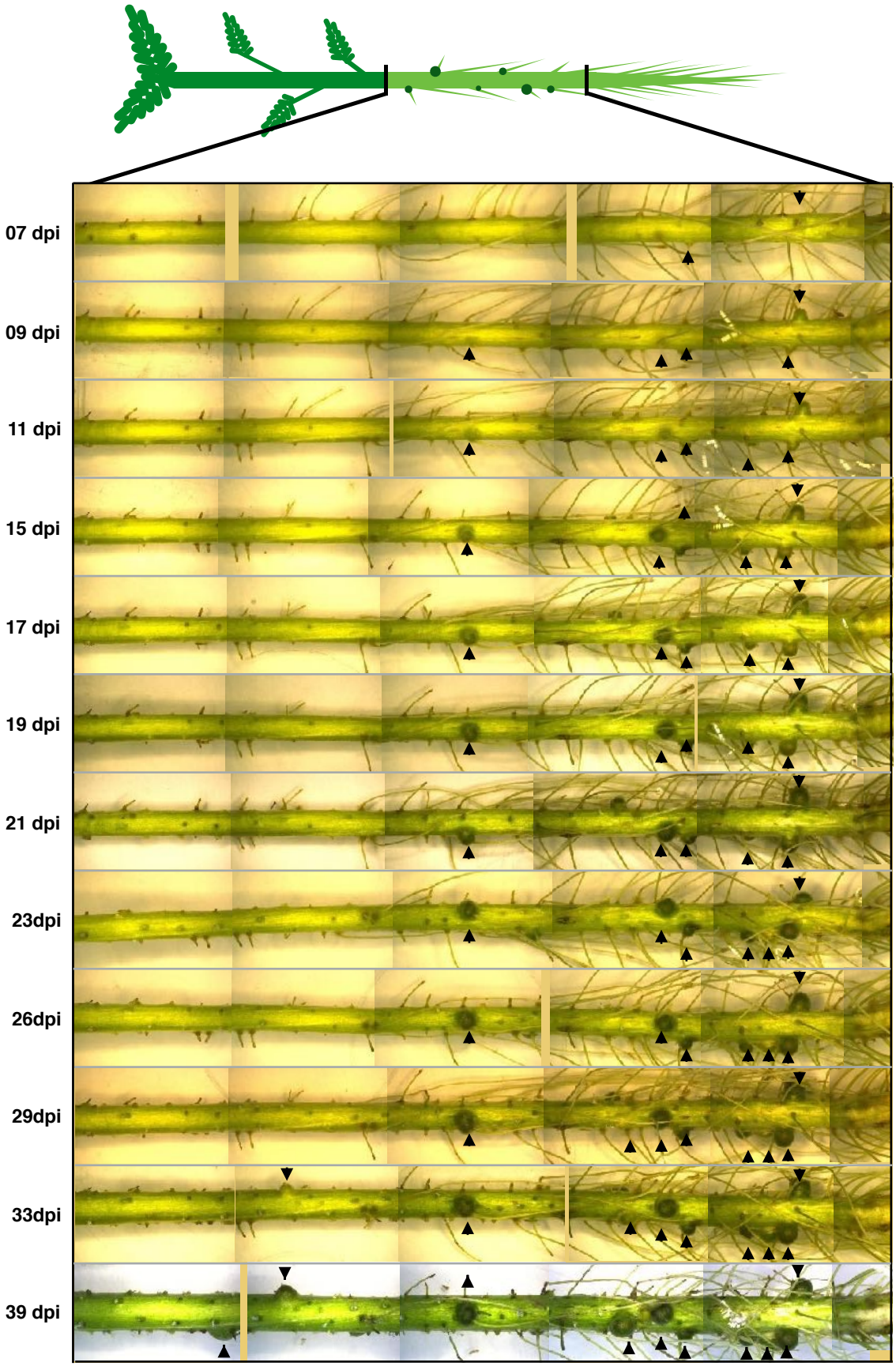
07 dpi
09 dpi
11 dpi
15 dpi
17 dpi
19 dpi
21 dpi
23dpi
26dpi
29dpi
33dpi
39 dpi

Figure S5.

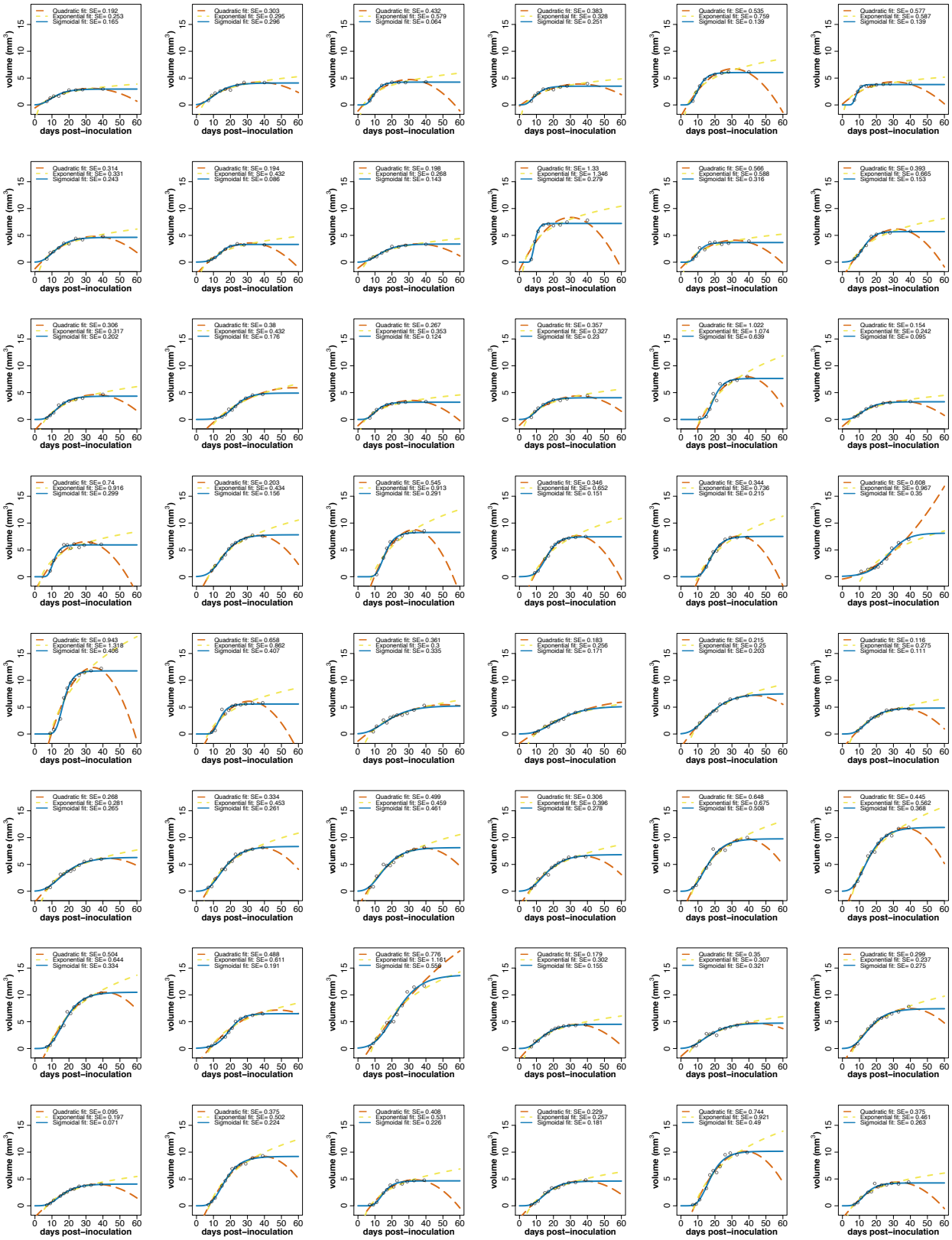
Quadratic fit: SE= 0.192
Exponential fit: SE= 0.253
Sigmoidal fit: SE= 0.165
Quadratic fit: SE= 0.303
Exponential fit: SE= 0.295
Sigmoidal fit: SE= 0.296
Quadratic fit: SE= 0.432
Exponential fit: SE= 0.579
Sigmoidal fit: SE= 0.064
Quadratic fit: SE= 0.383
Exponential fit: SE= 0.328
Sigmoidal fit: SE= 0.251
Quadratic fit: SE= 0.535
Exponential fit: SE= 0.759
Sigmoidal fit: SE= 0.139
Quadratic fit: SE= 0.577
Exponential fit: SE= 0.587
Sigmoidal fit: SE= 0.139
Quadratic fit: SE= 0.314
Exponential fit: SE= 0.331
Sigmoidal fit: SE= 0.243
Quadratic fit: SE= 0.194
Exponential fit: SE= 0.432
Sigmoidal fit: SE= 0.086
Quadratic fit: SE= 0.198
Exponential fit: SE= 0.268
Sigmoidal fit: SE= 0.143
Quadratic fit: SE= 1.33
Exponential fit: SE= 1.346
Sigmoidal fit: SE= 0.279
Quadratic fit: SE= 0.566
Exponential fit: SE= 0.588
Sigmoidal fit: SE= 0.316
Quadratic fit: SE= 0.393
Exponential fit: SE= 0.665
Sigmoidal fit: SE= 0.153
Quadratic fit: SE= 0.306
Exponential fit: SE= 0.317
Sigmoidal fit: SE= 0.202
Quadratic fit: SE= 0.38
Exponential fit: SE= 0.432
Sigmoidal fit: SE= 0.176
Quadratic fit: SE= 0.267
Exponential fit: SE= 0.353
Sigmoidal fit: SE= 0.124
Quadratic fit: SE= 0.357
Exponential fit: SE= 0.327
Sigmoidal fit: SE= 0.23
Quadratic fit: SE= 1.022
Exponential fit: SE= 1.074
Sigmoidal fit: SE= 0.639
Quadratic fit: SE= 0.154
Exponential fit: SE= 0.242
Sigmoidal fit: SE= 0.095
Quadratic fit: SE= 0.74
Exponential fit: SE= 0.916
Sigmoidal fit: SE= 0.299
Quadratic fit: SE= 0.203
Exponential fit: SE= 0.434
Sigmoidal fit: SE= 0.156
Quadratic fit: SE= 0.545
Exponential fit: SE= 0.913
Sigmoidal fit: SE= 0.291
Quadratic fit: SE= 0.346
Exponential fit: SE= 0.552
Sigmoidal fit: SE= 0.151
Quadratic fit: SE= 0.344
Exponential fit: SE= 0.736
Sigmoidal fit: SE= 0.215
Quadratic fit: SE= 0.608
Exponential fit: SE= 0.967
Sigmoidal fit: SE= 0.35
Quadratic fit: SE= 0.943
Exponential fit: SE= 1.318
Sigmoidal fit: SE= 0.406
Quadratic fit: SE= 0.658
Exponential fit: SE= 0.862
Sigmoidal fit: SE= 0.407
Quadratic fit: SE= 0.361
Exponential fit: SE= 0.3
Sigmoidal fit: SE= 0.335
Quadratic fit: SE= 0.183
Exponential fit: SE= 0.256
Sigmoidal fit: SE= 0.171
Quadratic fit: SE= 0.215
Exponential fit: SE= 0.25
Sigmoidal fit: SE= 0.203
Quadratic fit: SE= 0.116
Exponential fit: SE= 0.275
Sigmoidal fit: SE= 0.111
Quadratic fit: SE= 0.268
Exponential fit: SE= 0.281
Sigmoidal fit: SE= 0.265
Quadratic fit: SE= 0.334
Exponential fit: SE= 0.453
Sigmoidal fit: SE= 0.261
Quadratic fit: SE= 0.499
Exponential fit: SE= 0.459
Sigmoidal fit: SE= 0.461
Quadratic fit: SE= 0.306
Exponential fit: SE= 0.386
Sigmoidal fit: SE= 0.278
Quadratic fit: SE= 0.648
Exponential fit: SE= 0.675
Sigmoidal fit: SE= 0.508
Quadratic fit: SE= 0.445
Exponential fit: SE= 0.582
Sigmoidal fit: SE= 0.368
Quadratic fit: SE= 0.504
Exponential fit: SE= 0.644
Sigmoidal fit: SE= 0.334
Quadratic fit: SE= 0.488
Exponential fit: SE= 0.611
Sigmoidal fit: SE= 0.191
Quadratic fit: SE= 0.776
Exponential fit: SE= 1.161
Sigmoidal fit: SE= 0.558
Quadratic fit: SE= 0.179
Exponential fit: SE= 0.302
Sigmoidal fit: SE= 0.155
Quadratic fit: SE= 0.35
Exponential fit: SE= 0.307
Sigmoidal fit: SE= 0.321
Quadratic fit: SE= 0.299
Exponential fit: SE= 0.237
Sigmoidal fit: SE= 0.275
Quadratic fit: SE= 0.095
Exponential fit: SE= 0.197
Sigmoidal fit: SE= 0.071
Quadratic fit: SE= 0.375
Exponential fit: SE= 0.502
Sigmoidal fit: SE= 0.224
Quadratic fit: SE= 0.408
Exponential fit: SE= 0.531
Sigmoidal fit: SE= 0.226
Quadratic fit: SE= 0.229
Exponential fit: SE= 0.257
Sigmoidal fit: SE= 0.181
Quadratic fit: SE= 0.744
Exponential fit: SE= 0.921
Sigmoidal fit: SE= 0.49
Quadratic fit: SE= 0.375
Exponential fit: SE= 0.461
Sigmoidal fit: SE= 0.263
volume (mm3)
days post−inoculation

Figure S6.

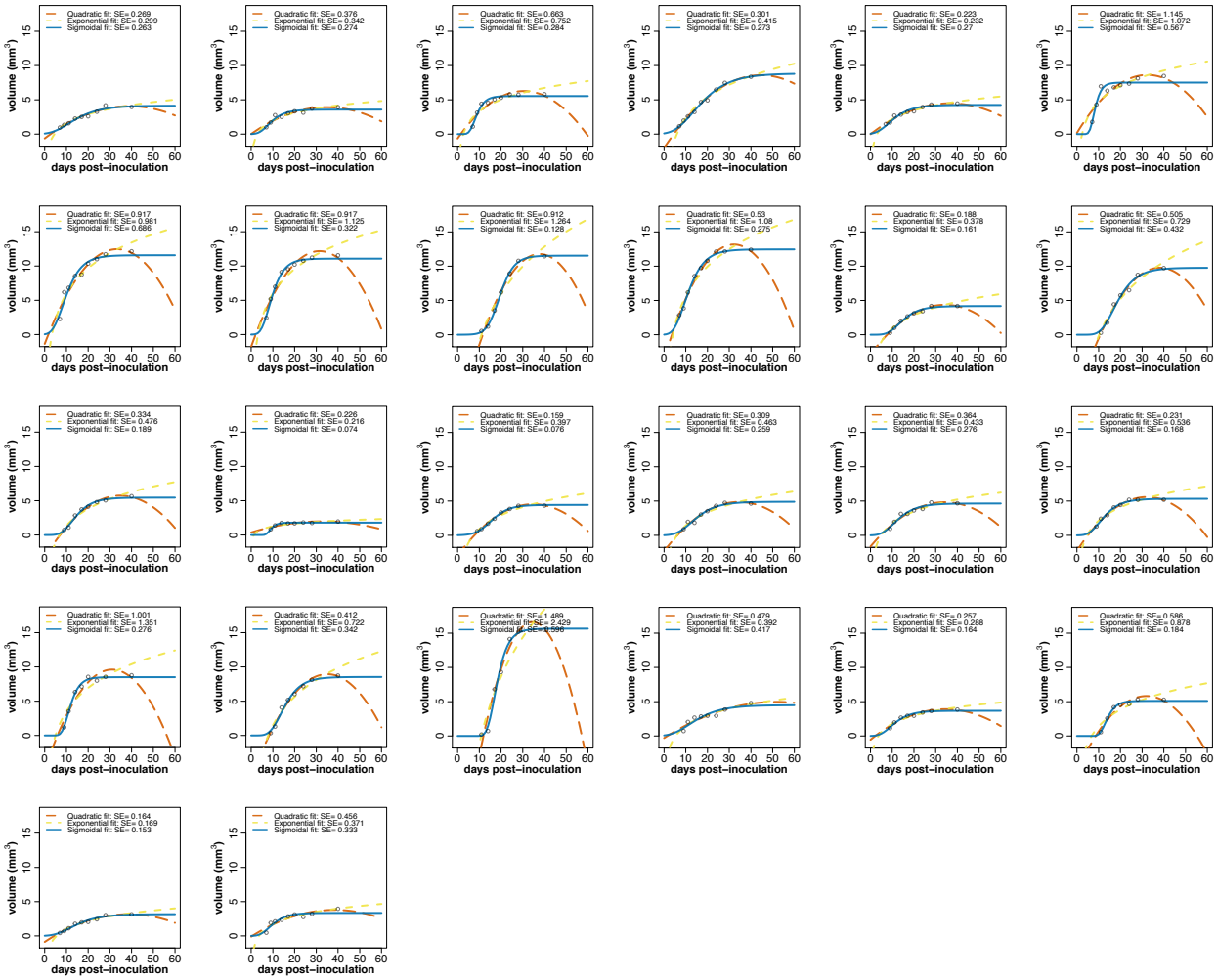

Figure S6 cont.

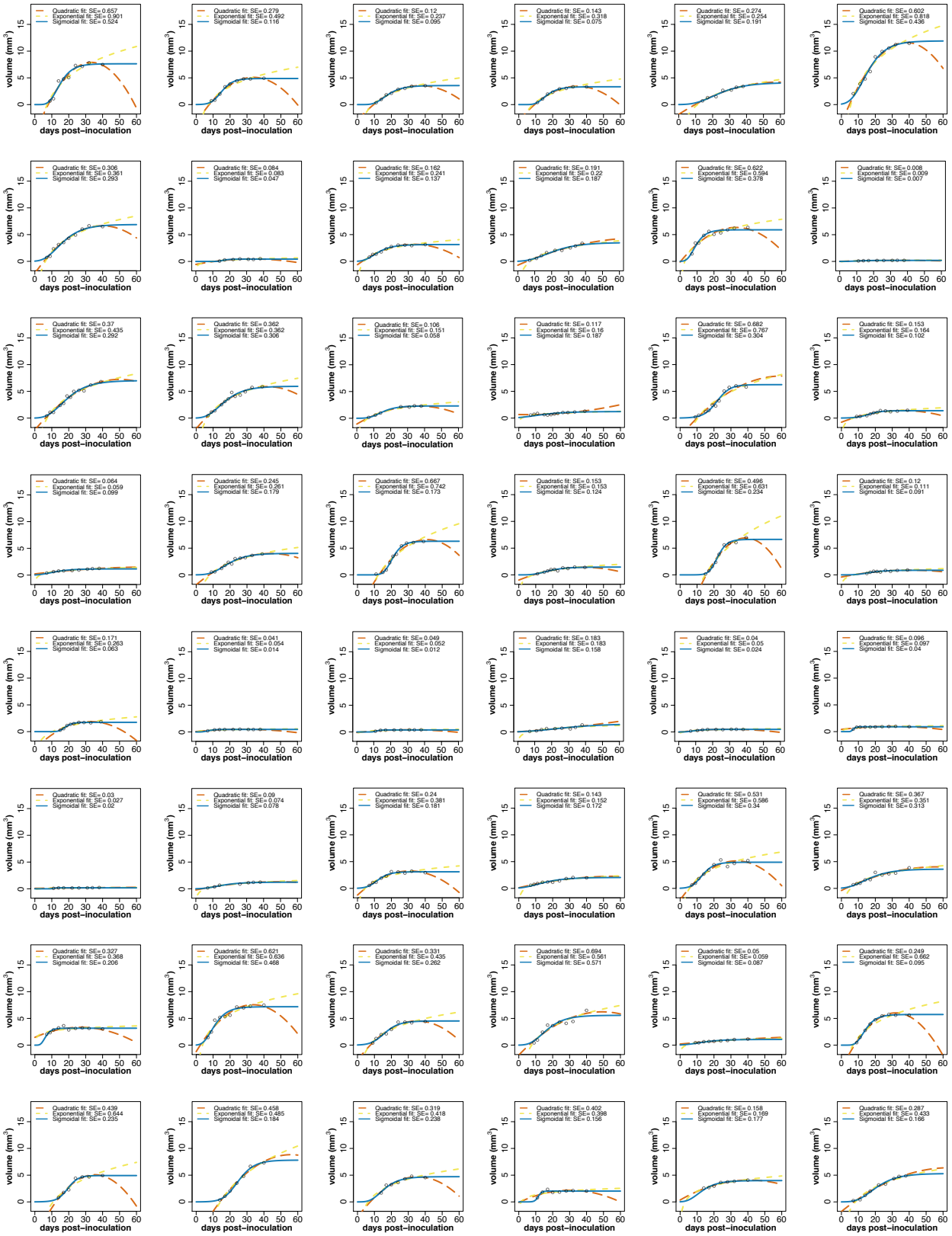
Quadratic fit: SE= 0.657
Exponential fit: SE= 0.901
Sigmoidal fit: SE= 0.524
Quadratic fit: SE= 0.279
Exponential fit: SE= 0.492
Sigmoidal fit: SE= 0.116
Quadratic fit: SE= 0.12
Exponential fit: SE= 0.237
Sigmoidal fit: SE= 0.095
Quadratic fit: SE= 0.143
Exponential fit: SE= 0.318
Sigmoidal fit: SE= 0.075
Quadratic fit: SE= 0.274
Exponential fit: SE= 0.254
Sigmoidal fit: SE= 0.191
Quadratic fit: SE= 0.602
Exponential fit: SE= 0.818
Sigmoidal fit: SE= 0.436
Quadratic fit: SE= 0.306
Exponential fit: SE= 0.361
Sigmoidal fit: SE= 0.293
Quadratic fit: SE= 0.084
Exponential fit: SE= 0.083
Sigmoidal fit: SE= 0.047
Quadratic fit: SE= 0.162
Exponential fit: SE= 0.241
Sigmoidal fit: SE= 0.137
Quadratic fit: SE= 0.191
Exponential fit: SE= 0.22
Sigmoidal fit: SE= 0.187
Quadratic fit: SE= 0.622
Exponential fit: SE= 0.594
Sigmoidal fit: SE= 0.378
Quadratic fit: SE= 0.008
Exponential fit: SE= 0.009
Sigmoidal fit: SE= 0.007
Quadratic fit: SE= 0.37
Exponential fit: SE= 0.435
Sigmoidal fit: SE= 0.292
Quadratic fit: SE= 0.362
Exponential fit: SE= 0.362
Sigmoidal fit: SE= 0.306
Quadratic fit: SE= 0.106
Exponential fit: SE= 0.151
Sigmoidal fit: SE= 0.058
Quadratic fit: SE= 0.117
Exponential fit: SE= 0.16
Sigmoidal fit: SE= 0.187
Quadratic fit: SE= 0.682
Exponential fit: SE= 0.767
Sigmoidal fit: SE= 0.304
Quadratic fit: SE= 0.153
Exponential fit: SE= 0.164
Sigmoidal fit: SE= 0.102
Quadratic fit: SE= 0.064
Exponential fit: SE= 0.059
Sigmoidal fit: SE= 0.099
Quadratic fit: SE= 0.245
Exponential fit: SE= 0.261
Sigmoidal fit: SE= 0.179
Quadratic fit: SE= 0.667
Exponential fit: SE= 0.742
Sigmoidal fit: SE= 0.173
Quadratic fit: SE= 0.153
Exponential fit: SE= 0.153
Sigmoidal fit: SE= 0.124
Quadratic fit: SE= 0.496
Exponential fit: SE= 0.631
Sigmoidal fit: SE= 0.234
Quadratic fit: SE= 0.12
Exponential fit: SE= 0.111
Sigmoidal fit: SE= 0.091
Quadratic fit: SE= 0.171
Exponential fit: SE= 0.263
Sigmoidal fit: SE= 0.063
Quadratic fit: SE= 0.041
Exponential fit: SE= 0.054
Sigmoidal fit: SE= 0.014
Quadratic fit: SE= 0.049
Exponential fit: SE= 0.052
Sigmoidal fit: SE= 0.012
Quadratic fit: SE= 0.183
Exponential fit: SE= 0.183
Sigmoidal fit: SE= 0.158
Quadratic fit: SE= 0.04
Exponential fit: SE= 0.05
Sigmoidal fit: SE= 0.024
Quadratic fit: SE= 0.096
Exponential fit: SE= 0.097
Sigmoidal fit: SE= 0.04
Quadratic fit: SE= 0.03
Exponential fit: SE= 0.027
Sigmoidal fit: SE= 0.02
Quadratic fit: SE= 0.09
Exponential fit: SE= 0.074
Sigmoidal fit: SE= 0.078
Quadratic fit: SE= 0.24
Exponential fit: SE= 0.381
Sigmoidal fit: SE= 0.181
Quadratic fit: SE= 0.143
Exponential fit: SE= 0.152
Sigmoidal fit: SE= 0.172
Quadratic fit: SE= 0.531
Exponential fit: SE= 0.586
Sigmoidal fit: SE= 0.34
Quadratic fit: SE= 0.367
Exponential fit: SE= 0.351
Sigmoidal fit: SE= 0.313
Quadratic fit: SE= 0.327
Exponential fit: SE= 0.368
Sigmoidal fit: SE= 0.206
Quadratic fit: SE= 0.621
Exponential fit: SE= 0.636
Sigmoidal fit: SE= 0.468
Quadratic fit: SE= 0.331
Exponential fit: SE= 0.435
Sigmoidal fit: SE= 0.262
Quadratic fit: SE= 0.694
Exponential fit: SE= 0.561
Sigmoidal fit: SE= 0.571
Quadratic fit: SE= 0.05
Exponential fit: SE= 0.059
Sigmoidal fit: SE= 0.087
Quadratic fit: SE= 0.249
Exponential fit: SE= 0.662
Sigmoidal fit: SE= 0.095
Quadratic fit: SE= 0.439
Exponential fit: SE= 0.644
Sigmoidal fit: SE= 0.235
Quadratic fit: SE= 0.458
Exponential fit: SE= 0.485
Sigmoidal fit: SE= 0.184
Quadratic fit: SE= 0.319
Exponential fit: SE= 0.418
Sigmoidal fit: SE= 0.238
Quadratic fit: SE= 0.402
Exponential fit: SE= 0.398
Sigmoidal fit: SE= 0.156
Quadratic fit: SE= 0.158
Exponential fit: SE= 0.169
Sigmoidal fit: SE= 0.177
Quadratic fit: SE= 0.287
Exponential fit: SE= 0.433
Sigmoidal fit: SE= 0.166
volume (mm^3)
days post−inoculation

Figure S7.

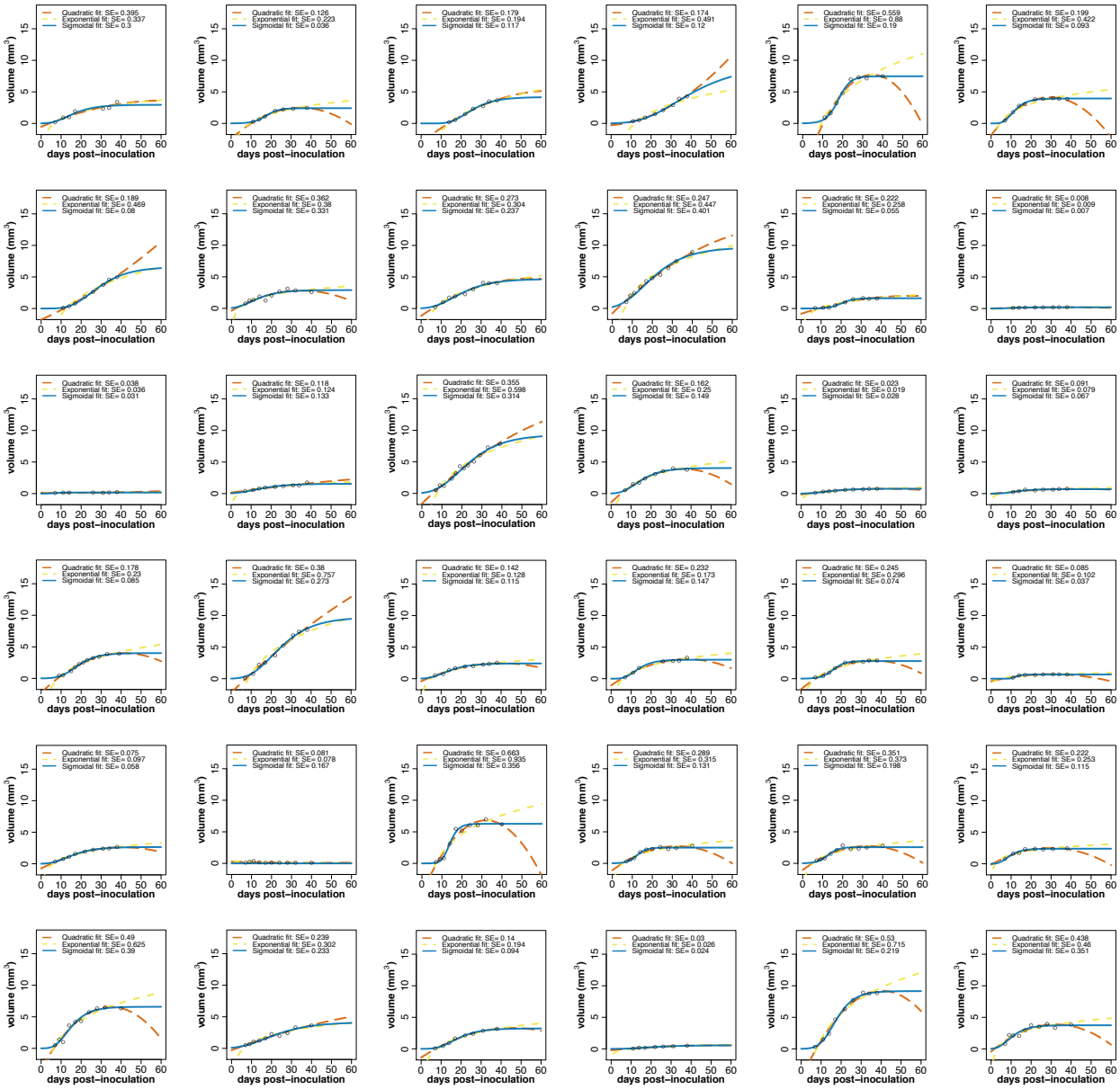

Figure S7 cont.

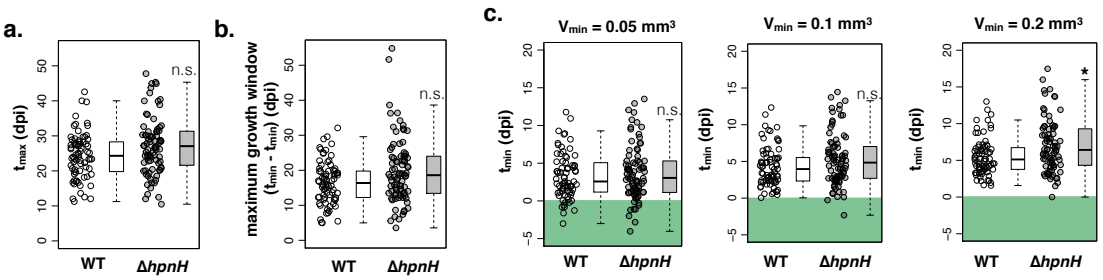
a.
b.
c.
t_{max} (dpi)
maximum growth window
(t_{min} - t_{min}) (dpi)
V_{min} = 0.05 mm³
V_{min} = 0.1 mm³
V_{min} = 0.2 mm³
t_{min} (dpi)
n.s.
*
WT
Δ*hpnH*

Figure S8.

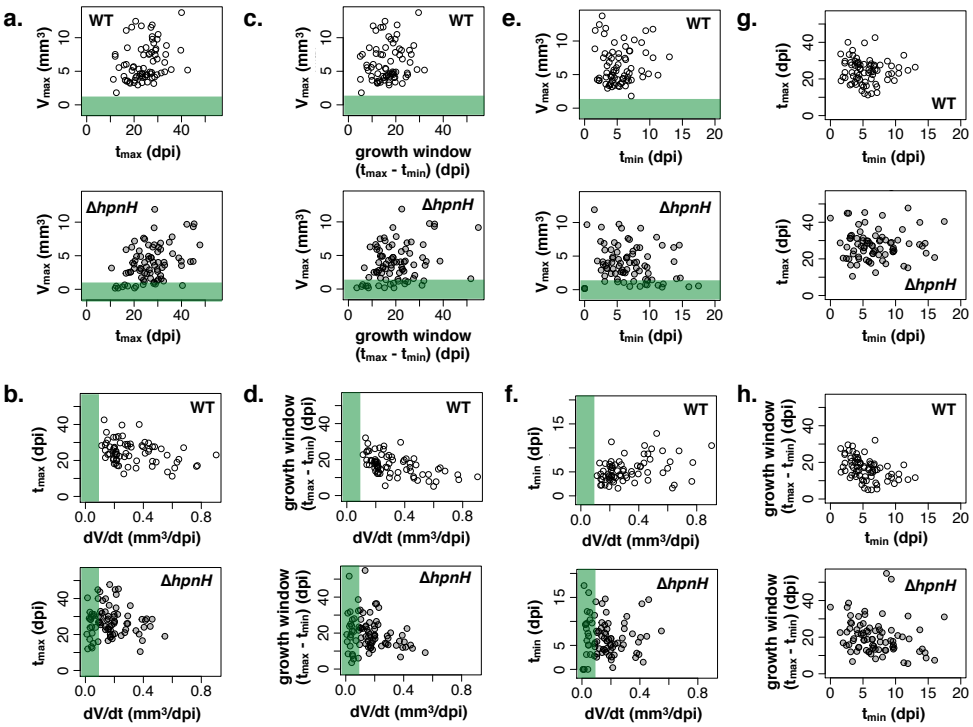
a.
WT
Vmax (mm3)
tmax (dpi)
ΔhpnH
b.
tmax (dpi)
dV/dt (mm3/dpi)
c.
growth window
(tmax - tmin) (dpi)
d.
e.
tmin (dpi)
f.
tmin (dpi)
g.
h.

Figure S9.

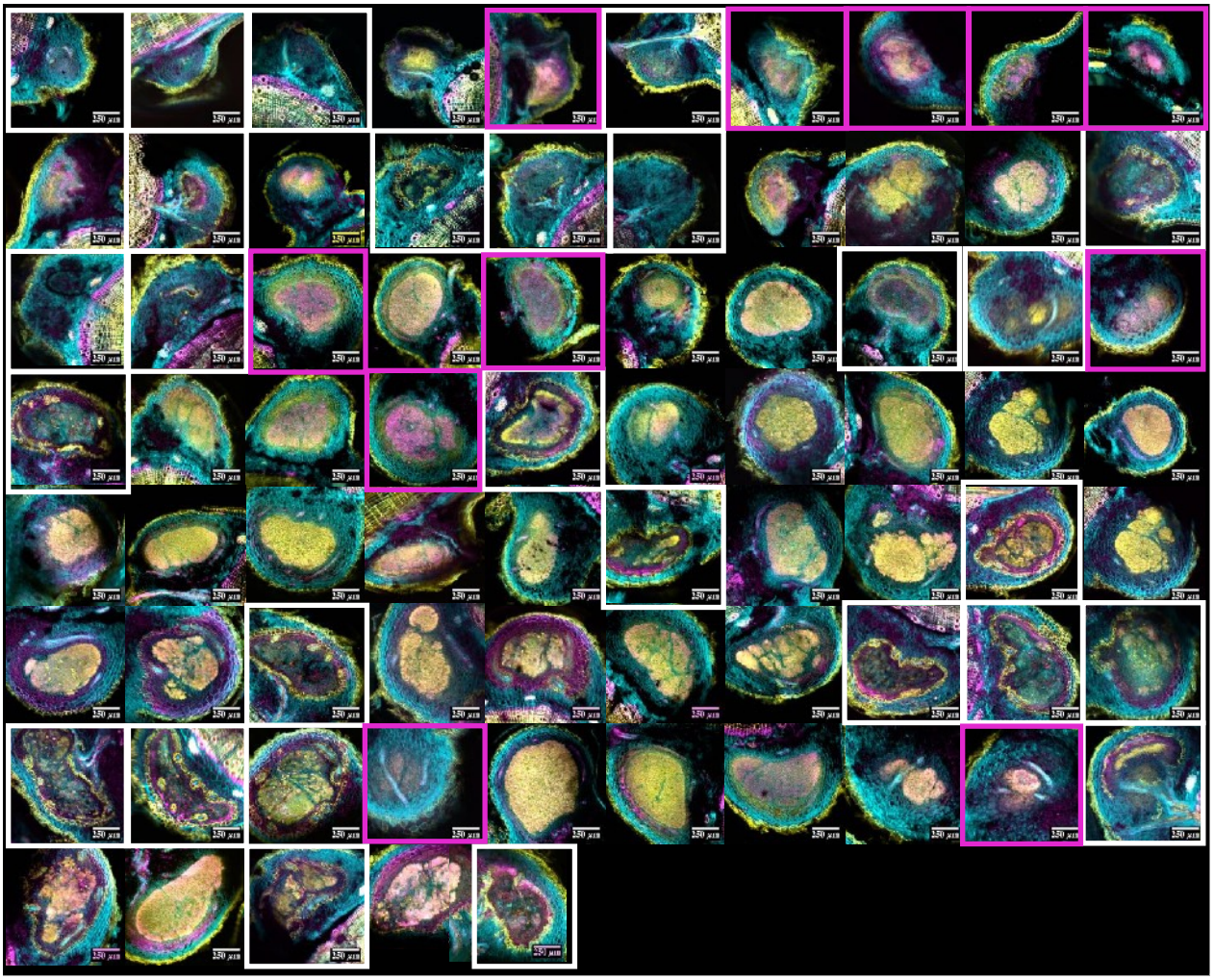

Figure S10.

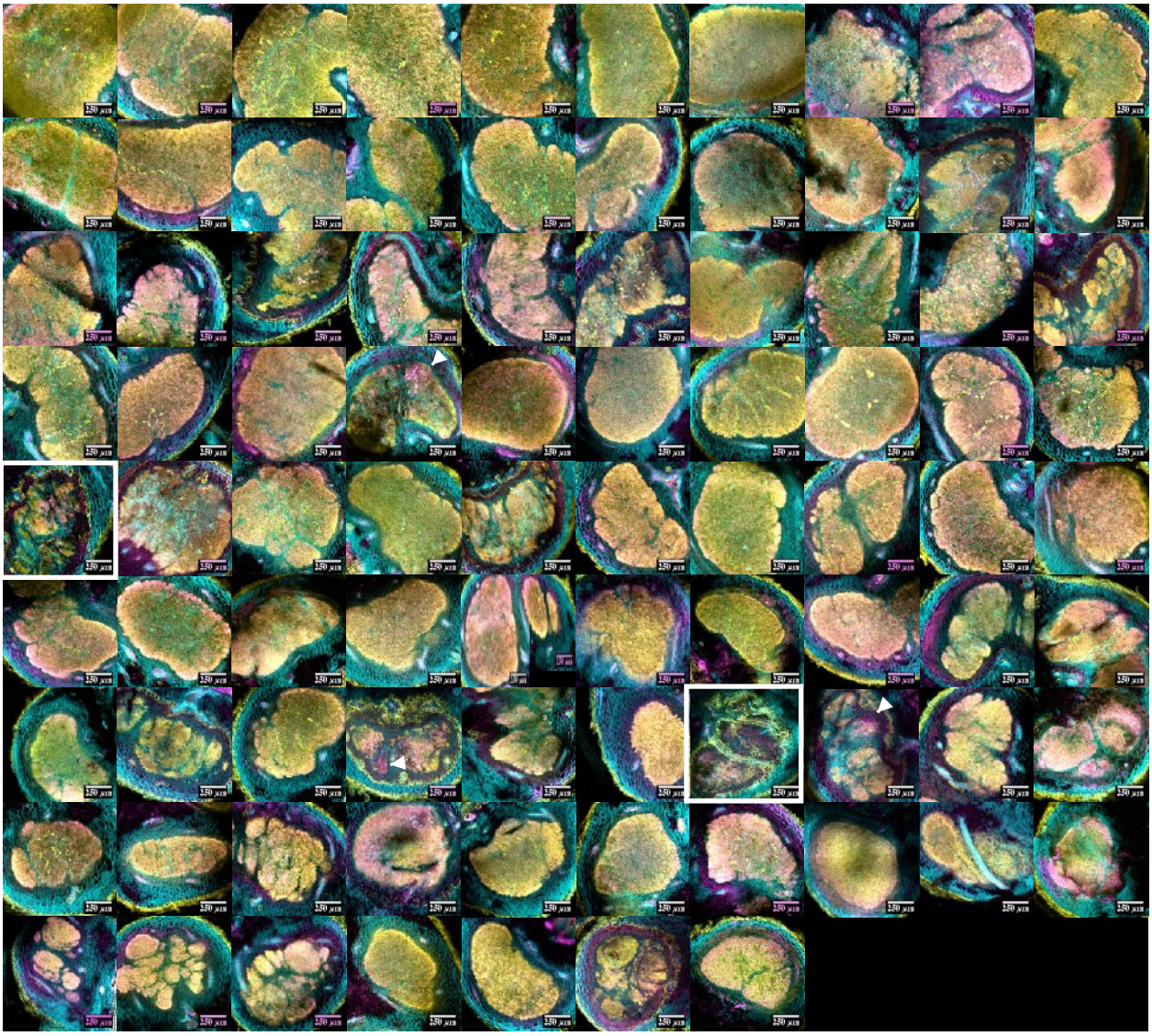

Figure S11.

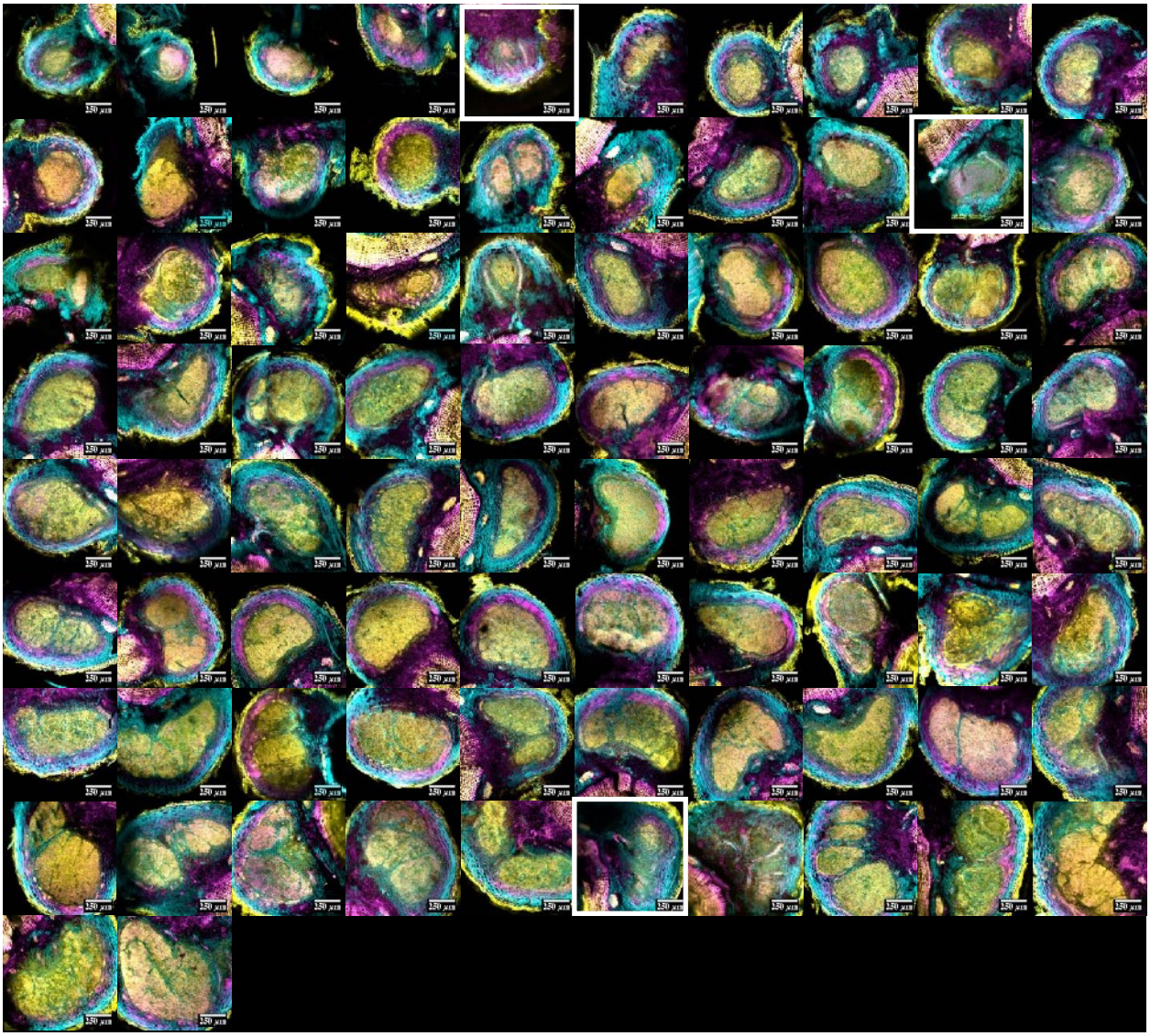

Figure S12.

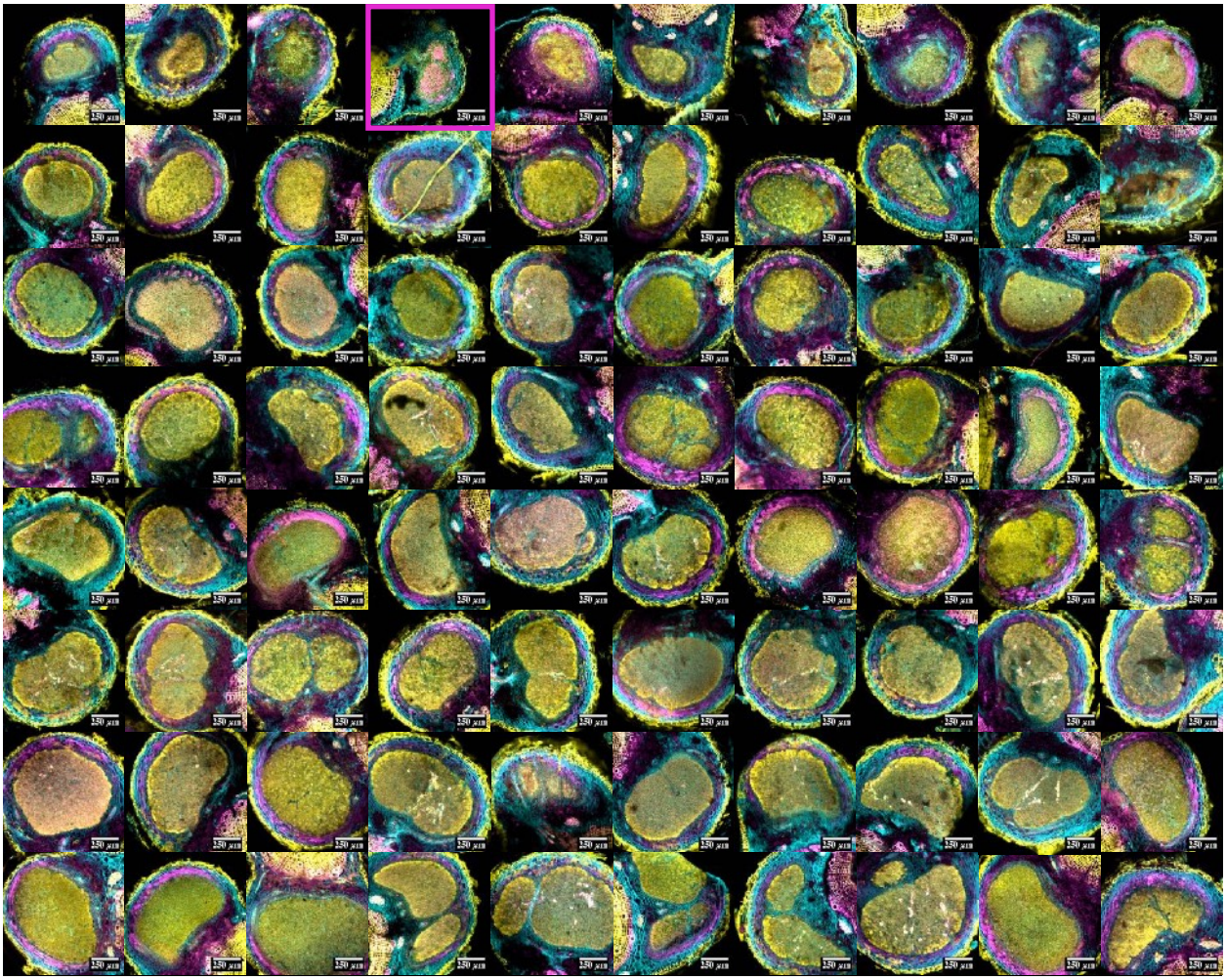

Figure S13.

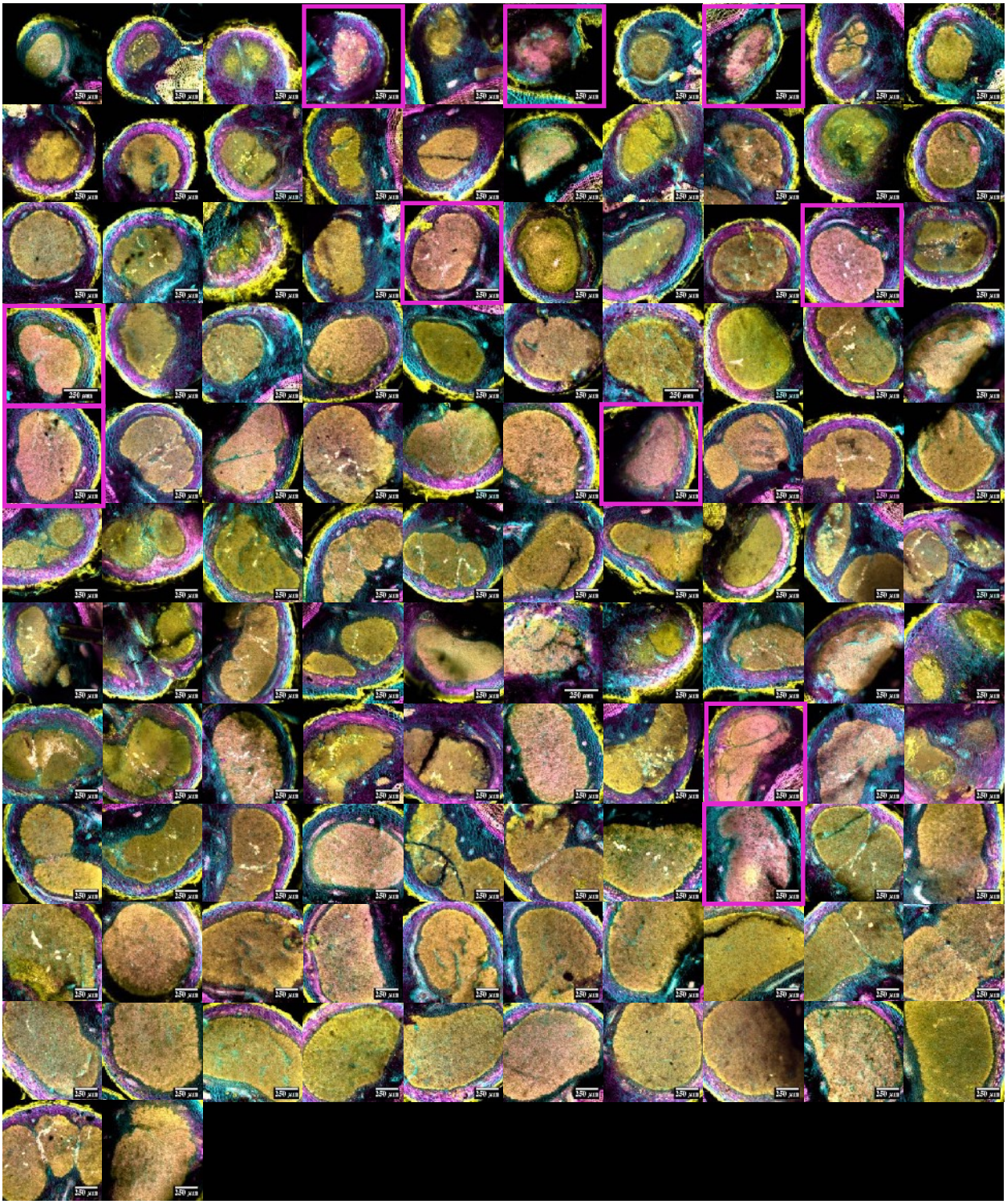

Figure S14.

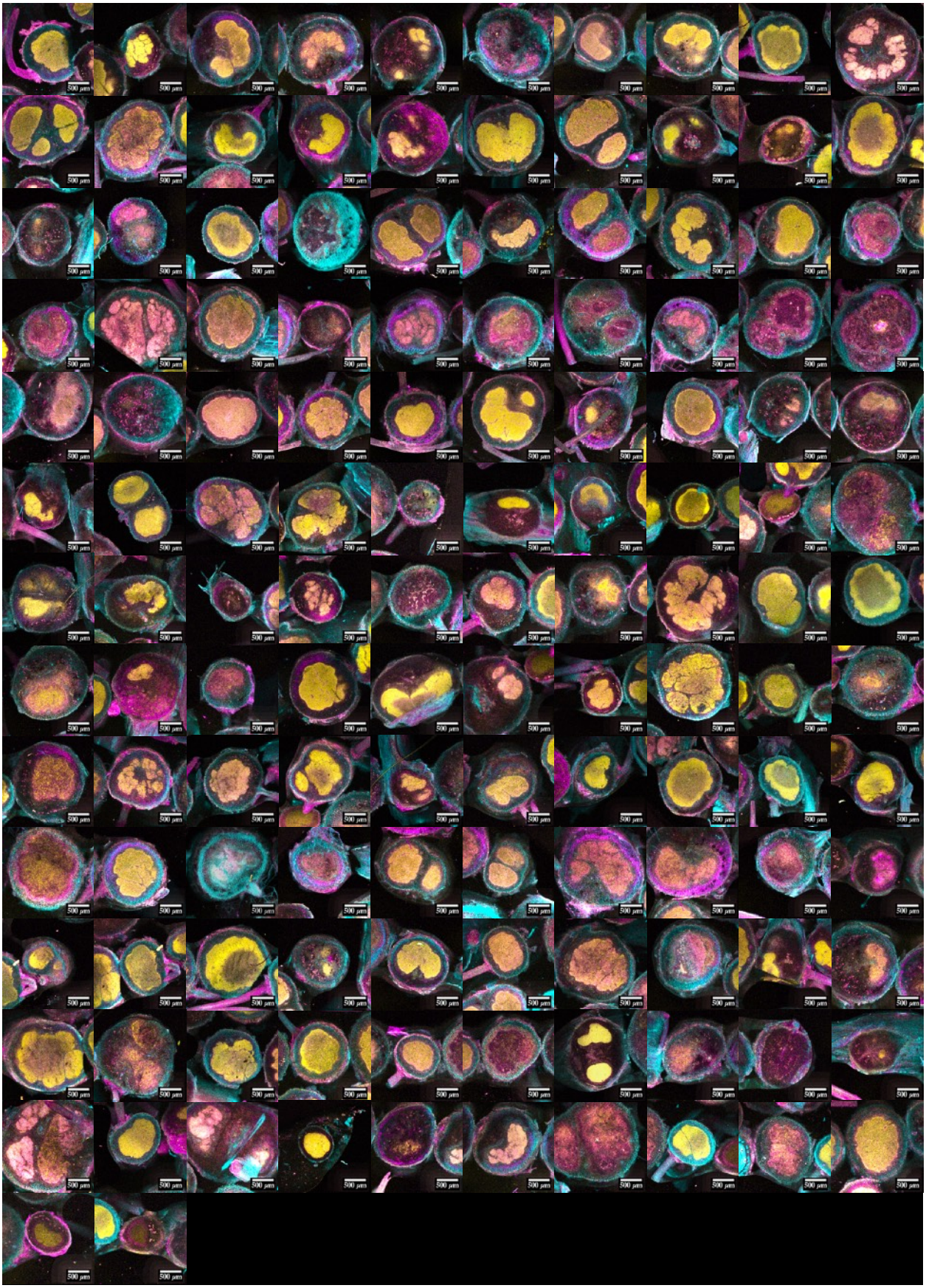

Figure S15.

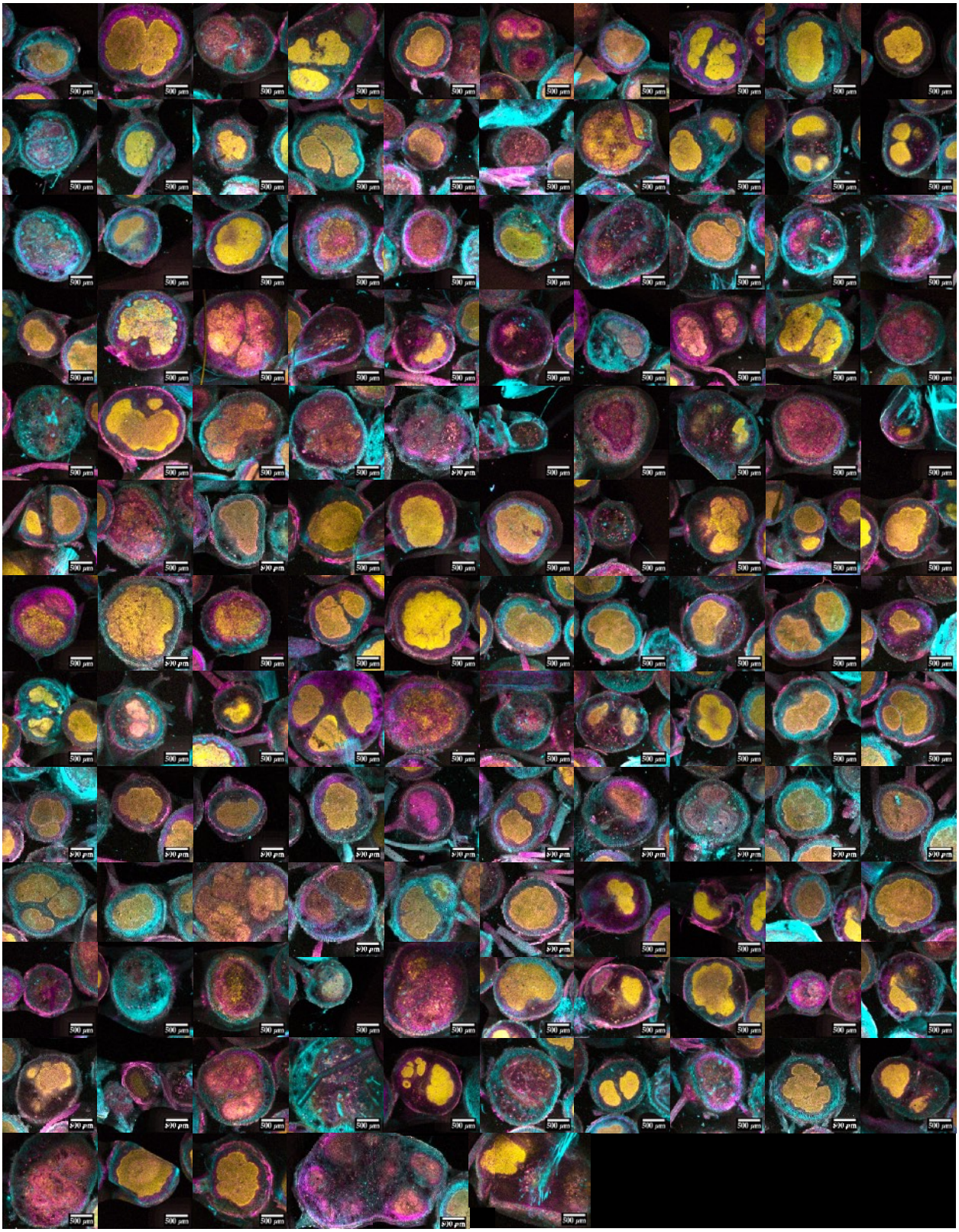

Figure S16.

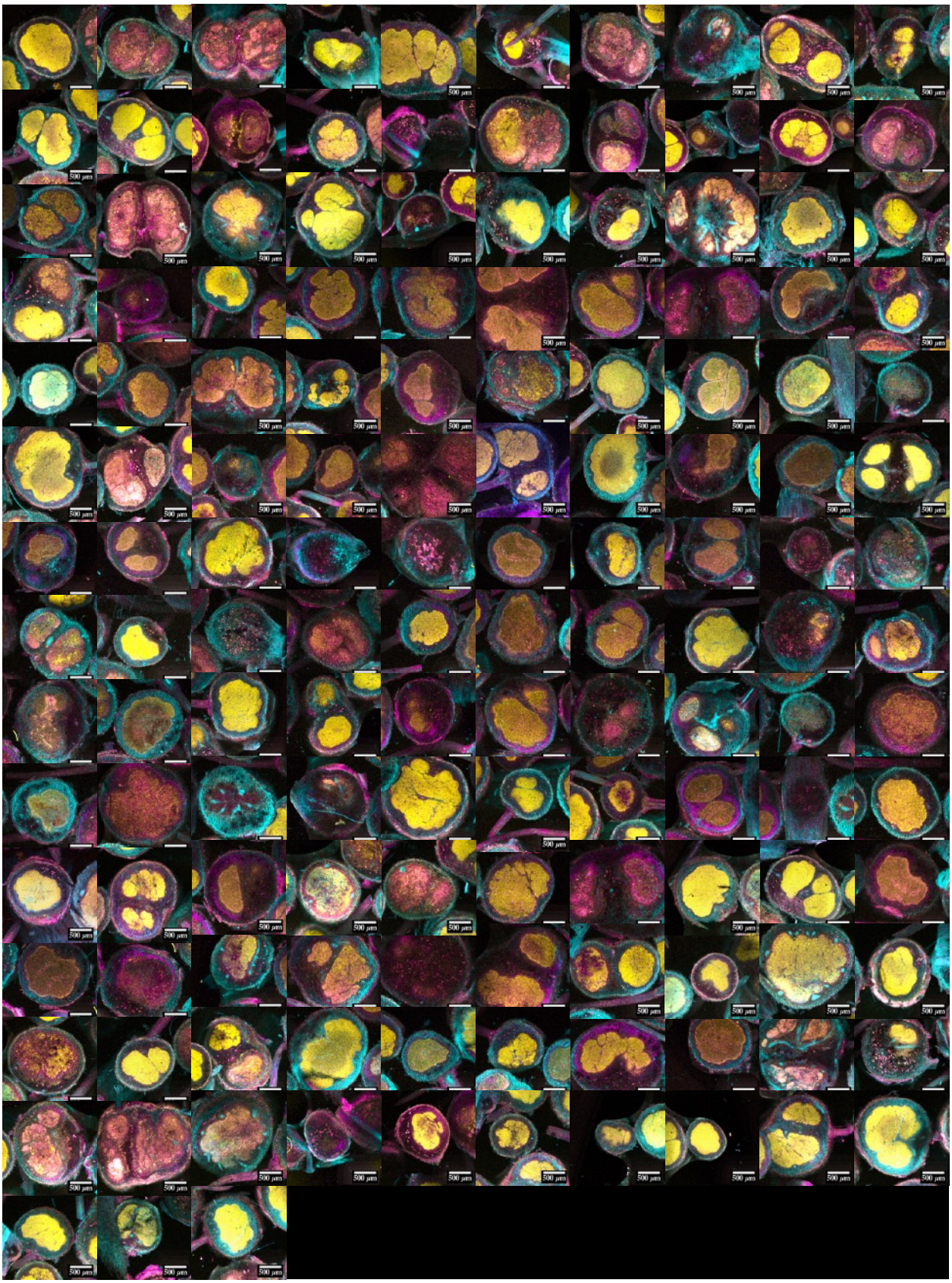

Figure S17.

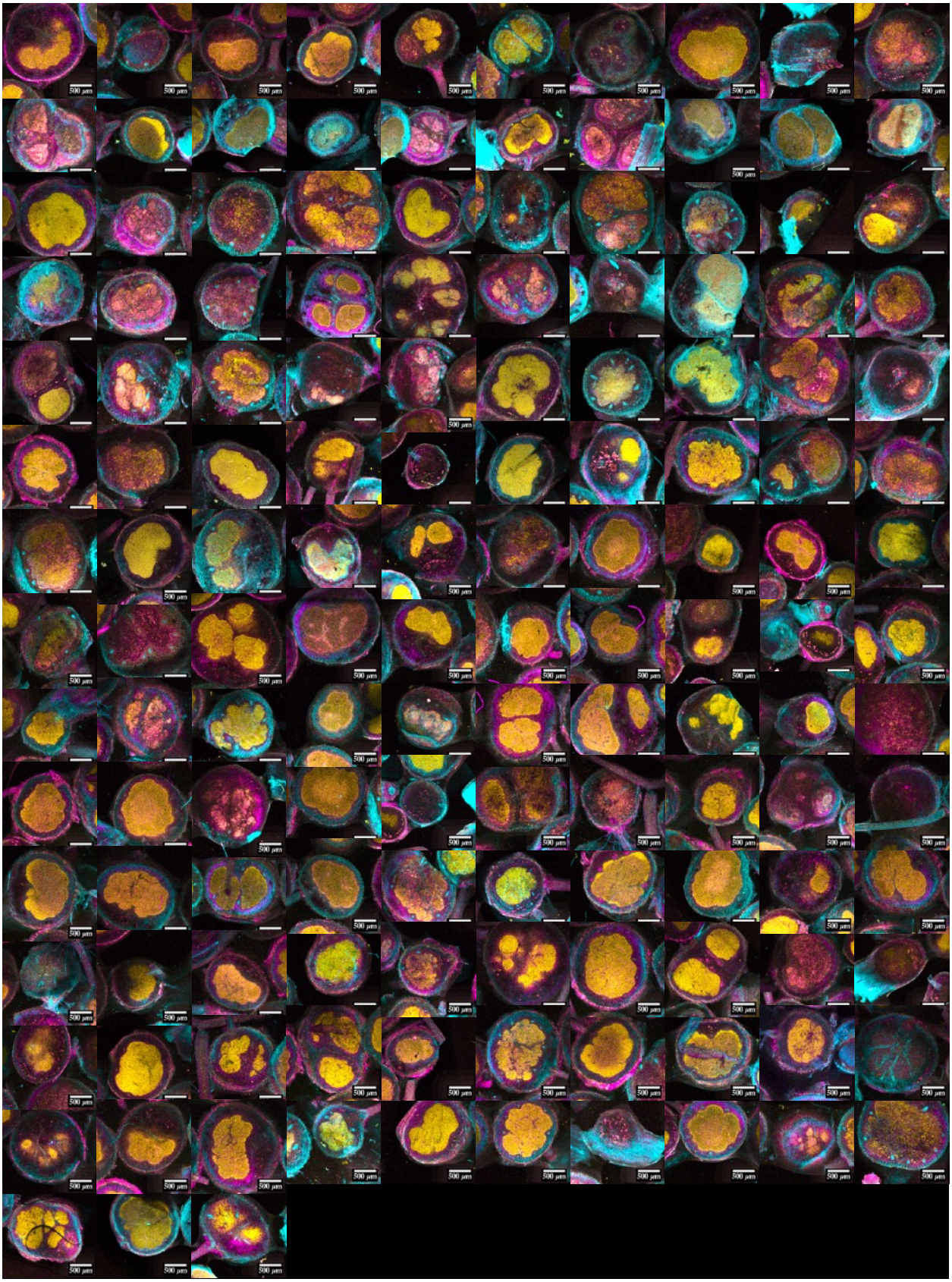

Figure S18.

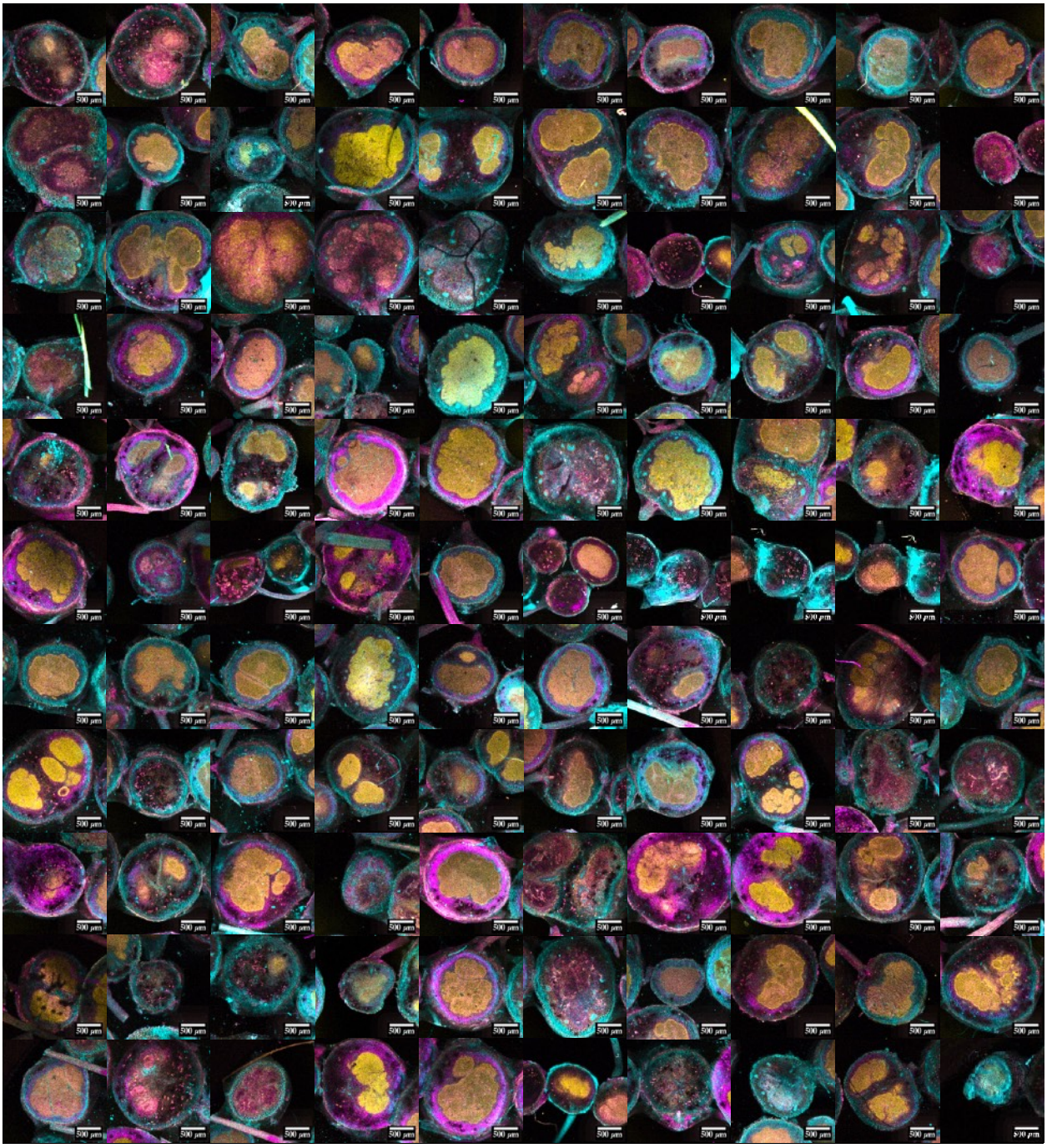

Figure S19.

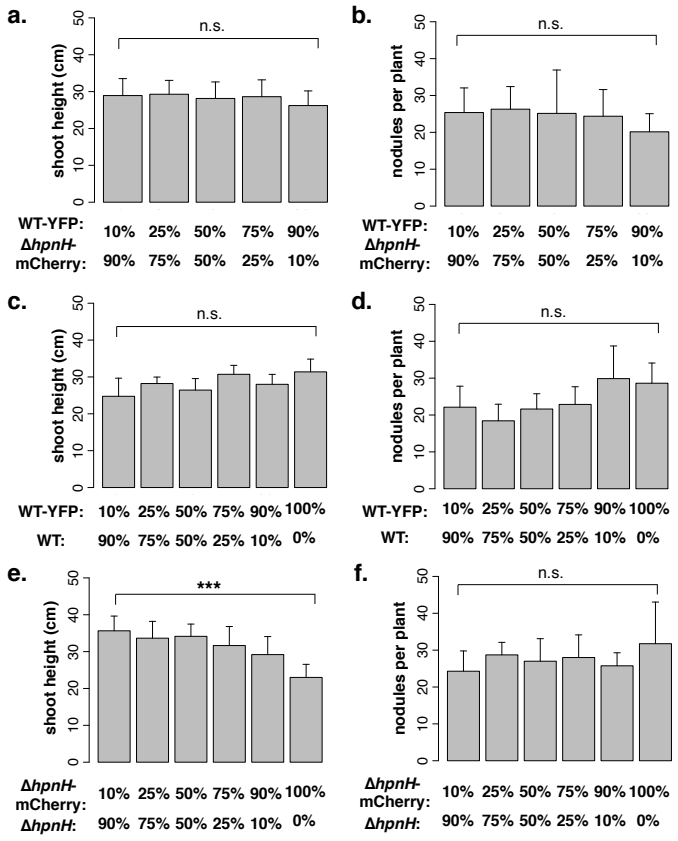
a.
shoot height (cm)
n.s.
WT-YFP: 10% 25% 50% 75% 90%
ΔhpnH-mCherry: 90% 75% 50% 25% 10%
b.
nodules per plant
n.s.
WT-YFP: 10% 25% 50% 75% 90%
ΔhpnH-mCherry: 90% 75% 50% 25% 10%
c.
shoot height (cm)
n.s.
WT-YFP: 10% 25% 50% 75% 90% 100%
WT: 90% 75% 50% 25% 10% 0%
d.
nodules per plant
n.s.
WT-YFP: 10% 25% 50% 75% 90% 100%
WT: 90% 75% 50% 25% 10% 0%
e.
shoot height (cm)
***
ΔhpnH-mCherry: 10% 25% 50% 75% 90% 100%
ΔhpnH: 90% 75% 50% 25% 10% 0%
f.
nodules per plant
n.s.
ΔhpnH-mCherry: 10% 25% 50% 75% 90% 100%
ΔhpnH: 90% 75% 50% 25% 10% 0%

Figure S20.

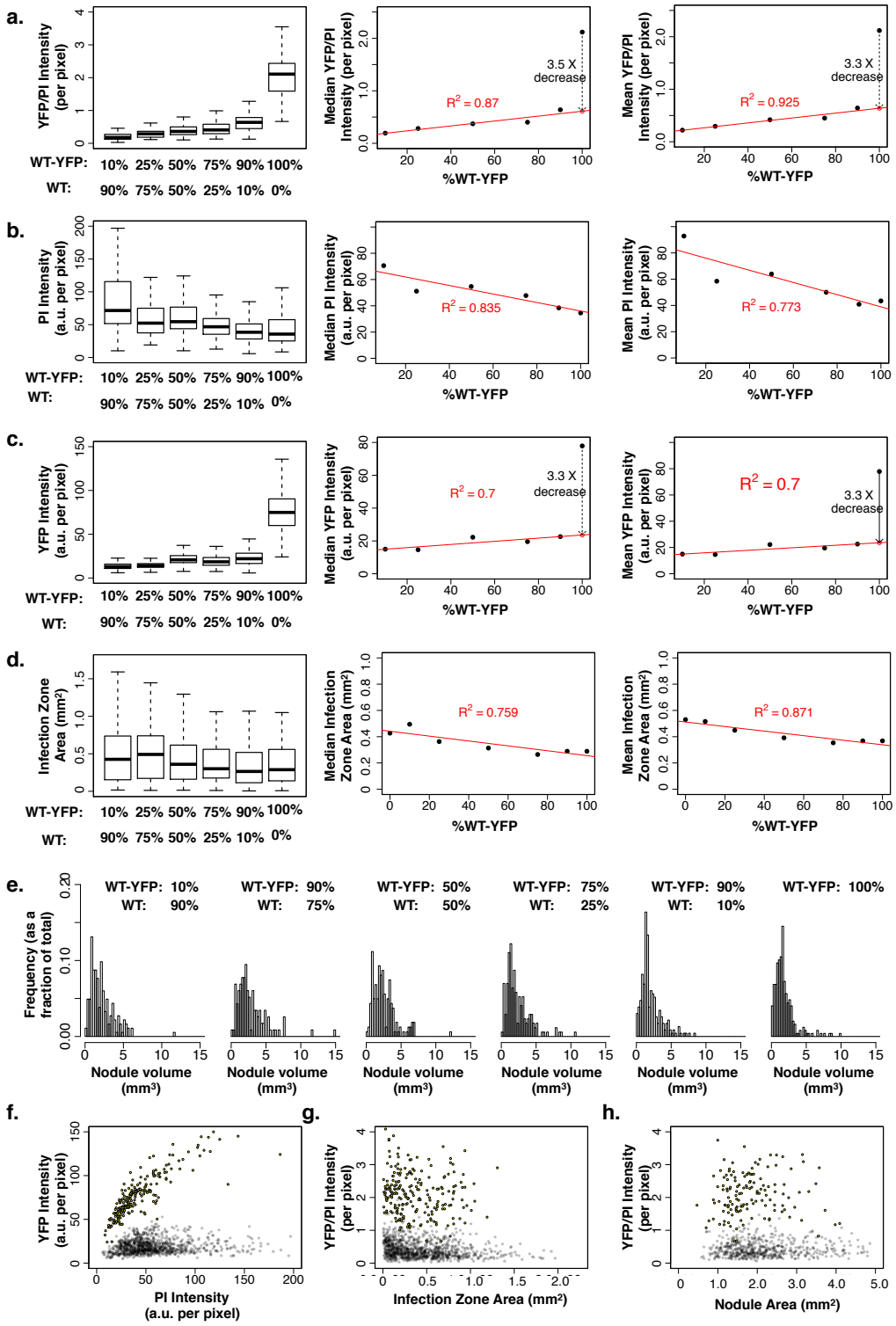
a.
YFP/PI Intensity (per pixel)
WT-YFP: 10% 25% 50% 75% 90% 100%
WT: 90% 75% 50% 25% 10% 0%
Median YFP/PI Intensity (per pixel)
3.5 X decrease
R2 = 0.87
%WT-YFP
Mean YFP/PI Intensity (per pixel)
3.3 X decrease
R2 = 0.925
b.
PI Intensity (a.u. per pixel)
Median PI Intensity (a.u. per pixel)
R2 = 0.835
Mean PI Intensity (a.u. per pixel)
R2 = 0.773
c.
YFP Intensity (a.u. per pixel)
Median YFP Intensity (a.u. per pixel)
R2 = 0.7
3.3 X decrease
Mean YFP Intensity (a.u. per pixel)
R2 = 0.7
d.
Infection Zone Area (mm2)
Median Infection Zone Area (mm2)
R2 = 0.759
Mean Infection Zone Area (mm2)
R2 = 0.871
e.
Frequency (as a fraction of total)
WT-YFP: 10% WT: 90%
WT-YFP: 90% WT: 75%
WT-YFP: 50% WT: 50%
WT-YFP: 75% WT: 25%
WT-YFP: 90% WT: 10%
WT-YFP: 100%
Nodule volume (mm3)
f.
YFP Intensity (a.u. per pixel)
PI Intensity (a.u. per pixel)
g.
YFP/PI Intensity (per pixel)
Infection Zone Area (mm2)
h.
YFP/PI Intensity (per pixel)
Nodule Area (mm2)

Figure S21.

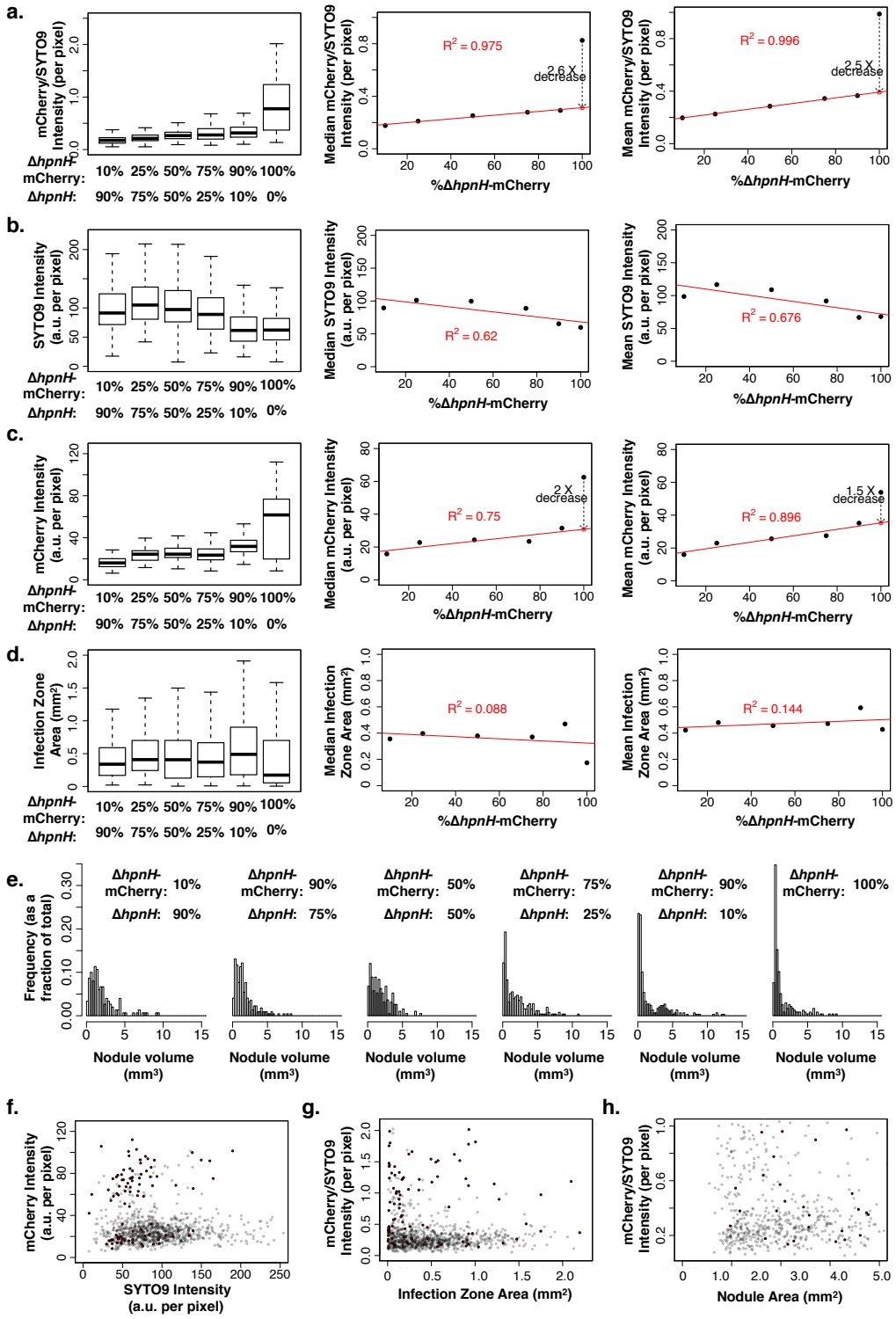
a.
mCherry/SYTO9 Intensity (per pixel)
ΔhpnH-mCherry: 10% 25% 50% 75% 90% 100%
ΔhpnH: 90% 75% 50% 25% 10% 0%
Median mCherry/SYTO9 Intensity (per pixel)
R2 = 0.975
2.6 X decrease
%ΔhpnH-mCherry
Mean mCherry/SYTO9 Intensity (per pixel)
R2 = 0.996
2.5 X decrease
%ΔhpnH-mCherry
b.
SYTO9 Intensity (a.u. per pixel)
Median SYTO9 Intensity (a.u. per pixel)
R2 = 0.62
Mean SYTO9 Intensity (a.u. per pixel)
R2 = 0.676
c.
mCherry Intensity (a.u. per pixel)
Median mCherry Intensity (a.u. per pixel)
R2 = 0.75
2 X decrease
Mean mCherry Intensity (a.u. per pixel)
R2 = 0.896
1.5 X decrease
d.
Infection Zone Area (mm2)
Median Infection Zone Area (mm2)
R2 = 0.088
Mean Infection Zone Area (mm2)
R2 = 0.144
e.
Frequency (as a fraction of total)
ΔhpnH-mCherry: 10% ΔhpnH: 90%
ΔhpnH-mCherry: 90% ΔhpnH: 75%
ΔhpnH-mCherry: 50% ΔhpnH: 50%
ΔhpnH-mCherry: 75% ΔhpnH: 25%
ΔhpnH-mCherry: 90% ΔhpnH: 10%
ΔhpnH-mCherry: 100%
Nodule volume (mm3)
f.
mCherry Intensity (a.u. per pixel)
SYTO9 Intensity (a.u. per pixel)
g.
mCherry/SYTO9 Intensity (per pixel)
Infection Zone Area (mm2)
h.
mCherry/SYTO9 Intensity (per pixel)
Nodule Area (mm2)

Figure S22.

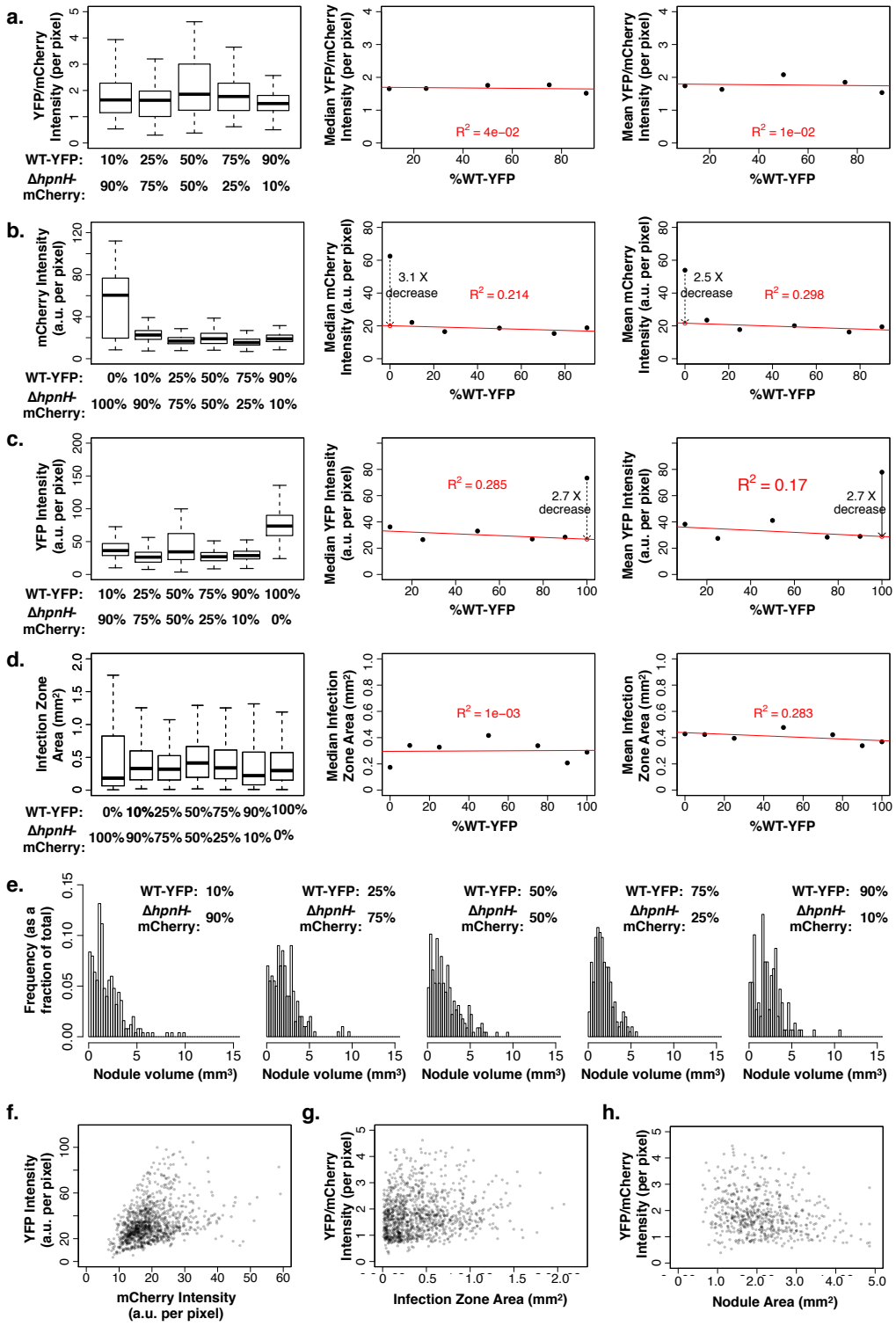
a.
YFP/mCherry Intensity (per pixel)
WT-YFP: 10% 25% 50% 75% 90%
ΔhpnH-mCherry: 90% 75% 50% 25% 10%
Median YFP/mCherry Intensity (per pixel)
R2 = 4e−02
%WT-YFP
Mean YFP/mCherry Intensity (per pixel)
R2 = 1e−02
%WT-YFP
b.
mCherry Intensity (a.u. per pixel)
WT-YFP: 0% 10% 25% 50% 75% 90%
ΔhpnH-mCherry: 100% 90% 75% 50% 25% 10%
Median mCherry Intensity (a.u. per pixel)
3.1 X decrease
R2 = 0.214
%WT-YFP
Mean mCherry Intensity (a.u. per pixel)
2.5 X decrease
R2 = 0.298
%WT-YFP
c.
YFP Intensity (a.u. per pixel)
WT-YFP: 10% 25% 50% 75% 90% 100%
ΔhpnH-mCherry: 90% 75% 50% 25% 10% 0%
Median YFP Intensity (a.u. per pixel)
R2 = 0.285
2.7 X decrease
%WT-YFP
Mean YFP Intensity (a.u. per pixel)
R2 = 0.17
2.7 X decrease
%WT-YFP
d.
Infection Zone Area (mm2)
WT-YFP: 0% 10% 25% 50% 75% 90% 100%
ΔhpnH-mCherry: 100% 90% 75% 50% 25% 10% 0%
Median Infection Zone Area (mm2)
R2 = 1e−03
%WT-YFP
Mean Infection Zone Area (mm2)
R2 = 0.283
%WT-YFP
e.
Frequency (as a fraction of total)
WT-YFP: 10% ΔhpnH-mCherry: 90%
WT-YFP: 25% ΔhpnH-mCherry: 75%
WT-YFP: 50% ΔhpnH-mCherry: 50%
WT-YFP: 75% ΔhpnH-mCherry: 25%
WT-YFP: 90% ΔhpnH-mCherry: 10%
Nodule volume (mm3)
f.
YFP Intensity (a.u. per pixel)
mCherry Intensity (a.u. per pixel)
g.
YFP/mCherry Intensity (per pixel)
Infection Zone Area (mm2)
h.
YFP/mCherry Intensity (per pixel)
Nodule Area (mm2)

Figure S23.

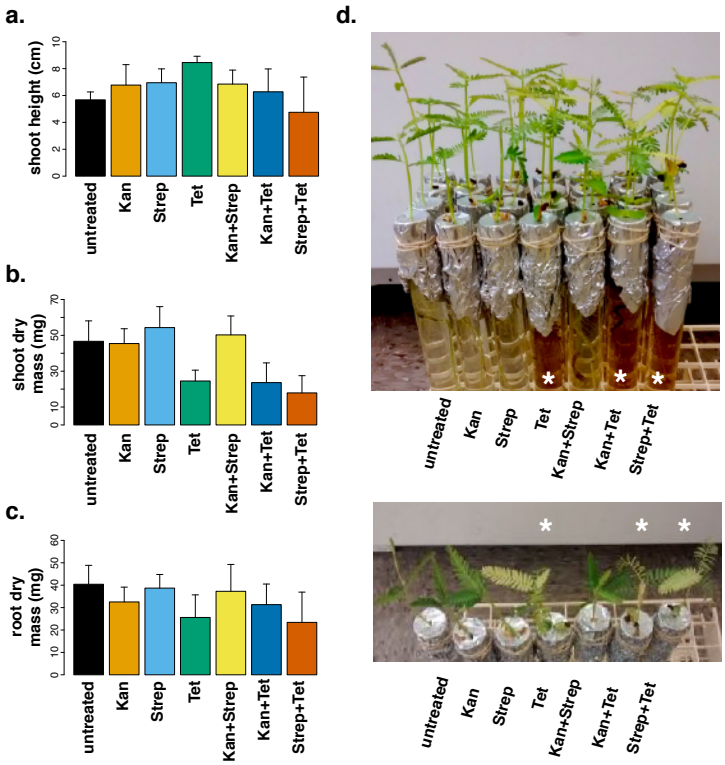
a.
shoot height (cm)
0
2
4
6
8
10
untreated
Kan
Strep
Tet
Kan+Strep
Kan+Tet
Strep+Tet
b.
shoot dry mass (mg)
0
10
30
50
70
untreated
Kan
Strep
Tet
Kan+Strep
Kan+Tet
Strep+Tet
c.
root dry mass (mg)
0
10
20
30
40
50
60
untreated
Kan
Strep
Tet
Kan+Strep
Kan+Tet
Strep+Tet
d.
*
*
*
untreated
Kan
Strep
Tet
Kan+Strep
Kan+Tet
Strep+Tet
*
*
*
untreated
Kan
Strep
Tet
Kan+Strep
Kan+Tet
Strep+Tet

Figure S24.

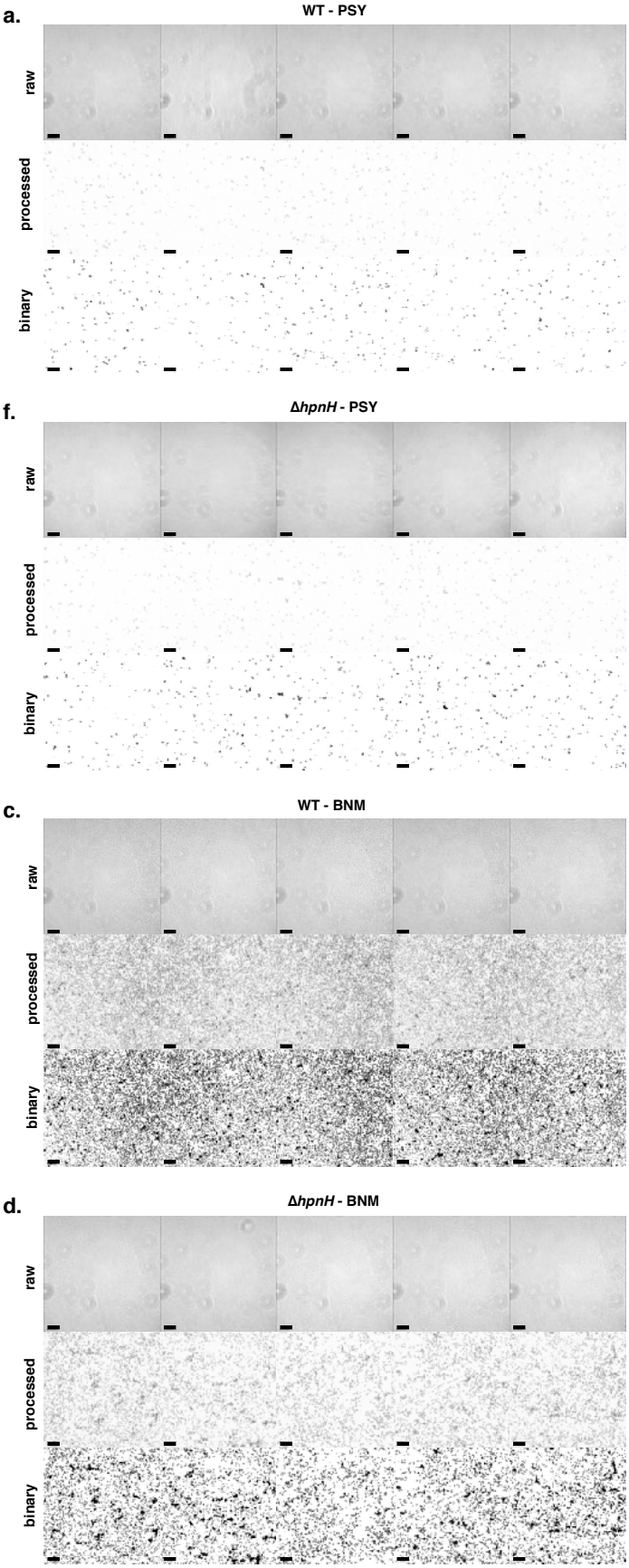
a.
WT - PSY
raw
processed
binary
f.
ΔhpnH - PSY
raw
processed
binary
c.
WT - BNM
raw
processed
binary
d.
ΔhpnH - BNM
raw
processed
binary

Figure S25.